# C O M M U N I C A T I O N S

FACULTY OF SCIENCES
UNIVERSITY OF ANKARA

DE LA FACULTE DES SCIENCES
DE L'UNIVERSITE D'ANKARA

Series A2-A3: Physical Sciences and Engineering

**VOLUME: 62** **Number: 1** **YEAR: 2020**

Faculy of Sciences, Ankara University
06100 Beşevler, Ankara-Turkey
ISSN 1303-6009 E-ISSN 2618-6462

# C O M M U N I C A T I O N S

FACULTY OF SCIENCES
UNIVERSITY OF ANKARA

DE LA FACULTE DES SCIENCES
DE L'UNIVERSITE D'ANKARA

**Series A2-A3: Physical Sciences and Engineering**

**Volume 62** **Number : 1** **Year :2020**



This Journal is published two issues in a year by the Faculty of Sciences, University of Ankara. Articles and any other material published in this journal represent the opinions of the author(s) and should not be construed to reflect the opinions of the Editor(s) and the Publisher(s).

**Correspondence Address:**
COMMUNICATIONS
EDITORIAL OFFICE
Ankara University, Faculty of Sciences,
06100 Tandoğan, ANKARA – TURKEY
**Tel: (90) 312-212 67 20 Fax: (90) 312-223 23 95**
e-mail: commun@science.ankara.edu.tr
http://communications.science.ankara.edu.tr/index.php?series=A2A3

**Print:**
Ankara University Press
İncitaş Sokak No:10 06510 Beşevler
ANKARA – TURKEY

# C O M M U N I C A T I O N S

FACULTY OF SCIENCES
UNIVERSITY OF ANKARA

DE LA FACULTE DES SCIENCES
DE L'UNIVERSITE D'ANKARA

Series A2-A3: Physical Sciences and Engineering

**Volume 62** **Number : 1** **Year :2020**

# C O M M U N I C A T I O N S

FACULTY OF SCIENCES
UNIVERSITY OF ANKARA

DE LA FACULTE DES SCIENCES
DE L'UNIVERSITE D'ANKARA

Commun.Fac.Sci.Univ.Ank.Series A2-A3
Volume 62, Number 1, Pages 1-13 (2020)
DOI: 10.33769/aupse.657684
ISSN 1303-6009 E-ISSN 2618-6462
http://communications.science.ankara.edu.tr/index.php?series=A2A3

# AN ARTIFACT REDUCTION METHOD FOR BLOCK-BASED VIDEO CODING

HAKKI ALPARSLAN ILGIN and AHMET AKBULUT

ABSTRACT. Most of the image/video coding standards are based on discrete cosine transform which is a block-based coding scheme with a disadvantage of blocking effect at low bit rates. In this paper, we propose a hybrid method, which consists of downsampling/upsampling, significance map coding and local cosine transform, to reduce the disadvantage of lossy compression and is also compatible with current standards. Experimental results show that performance of the proposed method is better than the conventional approaches.

## 1. INTRODUCTION

Image and video coding applications require high compression ratios for low bit rate applications and poor channel conditions. However, lossless compression is not sufficient for such cases requiring lossy compression, which causes defects in the reconstructed signal at low bit rates. Image/video compression algorithms and standards mostly consist of both lossy and lossless compression techniques. Furthermore, standards based on discrete cosine transform (DCT) result in blocking artifacts when used with lossy compression schemes at low bit rates. DCT is a block-based transform that converts image into frequency domain coefficients. Lossy compression algorithms primarily neglect most of the high frequency AC coefficients of DCT blocks. Since most of the energy is compacted into DC and low frequency AC coefficients, losing some of the high frequency AC coefficients does not affect the quality of the reconstructed signal significantly. However, as more high frequency AC coefficients are flattened by quantization, reconstructed image gets blurrier. Losing more AC coefficients, especially low frequency ones with higher energy to get more compression causes severe image degradation, which appears as blocking artifact. In the literature, there are many methods to compensate

Received by the editors: December 10, 2019; Accepted: January 07, 2020.
*Key word and phrases:* Local cosine transform, significance map coding, image compression, video coding.

the artifacts. Some of the most frequently used methods are lapped orthogonal transform (LOT) [1], post-filtering [2], linear filtering [3], and subband/wavelet coding [4]. However, LOT is not fully compatible with the standards that include DCT. Post- and linear filtering may get blurry images at low bit rates. Wavelet or subband-based codecs are also incompatible with DCT-based standards. Deblocking filter, which is used in standards such as H.263 Annex J, H.264 [5] and HEVC [6], has its own computational complexity. Recent works with deep learning [7] have additional complexity at training process. In this paper, we use a combined method that consists of downsampling/upsampling, significance map coding (SMC) and local cosine transform (LCT) [8]. Coding is kept in the DCT domain to prevent extra operations and for compatibility with the DCT-based standards. Reducing blocking effects is discussed in the next section. Significance map coding and downsampling/upsampling scheme are applied in section 3. In the last section, conclusion and discussion are given.

## 2. Blocking Effect Reduction

Blocking effect is the most significant artifact of lossy DCT-based coding methods at low bit rates. Several conditions and requirements lead signals to be encoded at low bit rates. However, lossless compression techniques do not provide very high compression ratios. Therefore, lossy compression is used together with lossless techniques. The most common lossy compression method is quantization, which is used in almost all standards. When used with DCT, it causes losses in DCT coefficients. Increasing compression ratio requires more AC coefficients of DCT blocks to be neglected, namely zero. Therefore, blocking effects appear at low bit rate coding and become severe with decreasing bit rate. Being one of the methods to decrease blocking effect, LCT implements folding/unfolding and DCT operations [8]. At the encoder side of LCT, DCT is applied after folding operation. Accordingly, inverse DCT and then unfolding are applied at the decoder. Because of the folding operation, discontinuities across the neighboring block boundaries are smoothed. A bell function defined on the basis of the function for folding operation affects the reconstructed image quality or the compression ratio [8]. After folding operation is performed on all blocks, DCT of each folded block is computed.

Coding with both conventional DCT and LCT are compared in terms of objective metrics. Two of the most frequently used metrics in image and video coding applications are Peak Signal-to-Noise Ratio (PSNR) and structural similarity index (SSIM) [9]. There are also specific MATLAB-based applications for image processing and image quality assessment as in [10]. Beside the objective metrics, subjective methods based on human perception are also used [11]. In this study, we

use both PSNR and SSIM objective metrics to evaluate the quality of the reconstructed images when compared to the original ones. PSNR is given by

$$\mathrm{PSNR}(I,R) = 10log_2\left(\frac{\max(I)^2}{\mathrm{MSE}(I,R)}\right) \quad (1)$$

where

$$\mathrm{MSE}(I,R) = \frac{1}{mn}\sum_{i=1}^{m}\sum_{j=1}^{n}[I(i,j) - R(i,j)]^2 \quad (2)$$

is mean-square error between the original and reconstructed images, $I$ and $R$, respectively, $m$ and $n$ are vertical and horizontal number of pixels and ($i$,$j$) is the coordinate of a pixel in original and reference images. The value of max($I$) is 255 for 8-bit images. SSIM is correlated with the quality perception of the human visual system with the highest value of 1 and given as follows [12]:

$$SSIM(I,R) = \frac{(2\mu_I\mu_R+c_1)(2\sigma_{IR}+c_2)}{(\mu_I^2+\mu_R^2+c_1)(\sigma_I^2+\sigma_R^2+c_2)} \quad (3)$$

where $\mu_I$ and $\mu_R$ are the mean value and $\sigma_I^2$ and $\sigma_R^2$ are the variance of the original and reconstructed images, respectively. $\sigma_{IR}^2$ is the covariance of $I$ and $R$. Variables $c_1$ and $c_2$ are used to stabilize the division with weak denominator and given as $c_1$=(0.01max($I$))$^2$ and $c_2$=(0.03max($I$))$^2$. If there is no correlation between the original and reconstructed images, the value of SSIM is 0. SSIM is higher for the images that are similar. SSIM is 1 when two images are the same. Comparison between codecs with DCT and LCT are given in Tab. 1.

Table 1. DCT and LCT comparison for *soccer* frame #1 and *bus* frame #1

| QP | ***Soccer*** | | | | ***Bus*** | | | |
|---|---|---|---|---|---|---|---|---|
| | **PSNR (dB)** | | **SSIM** | | **PSNR (dB)** | | **SSIM** | |
| | **DCT** | **LCT** | **DCT** | **LCT** | **DCT** | **LCT** | **DCT** | **LCT** |
| 12 | 30.31 | 31.28 | 0.846 | 0.871 | 29.87 | 31.06 | 0.886 | 0.907 |
| 15 | 28.93 | 29.71 | 0.808 | 0.834 | 28.16 | 29.31 | 0.853 | 0.879 |
| 20 | 27.95 | 28.49 | 0.770 | 0.797 | 26.79 | 27.85 | 0.819 | 0.848 |
| 25 | 27.02 | 27.37 | 0.733 | 0.759 | 25.50 | 26.45 | 0.784 | 0.815 |
| 30 | 26.61 | 26.91 | 0.704 | 0.736 | 24.79 | 25.70 | 0.758 | 0.791 |
| 35 | 26.08 | 26.33 | 0.678 | 0.711 | 24.00 | 24.78 | 0.730 | 0.766 |
| 40 | 25.76 | 26.04 | 0.658 | 0.693 | 23.57 | 24.36 | 0.709 | 0.747 |
| 45 | 25.41 | 25.74 | 0.641 | 0.676 | 23.02 | 23.76 | 0.686 | 0.726 |
| 50 | 25.22 | 25.56 | 0.630 | 0.663 | 22.70 | 23.40 | 0.669 | 0.710 |

FIGURE 1. Reconstructed *bus* frame #1 from coding scheme with LCT (top) and DCT (bottom) with QP=50.

In Tab. 1, first frames of 8-bit grayscale *soccer* and *bus* video sequences with 288x352 pixel resolution are encoded as intraframe with quantization parameters (QP) between 12 and 50, for both DCT and LCT coding schemes with 8x8 block size. LCT performs better than DCT for all QP values as seen in Tab. 1. As the bit rate decreases with increasing QP, artifacts become more visible. Comparison between LCT and DCT encoded *bus* frame #1 with QP=50 is given in Fig. 2. Blocking effect in the reconstructed image coded with DCT is severe as seen in Fig.

1. Also, DCT encoded reconstructed image has more blurry effects than the LCT encoded image.

## 3. Improving Quality By Significance Map Coding And Downsampling/Upsampling

Image quality degradation by lossy compression techniques for block-based algorithms appears block-wise at low bit rates. In the previous section, we used an effective method to decrease the blocking artifacts caused by high compression rates. In this section, we further improve image quality by applying LCT with significance map coding and downsampling in the coder and the corresponding upsampling in the decoder. Image quality is deteriorated more with higher compression rates. However, by using the hybrid approach, we aim to decrease the disadvantage of very low bit rate coding.

We first implement SMC together with LCT to improve image quality. Embedded image zerotree coding of wavelet coefficients is an efficient example of SMC [13]. This method is applied for DCT beside the wavelet transform. An improved method is set partitioning in hierarchical trees (SPIHT), which has a better compression performance [14], and still being used widespread recently [15]. SPHIT is an iterative algorithm with threshold halved at each iteration and encodes transform coefficients in decreasing order with binary output. In the first part of the algorithm, coefficients are compared with a threshold, which is the lower value of an uncertainty interval, to output bits corresponding to significance of coefficients or a hierarchical structure. In the second part, coefficients previously found to be significant are given one-bit precision. Since SPIHT can be applied for DCT, we implement the algorithm with LCT, which has DCT partly.

In the next experiments, we compare the improvement by LCT with SPIHT significance map coding (LCT-SMC) to DCT-SMC for video frames encoded intraframe. Before applying significance map coding, DCT coefficients are rearranged in subband structure. We use the most common grayscale CIF videos with 288x352 pixel resolution. Improvement of LCT-SMC is clearly seen for *salesman* and *city* frame #1 in terms of PSNR and SSIM in Fig. 2. At lower bit rates, advantage of LCT-SMC over DCT-SMC is apparent as supported by PSNR and SSIM. When reconstructed image is visually almost inseparable from the original one, increase of SSIM is much slower than PSNR. LCT is very efficient for intraframe at low bit rates when used with SMC, since SMC efficiently encodes coefficients with higher energy initially, so that the degradation caused by lower

energy coefficients, which are mostly related to high frequency details in the frame, does not distort image conspicuously. Besides SMC is applicable to DCT, since it is not block based algorithm, it does not have the disadvantage of blocking effect at low bit rates. Using SMC in conjunction with LCT achieves better results for reconstructed images.

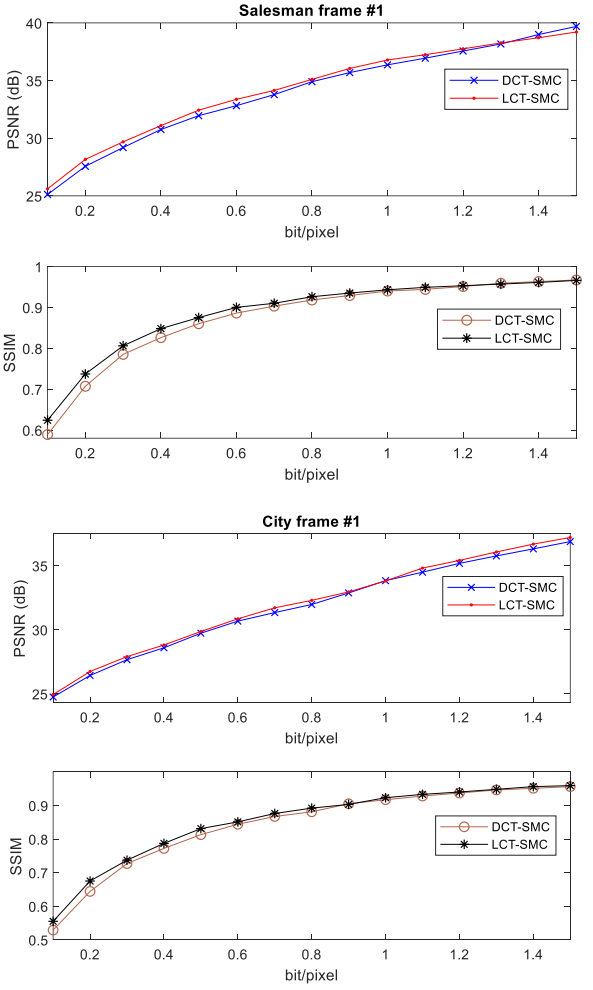


FIGURE 2. Comparison for intraframe coding at different bit rates

We also compare interframe coding performance of LCT-SMC and DCT-SMC. PSNR and SSIM per frame of both methods are given for *soccer*, *city* and *coastguard* sequences for first 30 frames in Fig. 3.

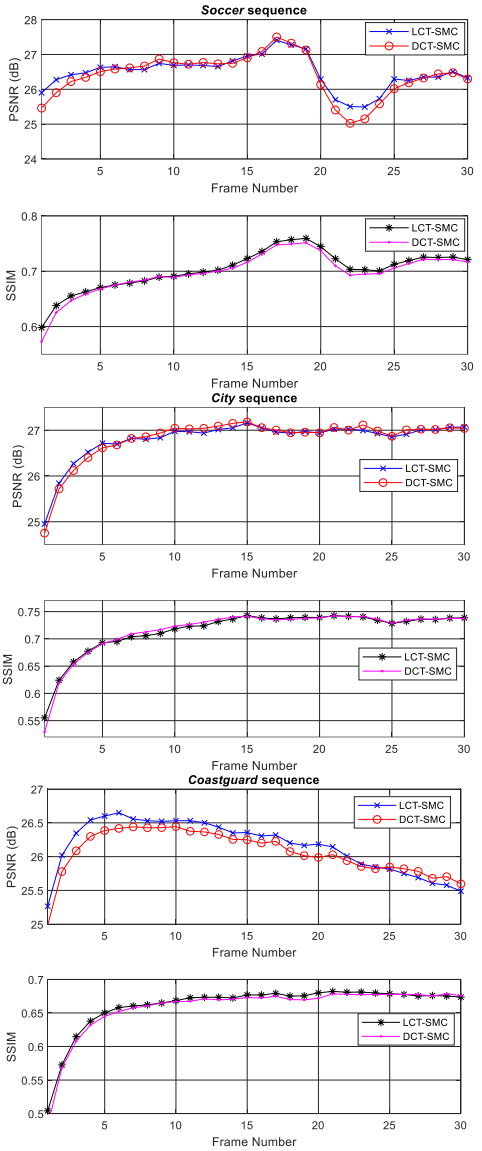


FIGURE 3. Interframe coding with LCT-SMC and DCT-SMC

Total bits for 30 frames for each sequence is 46881. Intraframe of each sequence is encoded with 10138 bits (or 0.1 bpp) and each of the 29 interframe is encoded with just 1267 bits (or 0.0125 bpp).

Interframe performance of LCT is not as efficient as its intraframe performance, since SMC and motion estimation/compensation help to improve the quality of the interframes [16]. However, performance of intraframe coding helps to improve coding efficiency of consecutive interframes as shown in Fig. 3, since first frame of each sequence gives higher PSNR with LCT-SMC than DCT-SMC, consequently the following interframes give high PSNR values. Since SMC is efficient for any cases, i.e. for DCT or LCT, its combination with either of the two achieves close results as seen in Fig. 3. Mean of PSNR and SSIM for 29 interframe coding in Fig. 3 are given in Tab. 2.

Table 2. Average PSNR and SSIM for Interframe Coding

| **Sequence** | **PSNR (dB)** | | **SSIM** | |
|---|---|---|---|---|
| | **DCT-SMC** | **LCT-SMC** | **DCT-SMC** | **LCT-SMC** |
| *Soccer* | 26.43 | 26.50 | 0.701 | 0.706 |
| *City* | 26.89 | 26.87 | 0.722 | 0.721 |
| *Coastguard* | 26.10 | 26.19 | 0.663 | 0.666 |

Loss in quality first appears at the details which corresponds to high frequency AC coefficients of DCT as bit rate decreases. Increasing compression ratio further makes image blurry, which is the result of degradation of more AC coefficients with lower frequency. When the compression requires very low bit rate, AC coefficients with the lowest frequencies and DC coefficient are also deteriorated. Accordingly, the resulting image will have blocking effects. Therefore, before losing information by lossy compression, we apply downsampling for each block in the frequency domain whose efficiency was shown in [17]. Another advantage of keeping downsampling in the frequency domain is that computational complexity caused by inverse DCT, decimation in the spatial domain and forward DCT is avoided. Thus, image quality is enhanced with only limited additions of computations, since proposed downsampling and upsampling are operated fully in the DCT domain. When downsampling/upsampling by 2 in the DCT domain with SMC is implemented, we obtain better results than the case of DCT-SMC. We further improve the results by using downsampling/upsampling with LCT-SMC. Results are shown in Fig. 4 for five video sequences.

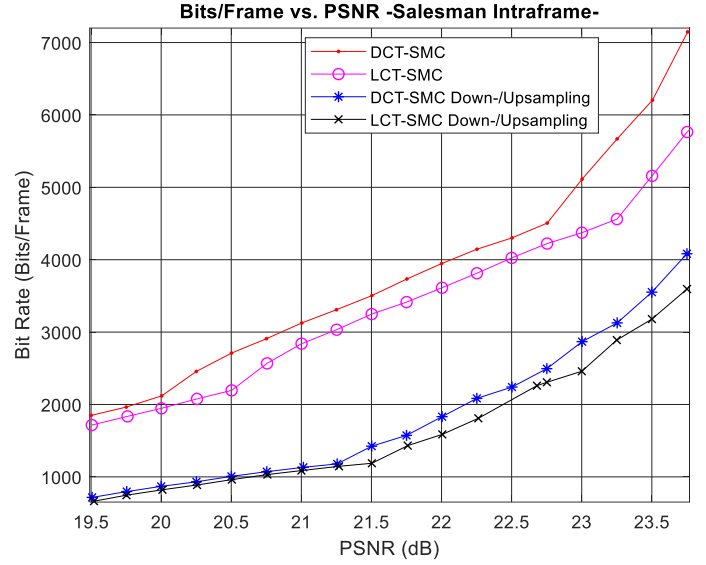
Bits/Frame vs. PSNR -Salesman Intraframe-
DCT-SMC
LCT-SMC
DCT-SMC Down-/Upsampling
LCT-SMC Down-/Upsampling
Bit Rate (Bits/Frame)
PSNR (dB)
7000
6000
5000
4000
3000
2000
1000
19.5
20
20.5
21
21.5
22
22.5
23
23.5

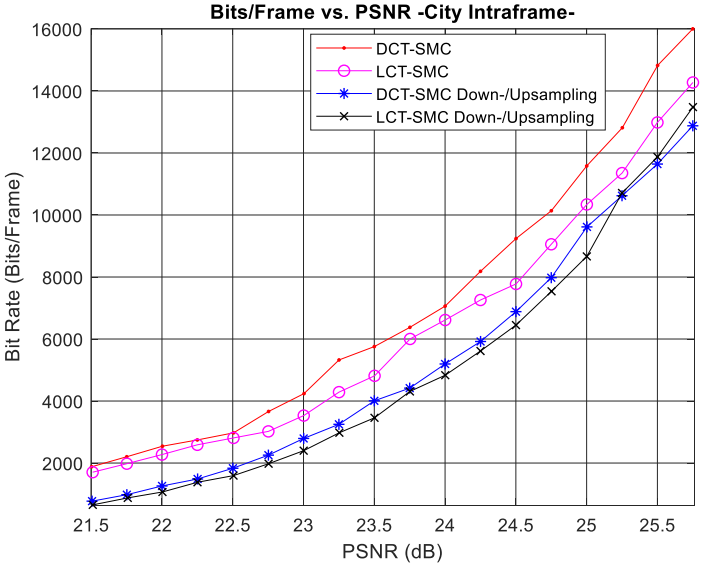
Bits/Frame vs. PSNR -City Intraframe-
DCT-SMC
LCT-SMC
DCT-SMC Down-/Upsampling
LCT-SMC Down-/Upsampling
Bit Rate (Bits/Frame)
PSNR (dB)
16000
14000
12000
10000
8000
6000
4000
2000
21.5
22
22.5
23
23.5
24
24.5
25
25.5

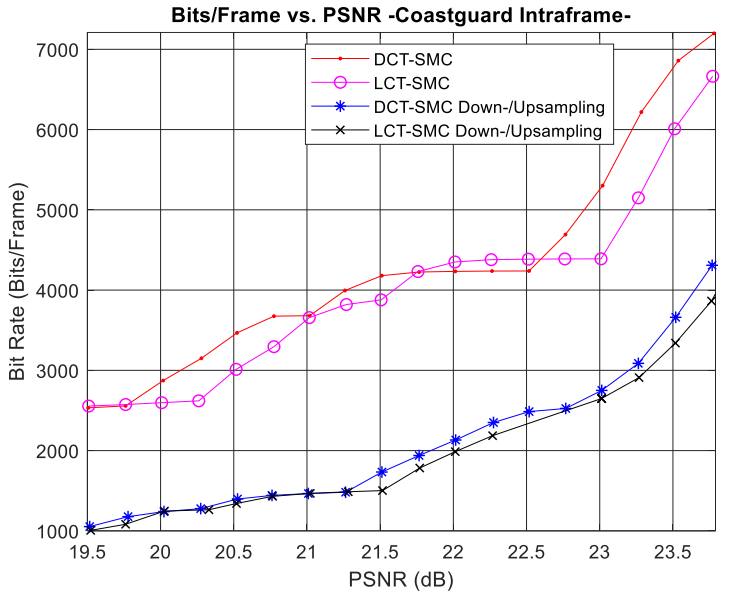
Bits/Frame vs. PSNR -Coastguard Intraframe-
DCT-SMC
LCT-SMC
DCT-SMC Down-/Upsampling
LCT-SMC Down-/Upsampling
Bit Rate (Bits/Frame)
PSNR (dB)
7000
6000
5000
4000
3000
2000
1000
19.5
20
20.5
21
21.5
22
22.5
23
23.5

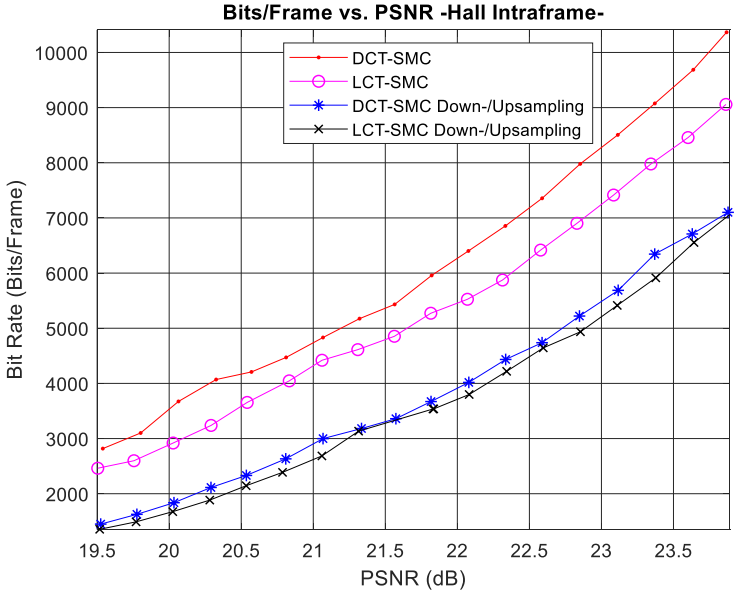
Bits/Frame vs. PSNR -Hall Intraframe-
DCT-SMC
LCT-SMC
DCT-SMC Down-/Upsampling
LCT-SMC Down-/Upsampling
Bit Rate (Bits/Frame)
PSNR (dB)
10000
9000
8000
7000
6000
5000
4000
3000
2000
19.5
20
20.5
21
21.5
22
22.5
23
23.5

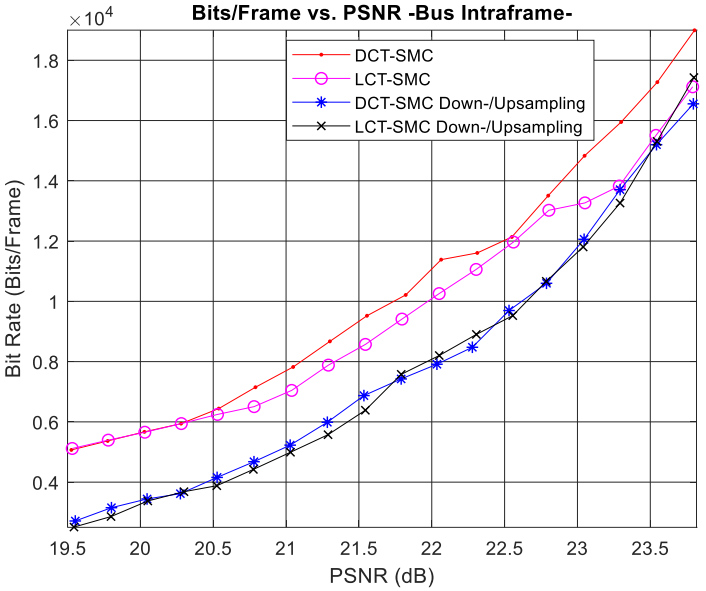


FIGURE 4. Quality improvement by downsampling/upsampling with LCT-SCM over other methods

## 4. CONCLUSION

Lossy compression of videos is required for low bandwidth and limited storage area conditions when lossless compression is not sufficient. In such cases, reconstructed video frames may have artifacts such as blocking effects and blurred scenes and objects. In order to surpass the artifacts at low bit rates, we used a hybrid method which includes LCT, SMC and downsampling/upsampling in the compressed domain. We showed that the LCT is efficient for deblocking of intraframes, while, SMC applied as SPIHT is very efficient for both intraframe and interframes. Furthermore, even though LCT has being used widely after its introduction, we utilized LCT in conjunction with SMC to decrease artifacts more efficiently. LCT-SMC is also compatible with most of the DCT-based standards still being used, since it implements DCT. Using downsampling at the coder and corresponding upsampling at the decoder increases coding performance because of energy conservation before losing DCT coefficients with high energy because of lossy compression. We implemented both downsampling and upsampling in the DCT domain with the factor of 2. It is also possible to use other factors to increase the coding performance at lower bit rates.

## References


[1] Malvar, H. S., The LOT: a link between block transform coding and multirate fillter banks, *IEEE Intern. Symp. Circuits and Systems,* (1988), 835-838.

[2] Tzou, K.-H., Post-filtering of transform-coded images, *Applications of Digital Image Proc.,* vol. 974, (1988), 121-126.

[3] Awil, C. and Nguyeri-Trsng, T., Linear filtering for reducing blocking effects in orthogonal transform image coding, Journal of Electronic Imaging 1(2) , (April 1992), 183-191.

[4] Wu, Po-Cheng, Chen, Liang-Gee and Lai, Yeong-Kang, A block shifting method for reduction of blocking effects in subband/wavelet image coding, IEEE Transactions on Consumer Electronics, vol. 44, no. 1, (Feb. 1998), 170-177. doi: 10.1109/30.663744

[5] Joint Video Team of ITU-T and ISO/IEC JTC 1, Draft ITU-T Recommendation and Final Draft International Standard of Joint Video Specification (ITU-T Rec. H.264 | ISO/IEC 14496-10 AVC), Joint Video Team (JVT) of ISO/IEC MPEG and ITU-T VCEG, JVT-G050r1, May 2003.

[6] Sullivan, G. J., Ohm, J. R. and Han W. J., Overview of the high efficiency video coding (HEVC) standard, *IEEE Trans. Circuits Syst. Video Technol.,* vol. 22 no. 12 (Dec. 2012) pp. 1649-1668.

[7] Goodfellow, Ian, Bengio, Yoshua and Courville, Aaron, Deep Learning, MIT Press, 2016.

[8] Aharoni, G., Averbuch, A., Coifman, R. and Israeli, M., Local Cosine Transform - A Method for the Reduction of the Blocking Effect in JPEG, *Journal of Mathematical Imaging and Vision,* (1993), pp. 7-38.

[9] Horé, A. and Ziou, D., Image Quality Metrics: PSNR vs. SSIM, *2010 20th International Conference on Pattern Recognition*, Istanbul, (2010), 2366-2369. doi: 10.1109/ICPR.2010.579

[10] Krasula, L., Klima, M., Rogard, E. and Jeanblanc, E., MATLAB based Applications for Image Processing and Image Quality Assessment – Part I: Software Description, *Radioengineering,* Vol. 20, No. 1, (Dec. 2011) 1009-1015.

[11] Richter, T. and Larabi, C., Subjective and Objective Assesment of Visual Image Quality Metrics and Still Image Codecs, *Data Compression Conference (dcc 2008)*, Snowbird, UT, (2008), 541-541. doi: 10.1109/DCC.2008.44

[12] Wang, Zhou, Bovik, A. C., Sheikh, H. R. and Simoncelli, E. P., Image quality assessment: from error visibility to structural similarity, *IEEE Transactions on Image Processing*, vol. 13, no. 4, (April 2004), pp. 600-612. doi: 10.1109/TIP.2003. 819861

[13] Shapiro, J. M., Embedded image coding using zerotrees of wavelet coefficients, *IEEE Transactions on Signal Processing*, vol. 41, no. 12, (Dec. 1993), 3445-3462. doi: 10.1109/78.258085

[14] Said, A. and Pearlman, W. A., A new, fast, and efficient image codec based on set partitioning in hierarchical trees, IEEE Transactions on Circuits and Systems for Video Technology, vol. 6, no. 3, (June 1996), 243-250. doi: 10.1109/76.49

[15] Bini, S. P. and Abirami, S., Secure image deduplication using SPIHT compression, *2017 Int. Conf. on Commu. and Signal Proc.* (ICCSP), Chennai, 2017, 276-280. doi: 10.1109/ICCSP.2017.828636

[16] Ilgin, H. A., Akbulut, A. and Kalaycıoğlu, A., Image and Video Compression Artifact Reduction at Low Bit Rates Using Local Cosine Transform in Conjuction with Significance Map Coding, *11th International Conference on Electronics, Computers and Artificial Intelligence*, ECAI 2019, June 2019.

[17] Ilgin ,H. A. and Chaparro, L. F., Low Bit Rate Video Coding Using DCT-Based Fast Decimation/Interpolation and Embedded Zerotree Coding, *IEEE Transactions on Circuits and Systems for Video Technology*, vol. 17, no. 7, July 2007, 833-844. doi: 10.1109/TCSVT.2007.898655

*Current Address:* Hakkı Alparslan ILGIN (Corresponding author): Ankara University, Electrical and Electronics Engineering Department, Ankara, Turkey
*E-mail:* ilgin@eng.ankara.edu.tr
*Orcid ID:* https://orcid.org/0000-0003-0112-4833

*Current Address:* Ahmet AKBULUT: Ankara University, Electrical and Electronics Engineering Department, Ankara, Turkey
*E-mail:* aakbulut@ankara.edu.tr
*Orcid ID:* https://orcid.org/0000-0001-8868-7385

Commun.Fac.Sci.Univ.Ank.Series A2-A3
Volume 62, Number 1, Pages 14-25 (2020)
DOI: 10.33769/aupse.559971
ISSN 1303-6009 E-ISSN 2618-6462
http://communications.science.ankara.edu.tr/index.php?series=A2A3

# THE DESIGN OF STANDALONE PV SYSTEM USING P&O ALGORITHM FOR MAXIMUM POWER POINT TRACKING

KENAN ÖZEL and AHMET KARAARSLAN

ABSTRACT. This paper presents the simulation of output power control of photovoltaic panel using Maximum Power Point Tracking (MPPT) controller of boost converter. Due to the stochastic behavior of temperature and irradiation condition, integrating a MPPT algorithm to DC-DC converter is important for extracting the maximum power from photovoltaic system. The Perturb and Observe (P&O) algorithm has been preferred due to its lower complexity and easy implementation. The main aim of this study is to track the maximum operation point of photovoltaic system and to control the output power with respect to the changing irradiation and temperature. The simulation results demonstrate that MPPT controller prevents the power deviation and provide to extract maximum possible power from solar array.

## 1. INTRODUCTION

The increasing demand for energy raises concerns about environmental pollution and energy crisis. The usage of alternative energy sources is considered the most effective solution to overcome these concerns. Recently, these energy sources have become increasingly important due to the depletion of fossil fuel reserves. Amongst them, solar energy is one of the most eminent energy sources owing to inexhaustible nature and free of use [1, 2].

Photovoltaic (PV) cells are devices that convert solar energy directly into electrical energy. However, the electrical power output of the PV cells is significantly affected by changing atmospheric conditions [3]. As seen in Fig. 1, the current-voltage (I-V) characteristics of PV cells are influenced by solar irradiance and temperature. The bending point of I-V characteristic curve of PV cell points out an operation point

Received by the editors: May 02, 2019; Accepted: January 15, 2020.
*Key word and phrases:* MPPT, DC-DC Converter, P&Q Algorithm.

called MPPT. At this point, PV cells deliver maximum power, working with highest efficiency [4]. Hence, it is important to track this point for extracting maximum possible power from PV system under various conditions.

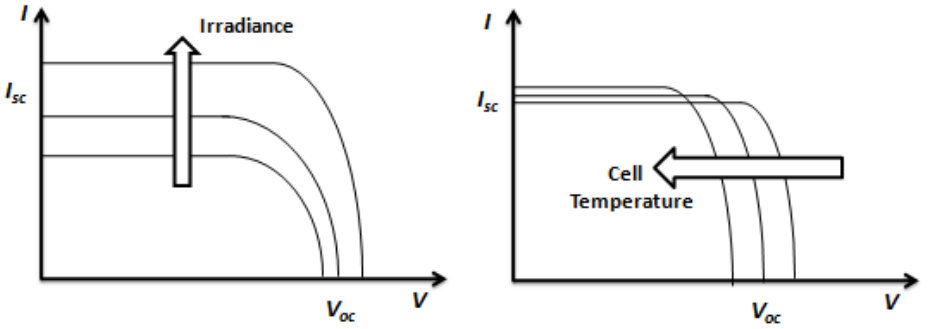


FIGURE 1. I-V characteristics of PV cell with (a) irradiation and (b) temperature effect.

This study is generally divided into 5 sections. The first is the modeling of the PV cell. Section 2 relates to the operation of the boost converter to be used in the simulation. Section 3 presents the review of the MPPT and P&O Algorithm. In section 4, the simulation of the independent PV system in MATLAB / Simulink is given and the results are listed in section 5.

## 2. THE MODELING OF PHOTOVOLTAIC (PV) CELL

The equivalent circuit model of a PV cell is shown in Fig. 2. This circuit model called single diode model comprises two resistances which are series $R_s$ and parallel $R_{sh}$. It is desirable for an ideal PV cell to have a low $R_s$ and high $R_{sh}$ value. Open circuit voltage ($V_{oc}$), short circuit current ($I_{sc}$) is related with $R_{sh}$ and $R_s$, respectively [5].

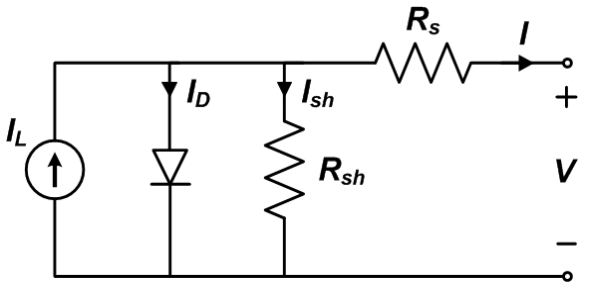


FIGURE 2. Single diode equivalent circuit model of PV cell.

Solar modules consist of a number of solar cells connected series. Similarly, solar arrays are made up of solar modules connected in series and in parallel. The module used in this work consists of $N_s$=96 of series connected solar cells and array is made up of 5 series and 66 parallel connected modules.

Generally, PV systems are classified into two main categories, which are grid-connected and standalone mode. In our case, we have worked on standalone system. Fig. 3 displays the basic block diagram of a standalone solar system [6]. In this system, electrical power produced by solar module is fed to the load, passing through DC-DC converter. Conventional Perturb and Observe (P&O) MPPT algorithm can be applied to a DC-DC Boost converter to provide the maximum power output of the PV module.

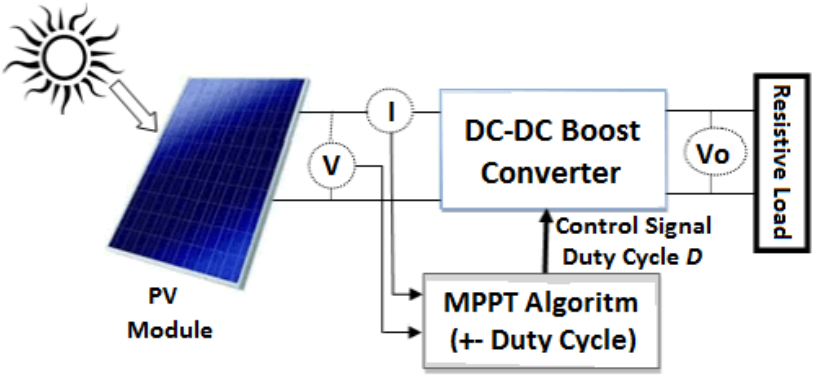


FIGURE 3. Block diagram of PV system with MPPT controller.

## 3. THE TOPOLOGY OF DC-DC BOOST CONVERTER

Circuit diagram of a DC-DC Boost converter is shown in Fig. 4. The circuit consists of an input capacitor, an output capacitor, an inductor, a switching device (IGBT or MOSFET), a diode and a load. This type of converter is also named as boost converter due to the larger output than the input. [7, 13]. The output voltage is adjusted by switching device which is either on or off depending on the duty cycle D coming from MPPT controller. Output voltage is given by the following equations:

$$V_{in} * t_{on} + (V_{in} - V_0) * t_{off} = 0 \tag{1}$$

$$t_{on} + t_{off} = t_s \tag{2}$$

According to the given equations (1-2), the relation between input and output voltage is obtained depending on the duty cycle given as in Equation (3).

$$\frac{V_0}{V_i} = \frac{t_s}{t_{off}} = \frac{1}{1-D} \tag{3}$$

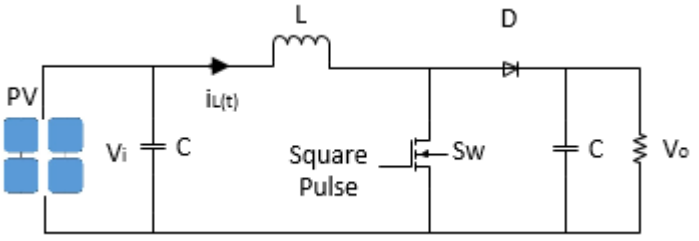


FIGURE 4. Circuit diagram of DC-DC Boost converter

Herein, D (duty cycle) is given as the ratio of the elapsed time when switch is off, to the total period of switching time. The dc-dc boost converter is operated in two

different modes depending on the switching conditions. If the switch is on-state mode, two parts of the circuit can be given as in Fig. 5 (a). First part is related to the inductor and switch. In this condition, inductor stores energy. The other part is regarding to capacitor. Stored energy in the capacitor discharges through the load. If the switch is off-state mode, stored energy in the inductor is transferred to the capacitor and load via the diode. Thus, the capacitor is recharged by the inductor, which is shown in Fig. 5 (b).

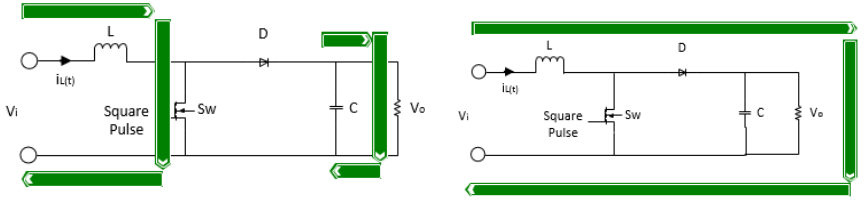


FIGURE 5. Conduction states of boost converter: (a) On-mode condition, (b) Off-mode condition.

## 4. PERTURB AND OBSERVE ALGORITHM (P&O)

This algorithm has been preferred due to its lower complexity and easy implementation [8]. This technique is based on the inserting slight perturbation to the system and the observation of system response [9]. In order to trace maximum operation point, output voltage of PV system is decreased or increased in accordance with the changes in power ΔP. If the power changes are positive, then we are on the right MPP track and maintain the perturbation in the same direction. Just for the opposite case, perturbation direction has to be changed [10]. Fig. 6 depicts the flowchart of P&O algorithm.

P&O algorithm is started by perturbing the PV array's voltage periodically. Then, PV output power is computed and compared with previous power values [11]. PV power and voltage value are increased or decreased by a perturbation step. According to the difference between calculated and last power/voltage value before perturbation, duty cycle (D) will be collected or differentiated with a finite increment (ΔD), to determine the next perturbation step size. This process will be executed continuously to attain a specific point at which maximum power can be extracted from PV system [12].

## 5. Simulation of the Standalone PV System in MATLAB/Simulink

Standalone PV system is constructed with MATLAB/Simulink software. By using this simulation, it can be evaluated the performance of the system. In the simulation, perturb and observe algorithm based MPPT controller are used to generate the switching signal which is the input of switching device of the DC-DC Boost converter. Also, PV current generated by the PV array is fed to the load through DC-DC Boost converter. The simulation model of standalone PV system built in MATLAB/Simulink is represented in Fig. 7. As can be understood, MPPT controller is the heart of the system, determining the output characteristics. Fig. 8 illustrates the subsystem representing the MPPT controller based on the perturb and observe algorithm depicted in Fig. 5.

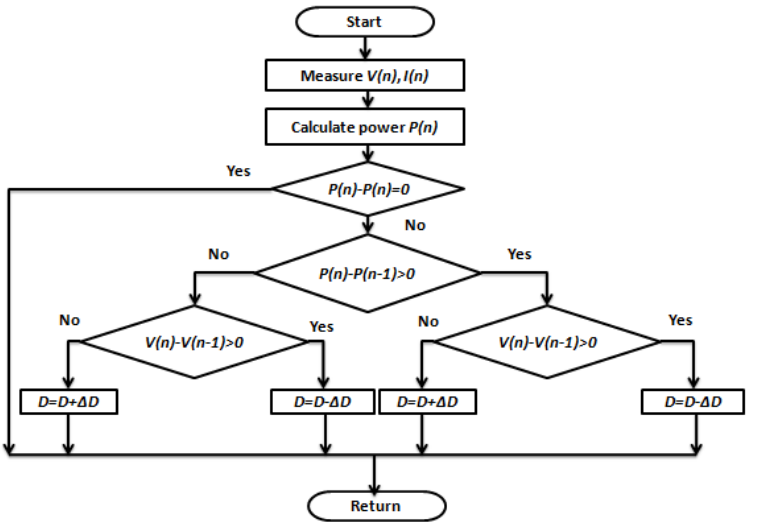


Figure 6. Flowchart of Perturb and Observation algorithm

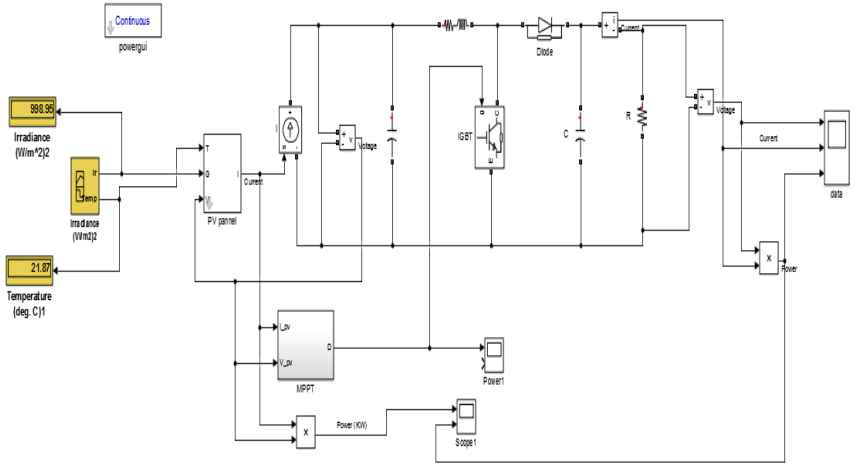


FIGURE 7. Standalone PV system built in Matlab/Simulink

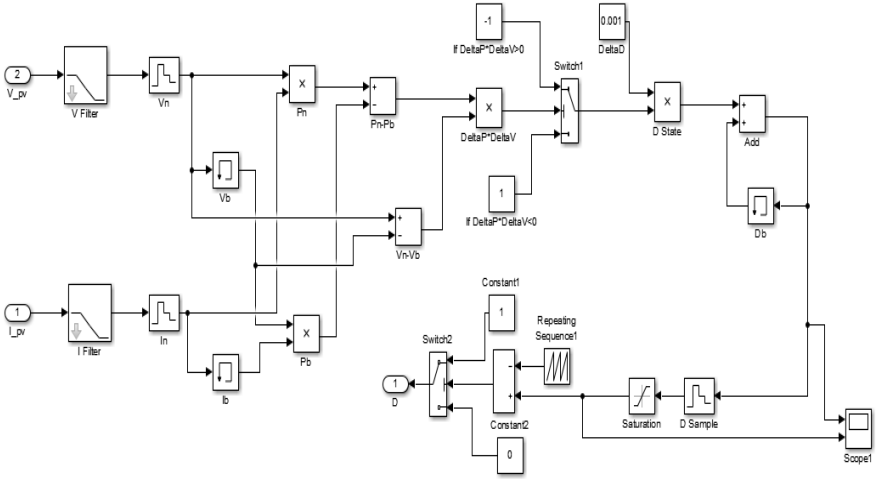


FIGURE 8. Subsystem representing the MPPT controller

In this study, a simulation is conducted to investigate the effect of changes in radiation and temperature. Time-varying input irradiation and temperature signals

are shown in Fig. 9. These changing inputs determine the output photoelectrical parameters of PV panel. Because of the non-linear properties of these inputs, it is required the use of the MPPT controller to obtain the maximum possible power from the PV panel. Fig. 10 represents the plot of switching signal assigned by the MPPT algorithm. This switching signal is used to determine the working condition of switching device.

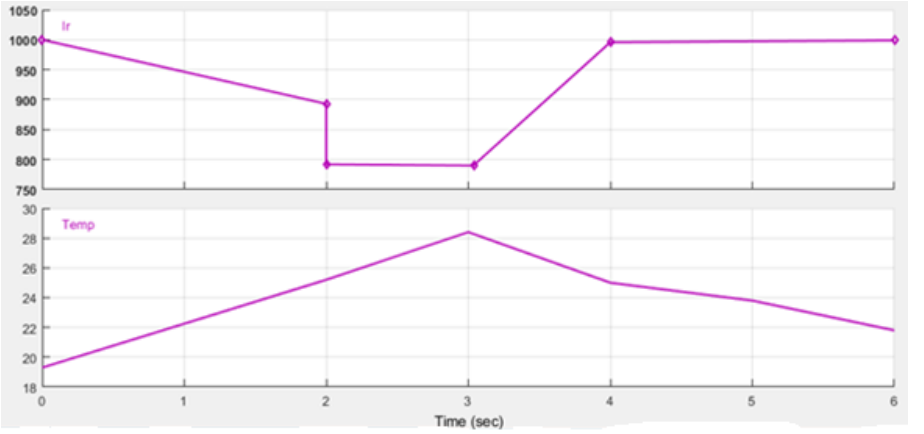


FIGURE 9. Time-varying input irradiation and temperature signals

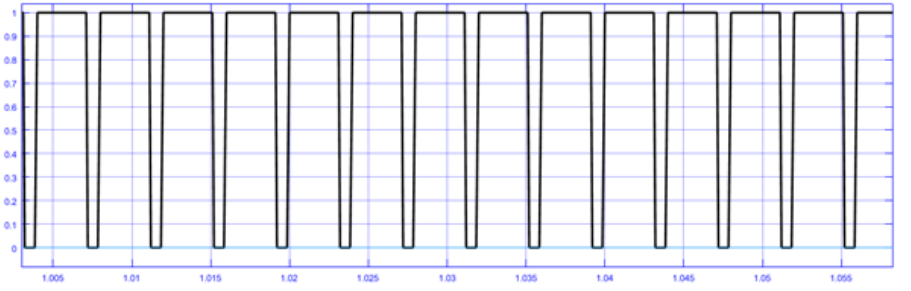

FIGURE 10. Plot of the switching signal

Fig. 11 shows the load voltage, current and power. The initial irradiation level is of 1000 W/m$^2$ and starts to decrease with time. At t=2 s, it begins to fall to 800 W/m$^2$ and stays this level during an interval of 1s. At t=3 s, it begins to rise at the same

level initial condition. Considering temperature variation, initial temperature value is of unnecessary 19.6ºC and begins to rise to 28ºC at t=3 s. Then, the temperature is subject to variation by decreasing back towards 21.8 ºC. The MPPT technique is used to track the maximum power point of PV array depending on the instantaneous current and voltage values. At any circumstances, MPPT will be tracking the MPP of the PV array by adjusting the duty cycle of the converter. As implied by the name, boost converter amplifies the output voltage of PV array. Irradiance and temperature inputs have opposite effect on output current. Fig. 11 displays the load voltage, current and power.

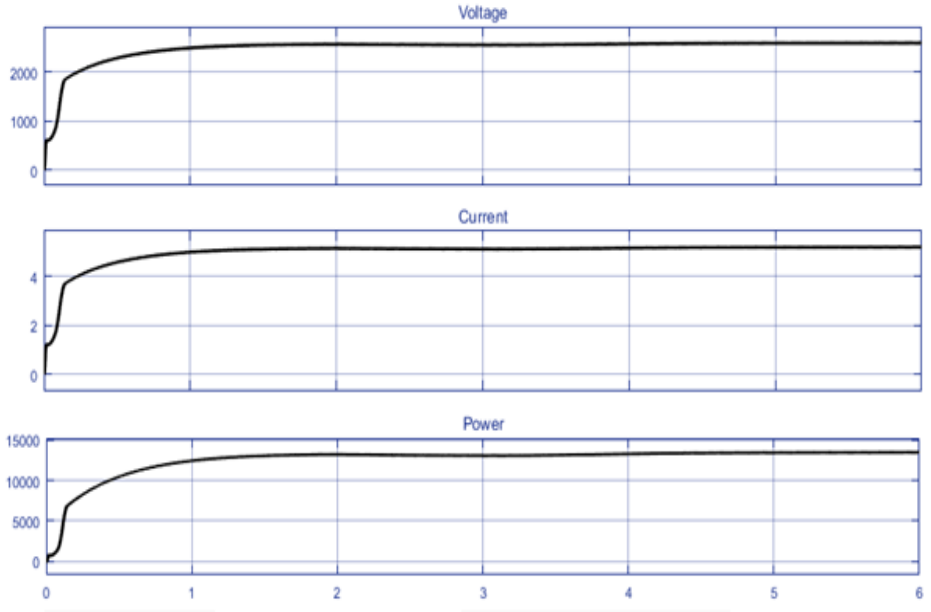


FIGURE 11. Simulation results of the converter with Perturb and Observation algorithm

Fig. 12 depicts the PV system output power in presence of irradiation and temperature variation. Without MPPT controller, the output power of system oscillates at the simulation time and it is affected with varying atmospheric conditions. This output power can be fixed using MPPT controller.

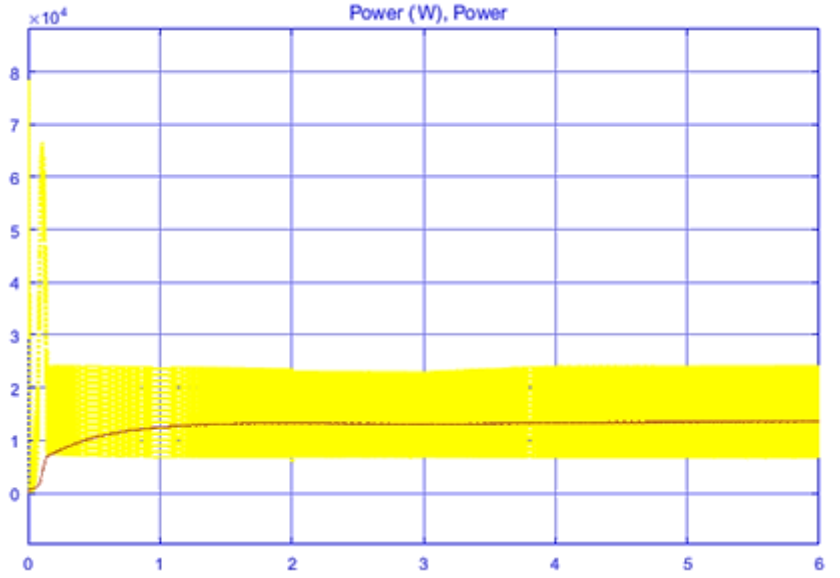


FIGURE 12. System power result in presence of irradiation and temperature variations.

## 6. CONCLUSION

This paper deals with designing of a standalone PV system using P&O algorithm for MPPT in MATLAB/Simulink environment. The focus of this work is to investigate the effect of MPPT controller on the output power of PV system. As seen from the results, nearly stable power output was achieved by inserting perturb and observe algorithm to the DC-DC Boost converter. It was observed that MPPT is not deviated from the tracking of varying maximum power point owing to the irradiation and temperature variations.

## REFERENCES

[1] Jothi, G.J.G. and Geetha, N., An Enhanced MPPT Technique for High Gain DC-DC Converter for Photovoltaic Applications, *2016 International Conference On Circuit, Power And Computing Technologies* [ICCPCT], IEEE, (2016).

[2] Haque, A., Maximum Power Point Tracking (MPPT) Scheme for Solar Photovoltaic System, *Energy Technology& Policy (2014) Published with License by Taylor & Francis Group LLC,* (2014), 115-122.

[3] Bodur, M. and Ermiş, M., Maximum Power Point Tracking for Low Power Photovoltaic Solar Panels, *IEEE Electrotechnical Conference Proc,* (1994), 758-761.

[4] Attou, A., Massoum, A. and Saidi, M., Photovoltaic Power Control Using MPPT And Boost Converter, *Balkan Journal of Electrical&Computer Engineering,* vol. 2, no. 1, (2014), 23-27.

[5] Salmi, T. and Bouzguenda, M., Matlab/Simulink based modelling of solar photovoltaic cell, *International Journal of Renewable Energy Research*, Vol. 2, no. 2, (2012).

[6] Mhiri, N., Alahdal, A., Ghulman, H. and Ammous, A., A Novel Analog Circuit Design for Maximum Power Point Tracking of Photovoltaic Panels, *Advances in Power Electronics*, (2017), 1-9.

[7] Chaitanya, T. and Saibabu, Ch., Modeling and Simulation of PV Array and its Performance Enhancement Using MPPT (P&O) Technique, *International Journal of Computer Science & Communication Networks*, 1(1), (2011).

[8] Sholapur, S. and Narsimhegowda, K.R., Boost Converter Topology for PV System with Perturb And Observe MPPT Algorithm, *IOSR Journal Of Electrical And Electronics Engineering* (IOSR-JEEE), vol.9, no. 4, (2014), 50-56.

[9] Ferchichi, M., Zaidi, N. and Khedher, A., Comparative Analysis for Various Control Strategies Based MPPT Technique of Photovoltaic System Using DC-DC Boost Converter, *17th International Conference on Sciences and Techniques of Automatic Control & Computer Engineering*- STA'2016, 2016 IEEE, (2016), 532-539.

[10] Bounechba, H., Bouzid, A., Nebti, K. and Benalla, H., Modeling and Simulation of Perturb and Observe MPPT Algorithm For Pv Systems, *International Conference STA*, (2013).

[11] Villalva, M. G., Gazoli, J. R. and Filho, E. R., A Study of Maximum Power Point Tracking Algorithms for Stand-alone Photovoltaic Systems, *IEEE Applied Power Electronics Colloquium* (IAPEC) (2011).

[12] Ngan, M. S. and Tan, C. W., Analysis ans Simulation of The P&O Algorithm Using A Linearized PV Array Model, *IECON'09 Industrial Electronics Conference*, (2009), 231-236.

[13] Erel, M. Z., Özev, M., Karaarslan, A., The Comparison of OCC and PI Control Method for DC-DC Boost Converter, *IATS'17 8th International Advanced Technologies Symposium*, (2017).

*Current Address:* KENAN ÖZEL: Ankara University, GAMA Vocational School, 06120, Keçiören, Ankara, TURKEY
*E-mail:* kozel@ankara.edu.tr
*ORCID:* https://orcid.org/0000-0002-0250-3731

*Current Address:* Ahmet KARAARSLAN: Ankara Yildirim Beyazit University, Department of Electrical and Electronics Engineering, Ankara, 06120, TURKEY
*E-mail :* akaraarslan@gmail.com
*Orcid ID:* https://orcid.org/0000-0001-6475-4539

Available online: February 5, 2020

Commun.Fac.Sci.Univ.Ank.Series A2-A3
Volume 62, Number 1, Pages 26–34 (2020)
DOI: 10.33769/aupse.611958
ISSN 1303-6009 E-ISSN 2618-6462
http://communications.science.ankara.edu.tr/index.php?series=A2A3

# LEARNING DENSE CONTEXTUAL FEATURES FOR SEMANTIC SEGMENTATION

LONG ANG LIM AND HACER YALIM KELES

Abstract. Semantic segmentation, which is one of the key problems in computer vision, has been applied in various application domains such as autonomous driving, robot navigation, or medical imagery, to name a few. Recently, deep learning, especially deep neural networks, have shown significant performance improvements over conventional semantic segmentation methods. In this paper, we present a novel encoder-decoder type deep neural network-based method, namely XSeNet, that can be trained end-to-end in a supervised manner. We adapt ResNet-50 layers as the encoder and design a cascaded decoder that is composed of the stack of the X-Modules, which enables the network to learn dense contextual information and have wider field-of-view. We evaluate our method using CamVid dataset, and experimental results reveal that our method can segment most part of the scene accurately and even outperforms previous state-of-the art methods.

## 1. Introduction

Semantic segmentation, which is the key problem in the field of computer vision that concerned with partitioning image frames in video sequences into multiple regions, is an active research area until these days. Consider road-scene video sequences, where those road-scene regions are assigned any semantic categories such as sidewalk, road, pedestrian, sky, building, and tree etc. More precisely, semantic segmentation is a multi-class classification problem, where each pixel of an image is associated with a class label. In this case, the representation of an image is changed to something that is more meaningful and easier to understand. Pixel-wise semantic segmentation is useful in various applications such as autonomous driving, medical imagery, and robot navigation etc.

Recently, Convolutional Neural Networks (CNNs) [14] are very powerful in extracting hidden feature representations from data [28] and have been successfully

Received by the editors: August 27, 2019; Accepted: February 04, 2020.
*Key words and phrases.* Semantic segmentation, deep learning, convolutional neural networks, pixel classification, autonomous driving.

used in many recognition tasks [14, 13, 22, 16, 12, 2, 21]. In particular, Fully Convolutional Networks (FCNs) that are based on transfer learning [16] have shown significant performance improvement over traditional computer vision approaches by large margins. In this case, the knowledge that is gained from image classification problem is adapted to dense spatial class prediction domain where each pixel in an image is marked with a class label. However, due to feature resolution reduction caused by consecutive pooling and strided convolution operations in the pre-trained models, this is a trade-off for the segmentation problem since the contextual details or some object boundaries are lost. To recover lost information, some methods [21, 2] used a skip-connection technique to injecting decoder features by using encoder features. This technique enables the network to learning and refining lost object boundaries by using low level features in a sense of previous knowledge can be incorporated with prior knowledge to help boosting the network learning.

Motivated by the recent success of deep neural networks, we propose a simple yet effective encoder-decoder type network that can be trained end-to-end in a supervised manner. The rest of this paper is organized as follows: a brief summary about previous works is described in Section 2, our method is described in Section 3, our segmentation results are described in Section 4, and conclusion in Section 5.

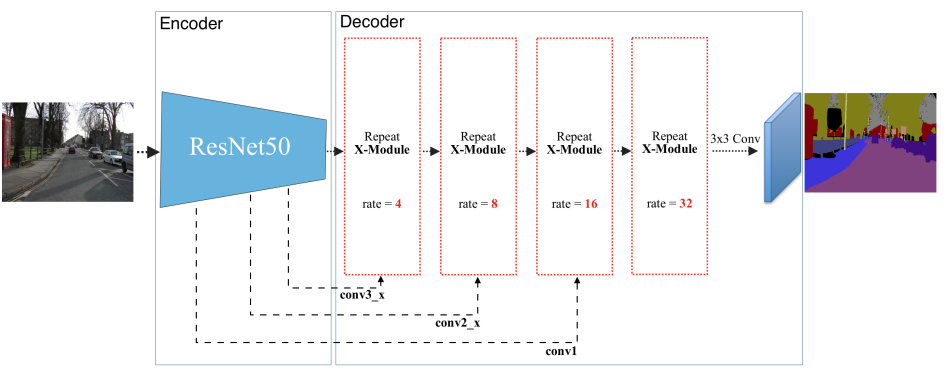


FIGURE 1. The flow of XSeNet architecture.

## 2. Related Works

Motivated by significant improvement of deep neural networks, most researchers explore the capabilities of such networks in semantic segmentation domain which make this domain improved over times. Recently, the FCNs was proposed by authors in [16] in semantic segmentation domain. The authors cast fully connected layers of the pre-trained network; i.e. AlexNet [13], VGG-Net [22], and GoogLeNet [23] into fully convolutional forms. The in-network upsampling and the skip architecture are introduced to refine the semantic outputs. Their method improves the

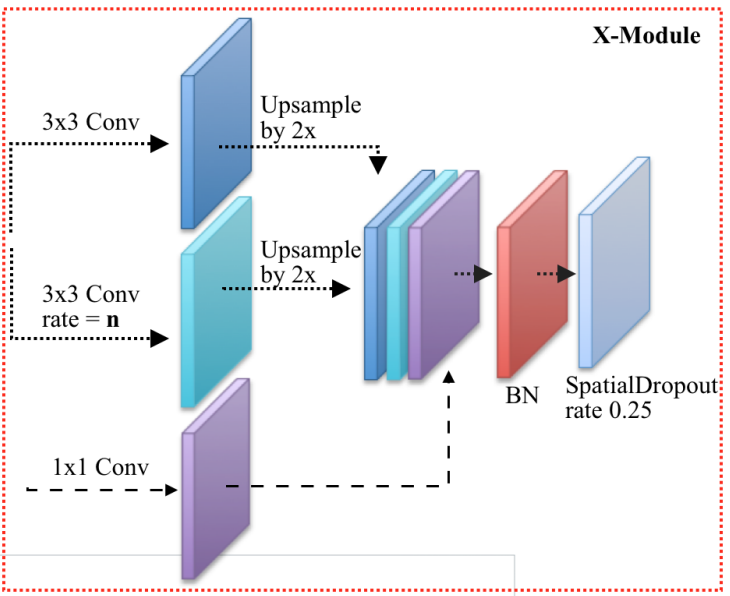


FIGURE 2. The X-Module

performance on several datasets such as Pascal VOC 2011-12 [7], SIFT Flow [15] etc. This work is considered as a milestone since the network can be trained end-to-end by taking input images of arbitrary sizes and producing dense predictions. Apart from this, a decoder approach is proposed by authors in [17] to mitigate the limitation of FCNs. In this work, the deconvolution layers and unpooling layers are embedded on top of the pre-trained classification model (VGG-16 Net) in a symmetric way. The network is applied to each object proposal in an input image, and then the resultant semantic outputs from all proposals were combined to construct the final segmentation output. This technique alleviates the limitation caused by the fixed receptive field of FCNs.

SegNet [2] is another state-of-the-art method and it is trained with CamVid dataset [3]. The network is composed of a decoder network embedded on top of the pre-trained VGG-Net. The decoder network consists of convolution layers and upsampling layers, where the max-pooling indices of the encoder network are used to perform non-linear upsampling in the decoder part. This network outperforms existing methods such as FCN [16] and DeconvNet [17].

Another recent encoder-decoder network is proposed by authors in [11]. In this work, the network is designed based on DenseNet [9] and trained from scratch without using any pre-trained networks. The proposed approach improves the state-of-the-art on CamVid and Gatech dataset [20]. Another efficient semantic segmentation method called ENet was proposed by [18]. The authors adopt the ideas of ResNet network [8] and specifically design the model for fast inferences and having low computational cost; yet, provides comparable results to existing methods. Authors in [1] proposed a residual coalesced convolutional network (RCC-Net) for video semantic segmentation problem. This encoder-decoder typed network architecture is designed based on the inspiration of ResNet model and Inception network [23]. For computational efficiency, the authors utilize an initial module to reducing the dimensionality of the input images into small feature maps before passing to the encoder network. Experimental results show that this network outperforms most of state-of-the-art methods. Authors in [25] proposed an encoder-decoder type recurrent neural network-based method to exploit contextual information from images and it provides promising results on various benchmarks.

Recently, authors in [19] proposed a two-branch network architecture which can segment high resolution images at 123.5fps that can be suited to efficient computation on embedded devices with low memory.

Moreover, dilated convolution or atrous convolution has been successfully used in semantic segmentation task [26, 5, 4, 6]. The idea of dilated convolution is to enlarge field-of-views in the network without learning extra parameters. To exploit this nice property, we also adopt this idea in our implementation.

## 3. Our Method

### 3.1. **Network Configuration.**

3.1.1. *The Encoder.* We adapt the pre-trained ResNet-50 [8], also known as ResNet 50 layers, and design a network architecture as depicted in Fig. 1 and Fig. 2. We utilize the first four blocks of ResNet-50 (conv1, conv2_x, conv3_x, conv4_x) and freeze all layers of the network, except the last identity block of conv4_x where we keep it for fine-tuning (for detailed ResNet network architecture, one may refer to the original paper). Skip connection technique has been successfully applied in image recognition task [8] to facilitate gradient flows through the network, and in semantic segmentation task [21] to allow the decoder to learn relevant features that are lost by pooling operations in the encoder part. Motivated by these ideas, we apply the skip layers in our implementation, and we found out that it makes the network converge faster and improves the accuracy.

3.1.2. *The Decoder.* Our decoder network (Fig. 2) contains four stacked modules, namely X-Module, where each module contains exactly the same configuration, except that the dilation rate is increased by a factor of two from the first module to

the last module. For each module, given a set of feature map $F$, two convolutional operations are operated in parallel:

(1) Firstly, a fixed receptive field 3x3-convolution with a stride of 1 is operated on a given feature map $F$ to produce a set of feature maps $M$ of size $H \times W \times 64$. Then the feature map $M$ is upsampled by a factor of 2 to produce a set of feature maps $M$ of size $H' \times W' \times 64$.

(2) Secondly, a dilated 3x3-convolution with a dilation rate $n$ and a stride of 1 is operated on the same feature map $F$ to produce a set of feature maps $N$ of size $H \times W \times 64$. Follow the same process, the feature map $N$ is upsampled by a factor of 2 to produce a set of feature maps $N$ of size $H' \times W' \times 64$.

(3) Thirdly, for the first, second and third module, a point-wise 1x1-convolution projects a set of high dimensional feature map depths in the encoder part to low dimension $P$ of size $H' \times W' \times 64$. Note that the skip weight-layers in conv2_x and conv3_x of the encoder part are taken from the last identity block (we pick the weight-layers right before BatchNormalization [10] and addition operation, from this identity block). There is no skip layer (dash-line layer) in the fourth module.

(4) Finally, feature map $M$, $N$ and $P$ are concatenated along the depth axis to produce $H' \times W' \times 192$ feature maps (since $64 \times 3 = 192$), except the fourth module where there is no skip layer $P$ is used. Note that the concatenated features are sequentially followed by BatchNormalization, ReLU, and SpatialDropout [24] layer. Then, the resultant feature maps are passed through the next layer.

**Further Analysis**: a fixed receptive field of normal 3x3-convolution can be interpreted as learning local features without incorporating global information into account, where dilated 3x3-convolution enables the network to have wider receptive fields that is significant for dense prediction by aggregating wide-ranged contextual information into account. In our implementation, these types of convolutional results are concatenated with previous knowledge in the encoder part, and then passed through the next layer to learning dense prediction. In each module (Fig. 2), since the concatenated feature map is a result of two convolutional operations that are operated on the same input, this concatenated feature map is expected to be strongly correlated. In this case, to alleviate overfitting, we apply the SpatialDropout right after this concatenated feature to drop correlated feature maps with a dropout rate of 25% and we found it to be effective in our implementation.

3.2. **Training Details.** In this work, we utilize CamVid dataset [3], which consists of 367 training, 101 validation, and 233 testing images at 360x480 resolution. The CamVid challenge is to segment scenes into 11 classes such as road, building, car, pedestrian, sidewalk, traffic sign etc. We train our network using the same training frames as described in [2].

We perform data augmentations to expanding the training sizes by horizontally flipping, rotating +10/-10 degrees. To make the network paying attention to the rare classes such as pole or traffic light, we perform zooming and cropping (to left and right) on the input image by focusing on those rare classes. Note that we

zoom the images to left and right in ratios of 100% and 200%, and then crop those images. To help the network paying attention to the rare class, we weight the classes differently by computing the class weights from entire training examples.

We train our network using Adam optimizer with a batch size of 1, setting the learning rate to 1e-3 and training by 15 epochs. We reduce the learning rate by a factor of 5 when the minimum validation loss stops improving for 5 epochs. Early stopping is applied when the minimum validation loss stops improving (min_delta equals to 1e-4) for 10 epochs. A softmax cross entropy loss is used in our training. Note that we resize the training images to a resolution of 352x480 in this experiment.

## 4. Results and Discussion

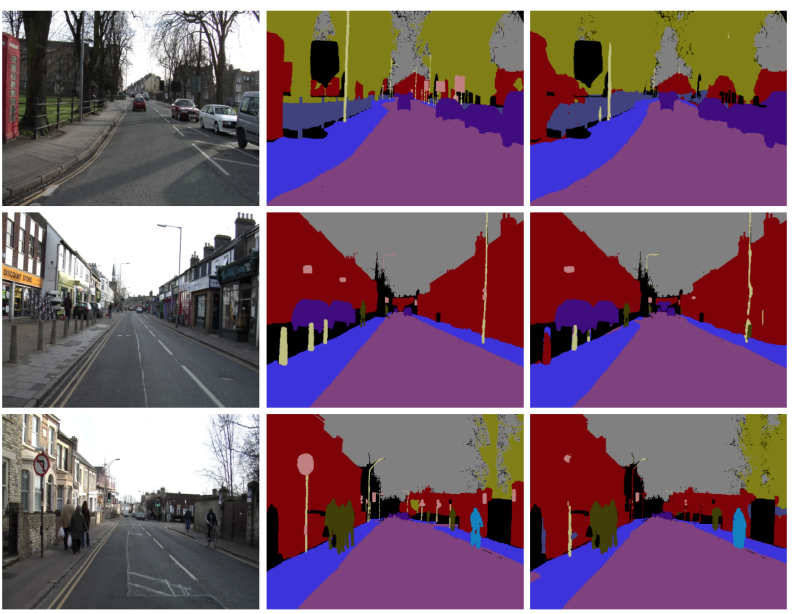

Figure 3. Our test results on CamVid dataset. First, second, and third column show input images, ground-truths, and our test results, respectively.

We measure the performance using three metrics followed the work in [2]; i.e. percentage of pixels correctly classified (G), mean predicted accuracy over all classes or class average accuracy (C), and mean intersection over all classes (mIoU).

Our test results and comparisons are depicted in Table 1. As can be seen, our method outperforms all listed methods by some margins. We also depict our segmentation results in Fig. 3 and Fig. 4. Most parts of the scenes are correctly classified by our method, especially major classes such as road, building, tree or car

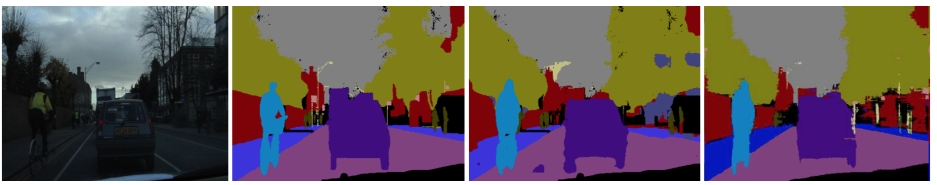


FIGURE 4. A comparison with the top model listed in Table 1. First, second, third, and fourth column show input images, ground-truths, our test results, and ReSeg results [25], respectively.

etc. One remarkable thing is that it is capable of distinguishing between bicyclists and pedestrians (Fig. 3, last row), where it is the failed case of other methods. This improvement may cause by aggregating contextual information using dilated convolution. However, it fails to detect rare classes, i.e. traffic lights and poles, where they share similar color intensities with the scene and it may be caused by the imbalanced data problem. Similarly, in the challenging scenario (dark scene), our method produces comparable results compared to the top listed model (Fig. 4).

TABLE 1. The *test results* on CamVid dataset and comparisons with the state-of-the-art methods. (G: Percentage of pixels correctly classified, C: Mean predicted accuracy over all classes, mIoU: Mean intersection over all classes.)

| Methods | G | C | m-IoU |
|---|---|---|---|
| **XSeNet (ours)** | 90.15 | 74.08 | 62.98 |
| ReSeg [25] | 88.70 | 68.10 | 58.80 |
| RCC-Net [1] | – | 71.50 | 53.30 |
| ENet [18] | – | 68.30 | 51.30 |
| SegNet [2] | 88.60 | 65.90 | 50.20 |
| DeconvNet [17] | 85.60 | – | 48.90 |
| SegNet-Basic [2] | 84.20 | 56.50 | 47.70 |
| FCN [16] | 83.50 | 57.30 | 47.00 |

## 5. CONCLUSION

In this research, we propose a novel network architecture and apply some useful techniques that significantly improve the segmentation results. We included four stacked X-Modules, all of which have exactly the same architectural configurations, except for the increased dilation rates. This configuration increases the receptive field size and helps better aggregating the contextual information without

creating additional burden to the architecture. Our method produces good results and outperforms previous state-of-the-art methods in all metrics. We believe that our method can be improved further by increasing the layers in our network, i.e. ResNet-101 and ResNet-152 layers, or by replacing the pre-trained architecture (ResNet-50) with dilated residual networks [27], since this network is designed to alleviate the problem of losing relevant information when applying pooling operations. We will investigate the optimal solution for the aforementioned problems in our future research.

## References


1. Igi Ardiyanto and Teguh Bharata Adji, *Deep residual coalesced convolutional network for efficient semantic road segmentation*, IPSJ Transactions on Computer Vision and Applications **9** (2017), no. 1, 6.
2. Vijay Badrinarayanan, Alex Kendall, and Roberto Cipolla, *Segnet: A deep convolutional encoder-decoder architecture for image segmentation*, arXiv preprint arXiv:1511.00561 (2015).
3. Gabriel J Brostow, Julien Fauqueur, and Roberto Cipolla, *Semantic object classes in video: A high-definition ground truth database*, Pattern Recognition Letters **30** (2009), no. 2, 88–97.
4. Liang-Chieh Chen, George Papandreou, Iasonas Kokkinos, Kevin Murphy, and Alan L Yuille, *Deeplab: Semantic image segmentation with deep convolutional nets, atrous convolution, and fully connected crfs*, IEEE transactions on pattern analysis and machine intelligence **40** (2018), no. 4, 834–848.
5. Liang-Chieh Chen, George Papandreou, Florian Schroff, and Hartwig Adam, *Rethinking atrous convolution for semantic image segmentation*, arXiv preprint arXiv:1706.05587 (2017).
6. Liang-Chieh Chen, Yukun Zhu, George Papandreou, Florian Schroff, and Hartwig Adam, *Encoder-decoder with atrous separable convolution for semantic image segmentation*, arXiv preprint arXiv:1802.02611 (2018).
7. Mark Everingham, Luc Van Gool, Christopher KI Williams, John Winn, and Andrew Zisserman, *The pascal visual object classes (voc) challenge*, International journal of computer vision **88** (2010), no. 2, 303–338.
8. Kaiming He, Xiangyu Zhang, Shaoqing Ren, and Jian Sun, *Deep residual learning for image recognition*, Proceedings of the IEEE conference on computer vision and pattern recognition, 2016, pp. 770–778.
9. Gao Huang, Zhuang Liu, Laurens Van Der Maaten, and Kilian Q Weinberger, *Densely connected convolutional networks.*, CVPR, vol. 1, 2017, p. 3.
10. Sergey Ioffe and Christian Szegedy, *Batch normalization: Accelerating deep network training by reducing internal covariate shift*, arXiv preprint arXiv:1502.03167 (2015).
11. Simon Jégou, Michal Drozdzal, David Vazquez, Adriana Romero, and Yoshua Bengio, *The one hundred layers tiramisu: Fully convolutional densenets for semantic segmentation*, Computer Vision and Pattern Recognition Workshops (CVPRW), 2017 IEEE Conference on, IEEE, 2017, pp. 1175–1183.
12. Andrej Karpathy and Li Fei-Fei, *Deep visual-semantic alignments for generating image descriptions*, Proceedings of the IEEE Conference on Computer Vision and Pattern Recognition, 2015, pp. 3128–3137.
13. Alex Krizhevsky, Ilya Sutskever, and Geoffrey E Hinton, *Imagenet classification with deep convolutional neural networks*, Advances in neural information processing systems, 2012, pp. 1097–1105.
14. Yann LeCun, Léon Bottou, Yoshua Bengio, and Patrick Haffner, *Gradient-based learning applied to document recognition*, Proceedings of the IEEE **86** (1998), no. 11, 2278–2324.

15. Ce Liu, Jenny Yuen, and Antonio Torralba, *Sift flow: Dense correspondence across scenes and its applications*, IEEE transactions on pattern analysis and machine intelligence **33** (2011), no. 5, 978–994.
16. Jonathan Long, Evan Shelhamer, and Trevor Darrell, *Fully convolutional networks for semantic segmentation*, Proceedings of the IEEE Conference on Computer Vision and Pattern Recognition, 2015, pp. 3431–3440.
17. Hyeonwoo Noh, Seunghoon Hong, and Bohyung Han, *Learning deconvolution network for semantic segmentation*, Proceedings of the IEEE international conference on computer vision, 2015, pp. 1520–1528.
18. Adam Paszke, Abhishek Chaurasia, Sangpil Kim, and Eugenio Culurciello, *Enet: A deep neural network architecture for real-time semantic segmentation*, arXiv preprint arXiv:1606.02147 (2016).
19. Rudra PK Poudel, Stephan Liwicki, and Roberto Cipolla, *Fast-scnn: fast semantic segmentation network*, arXiv preprint arXiv:1902.04502 (2019).
20. S Hussain Raza, Matthias Grundmann, and Irfan Essa, *Geometric context from videos*, Computer Vision and Pattern Recognition (CVPR), 2013 IEEE Conference on, IEEE, 2013, pp. 3081–3088.
21. Olaf Ronneberger, Philipp Fischer, and Thomas Brox, *U-net: Convolutional networks for biomedical image segmentation*, International Conference on Medical image computing and computer-assisted intervention, Springer, 2015, pp. 234–241.
22. Karen Simonyan and Andrew Zisserman, *Very deep convolutional networks for large-scale image recognition*, arXiv preprint arXiv:1409.1556 (2014).
23. Christian Szegedy, Wei Liu, Yangqing Jia, Pierre Sermanet, Scott Reed, Dragomir Anguelov, Dumitru Erhan, Vincent Vanhoucke, and Andrew Rabinovich, *Going deeper with convolutions*, Proceedings of the IEEE conference on computer vision and pattern recognition, 2015, pp. 1–9.
24. Jonathan Tompson, Ross Goroshin, Arjun Jain, Yann LeCun, and Christoph Bregler, *Efficient object localization using convolutional networks*, Proceedings of the IEEE Conference on Computer Vision and Pattern Recognition, 2015, pp. 648–656.
25. Francesco Visin, Marco Ciccone, Adriana Romero, Kyle Kastner, Kyunghyun Cho, Yoshua Bengio, Matteo Matteucci, and Aaron Courville, *Reseg: A recurrent neural network-based model for semantic segmentation*, Proceedings of the IEEE Conference on Computer Vision and Pattern Recognition Workshops, 2016, pp. 41–48.
26. Fisher Yu and Vladlen Koltun, *Multi-scale context aggregation by dilated convolutions*, arXiv preprint arXiv:1511.07122 (2015).
27. Fisher Yu, Vladlen Koltun, and Thomas A Funkhouser, *Dilated residual networks.*, CVPR, vol. 2, 2017, p. 3.
28. Matthew D Zeiler and Rob Fergus, *Visualizing and understanding convolutional networks*, European conference on computer vision, Springer, 2014, pp. 818–833.

*Current address*: Long Ang Lim: Ankara University, Department of Computer Engineering, Ankara TURKEY

*E-mail address*: lim.longang@gmail.com

*Current address*: Hacer Yalim Keles (Corresponding author): Ankara University, Department of Computer Engineering, Ankara, TURKEY

*E-mail address*: hkeles@ankara.edu.tr

ORCID: http://orcid.org/0000-0002-1671-4126

Commun.Fac.Sci.Univ.Ank.Series A2-A3
Volume 62, Number 1, Pages 35-52 (2020)
DOI: 10.33769/aupse.676443
ISSN 1303-6009 E-ISSN 2618-6462
http://communications.science.ankara.edu.tr/index.php?series=A2A3

# A STUDY ON THE SEARCH POTENTIAL OF DOUBLY CHARGED LEPTONS AT THE SppC BASED *ep* COLLIDERS

A. OZANSOY and O. ALBAYRAK

ABSTRACT. We consider the single production of doubly charged leptons which take part in the extended weak isospin models and have exotic electric charges such as $Q = \pm 2e$ at the SppC based electron-proton (*ep*) colliders. We introduce the effective lagrangians describing the doubly charged lepton gauge interactions with SM leptons. We calculate the decay widths and production cross sections as a function of doubly charged lepton mass. We deal with the $e^- p \to e^- W^- X$ process and plot the kinematical distributions for the final state electron both for the signal and corresponding background. We perform a cut-based analysis to obtain the mass limits and couplings of doubly charged leptons at the SppC based *ep* colliders with the center-of-mass energies of $\sqrt{s} = 8.44$ TeV and $\sqrt{s} = 26.68$ TeV.

## 1. INTRODUCTION

The Standard Model (SM) of particle physics has a structure with three families of matter particles. Apart from their masses, these families are exact repetition of the first family. SM has no answer for the fermionic family replication. On the other hand, the large number of the fundamental particles and free parameters in the SM bring to mind that question: Is it really a basic theory? Currently, although SM is very compatible with experiments, it is not the final word for particle physics, but it can be considered as the low energy limit of a more fundamental theory. It is clear that theories beyond the SM (BSM) must be envisaged.

Compositeness is one of the BSM theories which is a reasonable candidate to be capable of answering these questions. In composite models, it is considered that there could be one more layer of matter constituents called preons and SM fermions are bound states of preons [1-8]. At the scale of preon binding energies new

Received by the editors: January 17, 2020; Accepted: February 03, 2020.
*Key word and phrases:* Doubly charged leptons, compositeness scale, electron-proton colliders, weak isospin.

interactions among leptons and quarks may emerge. If leptons and quarks have a composite structure, excited states should be observed. Spin and isospin-1/2 excited fermions are considered as lowest radial and orbital excited states. Excited leptons with weak isospin states $I_W = 0$ (singlet) and $I_W = 1/2$ (doublet) are studied widely in the literature [9- 25].

If we take into account the weak isospin invariance in the framework of compositeness, the weak isospin values can be extended to include the $I_W = 1$ (triplet) and $I_W = 3/2$ (quadruplet) multiplets. These exotic multiplets have new particles (excited leptonic states) with exotic charges $Q = \pm 2e$ and they are called doubly charged leptons [26]. If a signal for the doubly charged lepton is observed in the next generation of colliders, this will provide us pioneering information about the SM family repetition and flavor structure.

The experimental data coming from the Large Hadron Collider (LHC) is quite compatible with the SM and there is no new physics signal of $\sim O$ (a few) TeV (by referring to the LHC energies). To go far beyond the scope of the LHC, designing for the installation of high energy and high luminosity colliders has become very important. Future Circular Collider (FCC) is a 100 TeV center-of-mass energy *pp* collider studied at CERN for the post-LHC era. It is an international project and supported by European Union within the Horizon 2020 Framework for Research and Innovation. The FCC's Conceptual Design Report (CDR) was completed in 2019 and published as four volumes [27-30]. The FCC is planned to be 4 times the LHC in size and bigger than the LHC energy about 7 times.

Another important post-LHC project is Super proton-proton Collider (SppC) project [31]. SppC is the Chinese analog of the FCC with the center-of-mass energy about 70 TeV. The CDR of the project which has two volumes was published in 2018 [32-33]. The first stage of the project will be an electron-positron collider called Circular Electron Positron Collider (CEPC) with a center-of-mass energy of 240 GeV. After this stage is completed, a *pp* collider of approximately 70 GeV in the same tunnel will go into operation.

Except from the compositeness doubly charged leptonic states are encountered in other BSM models, (for example in Type II seesaw mechanisms, some extensions of supersymmetric models, string inspired models etc.), too [34-44]. In the literature there are phenomenological studies for the doubly charged leptons at the LHC [45-54], at the future $e^+e^-$ and $e\gamma$ colliders [55-58], and at the future lepton-proton colliders [59-61]. The first limits for the mass of doubly charged leptons in *ep* collisions obtained as like that, for $L_{int} > 10^4$ fb$^{-1}$, $M_L > 860$ (1280) GeV at $\sqrt{s} = 1.3$ (1.98) TeV in [59].

In this work, we give the effective lagrangians responsible for the gauge interactions of doubly charged leptons predicted by the extended weak isospin model and calculate the decay widths for different values of compositeness scale ( $\Lambda$) in Section 2. In Section 3, we introduce the SppC based *ep* colliders. We give our analysis for the search potential of the SppC based *ep* colliders in Section 4 and then we conclude.

## 2. Doubly Charged Leptons In The Extended Weak Isospin Model

Long before the experimental verification of hadronic constituents (quarks and gluons), the strong isospin symmetry provided important information for understanding the patterns and properties of the hadron resonances. By analogy, the structure of possible fermionic resonances can be understood using the weak isospin ($I_W$) symmetry. In this way, the quantum numbers of possible excited fermionic states could be obtained without needing the dynamics of the preons explicitly. Since, right-handed SM fermions are in singlets ($I_W = 0$), left-handed SM fermions are in doublets ($I_W = 1/2$) and gauge bosons have $I_W = 0$ (for photon and gluon) or 1 (for $W^{\pm}$ and $Z$ bosons); allowed weak isospin values for excited fermionic states can be $I_W \leq 3/2$. Basic principles of extended weak isospin model are discussed in [26]. In the extended weak isospin model, weak isospin multiplets are extended to $I_W = 1$, 3/2. In these exotic multiplets doubly charged leptons with electric charge $Q$=-2*e* appear in triplets ($I_W = 1$) and in quadruplets ($I_W = 3/2$). In Eq. 1 the form of these exotic multiplets are listed as

$$L_1 = \begin{pmatrix} L^0 \\ L^- \\ L^{--} \end{pmatrix}, \quad I_W = 1, \quad Y = -2$$

$$L_{3/2} = \begin{pmatrix} L^+ \\ L^0 \\ L^- \\ L^{--} \end{pmatrix}, I_W = 3/2, \quad Y = -1 \tag{1}$$

and similar for the antiparticles. Here, $L$ can stand for any kind of lepton flavor, $Y$ is the weak hypercharge. Since the weak hypercharge value for all gauge fields is $Y$=0, a given exotic multiplet couples through the gauge fields to a SM multiplet only with the same $Y$. Concerning the gauge invariance, the couplings of the doubly charged

leptons to SM leptons and gauge bosons have to be of anomalous magnetic moment type. Therefore, the only possible coupling of doubly charged leptons to SM fermions, including both $I_W=1$ and $I_W=3/2$ multiplets, takes place via *W*-boson. The effective Lagrangians describing the gauge interactions of doubly charged leptons with ordinary leptons are given as

$$\mathcal{L}_{GM}^{(1)} = i\frac{gf_1}{\Lambda}\left(\bar{L}\sigma_{\mu\nu}\partial^{\nu}W^{\mu}\frac{1+\gamma_5}{2}l\right)+h.c. \tag{2}$$

$$\mathcal{L}_{GM}^{(3/2)} = i\frac{gf_3}{\Lambda}\left(\bar{L}\sigma_{\mu\nu}\partial^{\nu}W^{\mu}\frac{1-\gamma_5}{2}l\right)+h.c. \tag{3}$$

As seen in Eq. 2 (Eq. 3), $I_W=1$ ($I_W=3/2$) multiplet couples to SM right-handed (left-handed) lepton, because of the fact that a certain exotic multiplet can couple via gauge fields to a SM multiplet with the same value of *Y*. In Eq. 2 and 3, *g* is the *SU*(2) coupling constant and it is equals to $g = g_e/\sin\theta_W$ where $g_e = \sqrt{4\pi\alpha}$. $f_1$ and $f_3$ are new coupling constants related to effective interactions of $I_W=1$ and $I_W=3/2$ multiplets, and they are usually set to 1 in the literature. If we want to obtain their exact values we have to take into consideration the model for compositeness. $\Lambda$ is the compositeness scale, and *L* and *l* stand for doubly charged lepton and SM lepton, respectively. $\sigma_{\mu\nu}$ is an antisymmetric tensor and it is equal to $\sigma_{\mu\nu} = i\left(\gamma_\mu\gamma_\nu - \gamma_\nu\gamma_\mu\right)/2$ where $\gamma_\mu$ being the Dirac matrices.

Since doubly charged leptons couple to the SM leptons only via the *W*-boson, the only decay mode is charged weak decay mode, so the branching ratio of the $L^{--} \to l^- W^-$ process is equals to one (BR(%)=100, in other words). Taking into account $f_1 = f_3 = f$, decay width values for the doubly charged leptons both for the Lagrangians $\mathcal{L}_{GM}^{(1)}$ and $\mathcal{L}_{GM}^{(3/2)}$ are the same. The decay width of the doubly charged lepton with respect to its mass ($M_L$) for $f_1=f_3=1$ is given in Table 1 for two different values of $\Lambda$.

**Table 1.** Total decay width of doubly charged lepton as a function of its mass for $\Lambda=M_L$ and $\Lambda=5$ TeV.

| $M_L$(GeV) | Γ (GeV) | |
|---|---|---|
| | **$\Lambda=M_L$** | **$\Lambda=5$ TeV** |
| 500 | 4.21 | 0.0042 |
| 1000 | 8.68 | 0.35 |
| 1500 | 13.10 | 1.17 |
| 2000 | 17.49 | 2.79 |
| 2500 | 21.89 | 5.47 |
| 3000 | 26.68 | 9.45 |
| 3500 | 30.66 | 15.02 |
| 4000 | 35.05 | 22.43 |

## 3. SppC Based *ep* Colliders

Construction of a linear electron accelerator tangential to the proton ring can give the opportunity to collide the electrons and protons. It should be emphasized here that the electron accelerator should be linear since it will be very difficult to reach high energies due to the synchrotron radiation in circular electron accelerators. The advantages and physics potential of the linac-ring type colliders are discussed in [62-63]. Hadron Electron Ring Accelerator (HERA), the only *ep* collider ever operated, has shown that *ep* colliders are competitive to *pp* and *ee* colliders and are very important for BSM physics research. The Large Hadron electron Collider (LHeC) would be the second *ep* collider with the center-of mass energies 1.3 and 1.98 TeV after the HERA [64-65]. Also FCC would have an *ep* option [27]. Recently, using the parameters of the well-known future linear electron accelerator projects, SppC-based various *ep* colliders proposed in [66]. The main parameters of four different options of the SppC-based *ep* colliders are given in Table 2.

**Table 2.** Main parameters of the SppC-based *ep* colliders. (*These values are obtained from* [66]).

| $E_e$ (TeV) | $E_p$ (TeV) | $\sqrt{s}$ (TeV) | $L_{ep}$ ($cm^{-2}s^{-1}$) |
|---|---|---|---|
| 0.5 | 35.6 | 8.44 | $2.51\times10^{31}$ |
| 0.5 | 68 | 11.66 | $6.45\times10^{31}$ |
| 5 | 35.6 | 26.68 | $7.37\times10^{30}$ |
| 5 | 68 | 36.88 | $1.89\times10^{31}$ |

## 4. Analysis

Doubly charged leptons can be produced singly through the process $e^- p \to L^{--} X$ at *ep* colliders. The Feynman diagrams representing the related subprocess $e^- q(\bar{q}') \to L^{--} q'(\bar{q})$ are given in Figure 1.


Figure 1. Feynman diagrams for the subprocess $e^- q(\bar{q}') \to L^{--} q'(\bar{q})$.

For the sake of simplicity, we have considered only $I_W$=1 multiplet in our analysis. One of the authors of this paper has showed in [61] that single production cross section for $I_W$=3/2 multiplet differs slightly from $I_W$=1 multiplet at *ep* colliders. We implemented the doubly charged lepton interaction vertices in high-energy simulation programme CalcHEP [67-69] and used it for our calculations both for signal and background.

Total production cross section for the single production of doubly charged leptons ($e^- p \to L^{--} X$) at *ep* colliders with center-of-mass energies $\sqrt{s} = 8.44$ TeV and $\sqrt{s} = 26.68$ TeV for $\Lambda$=$M_L$ and $f_l$=1 is shown in Figure 2. To obtain the total cross section we have used the CTEQ6L parton distribution function [70].

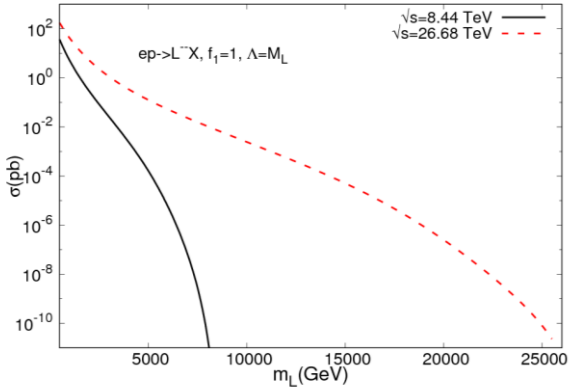


FIGURE 2. Total cross section for the single production of doubly charged leptons at two different SppC-based *ep* colliders.

After the decay of $L^{--}$, we deal with the $eq(\bar{q}') \to eW^{-}q'(\bar{q})$ subprocess. Here we respect the lepton family number conservation. We apply the same generic cuts for the final state electron and jets as

$$p_T^{e,j} > 20\ GeV \tag{4}$$

By applying the generic cuts, we get the some kinematical distributions of the final state electron. There is no more cut on jets. We show normalized transverse momentum ($p_T$) and normalized pseudorapidity ($\eta$) distributions for $\sqrt{s} = 8.44$ TeV and $\sqrt{s} = 26.68$ TeV in Figures 3 and 4, respectively.

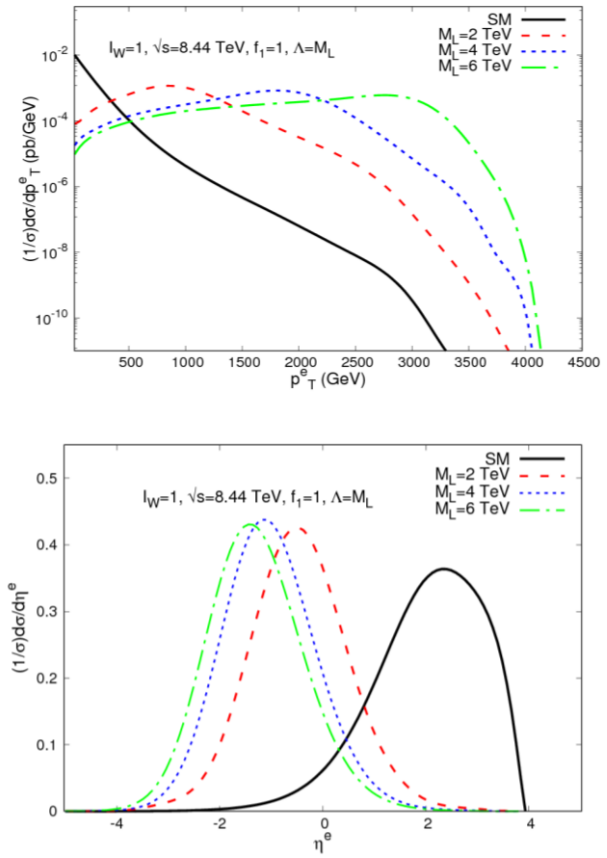


FIGURE 3. Normalized $p_T$ and $\eta$ distributions for the final state electron at $\sqrt{s}$ =8.44 TeV.

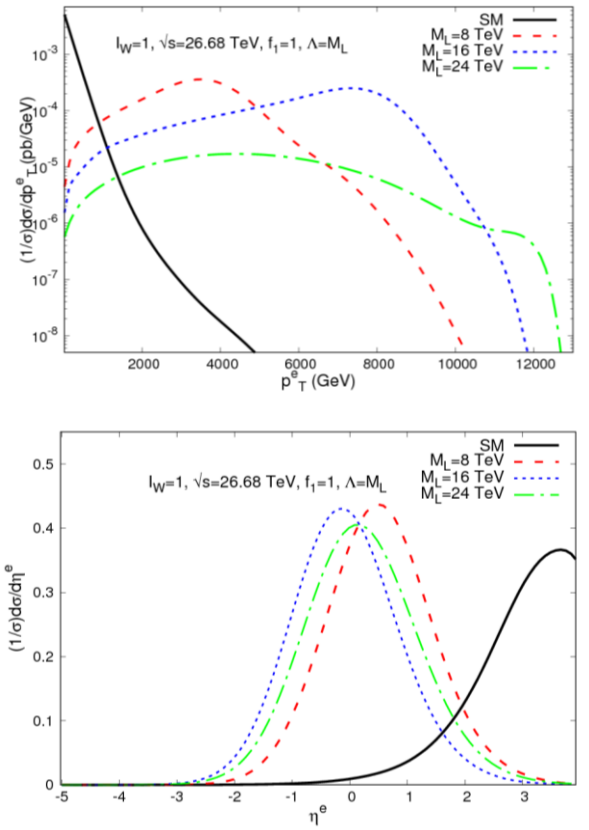


FIGURE 4. Normalized $p_T$ and $\eta$ distributions for the final state electron at $\sqrt{s}$ =26.68 TeV.

We obtain the discovery cuts by examining these kinematical distributions. We search for the areas which we largely remove the background but not affect the signal much. These discovery cuts are presented in Table 3.

**Table 3.** Discovery cuts for the doubly charged lepton production at the SppC-based *ep* colliders.

| $\sqrt{s}$ (TeV) | $p_T^e$ cut | $\eta^e$ cut |
|---|---|---|
| 8.44 | $p_T^e > 320$ GeV | $-3.2 < \eta^e < 0.8$ |
| 26.68 | $p_T^e > 870$ GeV | $-2.2 < \eta^e < 2$ |

We give the signal and background cross sections before and after the discovery cuts in Table 4 and 5 for $\sqrt{s} = 8.44$ TeV and $\sqrt{s} = 26.68$ TeV, respectively; and it is easily seen from these values that we have reached what we want. The signal cross sections show almost no change after applying the obtained discovery cuts.

**Table 4.** Signal and background cross sections before and after applying the discovery cuts for $\sqrt{s} = 8.44$ TeV

| $M_L$ (TeV) | $\sigma_S$ (pb) | | $\sigma_B$ (pb) | |
|---|---|---|---|---|
| | **Before cuts** | **After cuts** | **Before cuts** | **After cuts** |
| 2 | $1.21\times10^{-1}$ | $1.12\times10^{-1}$ | 15.39 | 0.34 |
| 4 | $1.38\times10^{-3}$ | $1.34\times10^{-3}$ | | |
| 6 | $6.03\times10^{-6}$ | $5.88\times10^{-6}$ | | |

**Table 5.** Signal and background cross sections before and after applying the discovery cuts for $\sqrt{s} = 26.68$ TeV

| $M_L$ (TeV) | $\sigma_S$ (pb) | | $\sigma_B$ (pb) | |
|---|---|---|---|---|
| | **Before cuts** | **After cuts** | **Before cuts** | **After cuts** |
| 8 | $4.90\times10^{-3}$ | $4.50\times10^{-3}$ | 60.48 | 0.105 |
| 16 | $1.32\times10^{-5}$ | $1.29\times10^{-5}$ | | |
| 24 | $1.97\times10^{-8}$ | $1.91\times10^{-8}$ | | |

We choose the hadronic decay mode of *W*-boson as $W \to 2j$. We define the statistical significance (*SS*) of the expected signal yield as

$$SS = \frac{|\sigma_{S+B} - \sigma_B|}{\sqrt{\sigma_B}} \sqrt{L_{\text{int}}} \tag{5}$$

where $\sigma_{S+B}$ is the cross section due to the all contributions of SM and doubly charged lepton, and $\sigma_B$ is the SM background cross section, respectively; $L_{int}$ is the integrated luminosity of the collider. We obtain $L_{int,}$ by multiplying the average instantaneous luminosity of the collider given in Table 1 by the factor $10^7$ which is the operating time of the collider for approximately 1 year.

In Figure 5, we show the *SS* - $M_L$ plots for the SppC-based *ep* colliders, indicating the $2\sigma$ (exclusion), $3\sigma$ (observation), and $5\sigma$ (discovery) regions, respectively. In Table 6, we list the obtained mass limits for doubly charged leptons at the SppC-based *ep* colliders for $f_l$=1 and $\Lambda$=$M_L$, taking into account the criteria $SS \geq 2$, $SS \geq 3$ and $SS \geq 5$ which denote the $2\sigma$, $3\sigma$ and $5\sigma$ limits, respectively.

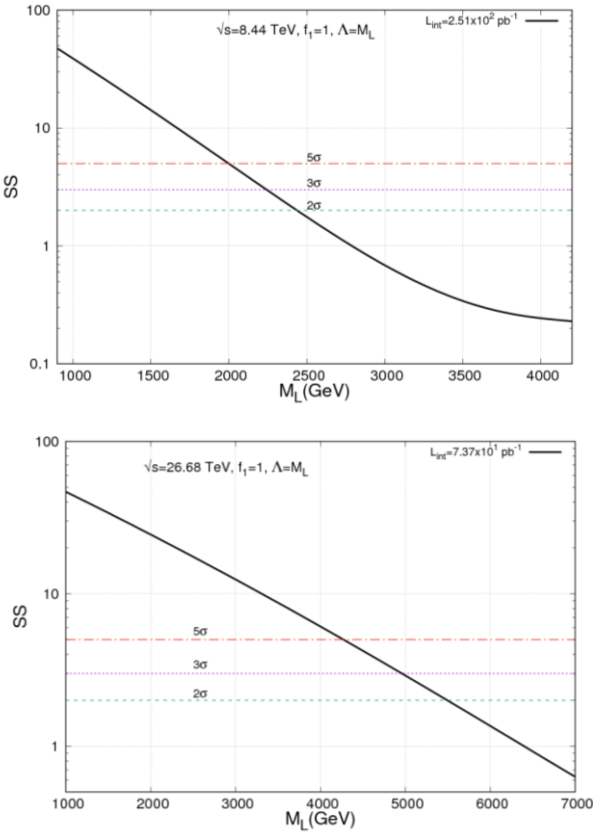

FIGURE 5. *SS* as a function of $M_L$ for the SppC-based *ep* colliders.

**Table 6.** Mass limits for doubly charged leptons at the SppC based *ep* colliders for $\Lambda=M_L$ and $f_l=1$.

| **√s (TeV)** | **$L_{int}$ ($pb^{-1}$)** | **2σ (Exclusion) (TeV)** | **3σ (Observation) (TeV)** | **5σ (Discovery) (TeV)** |
|---|---|---|---|---|
| 8.44 | $2.51 \times 10^2$ | 2.19 | 2.00 | 1.75 |
| 26.68 | $7.37 \times 10^3$ | 4.30 | 3.85 | 3.30 |

By using the same discovery cuts we plot the contour plots at $\Lambda$-$M_L$ parameter space. We show our contour plots in Figure 6. From these figures we deduce the observation (3σ) limits for the Λ as Λ~ 2.6 (4) )TeV for $M_L$=1.75 (3.30) TeV at $\sqrt{s}$ = 8.44 (26.68) TeV.

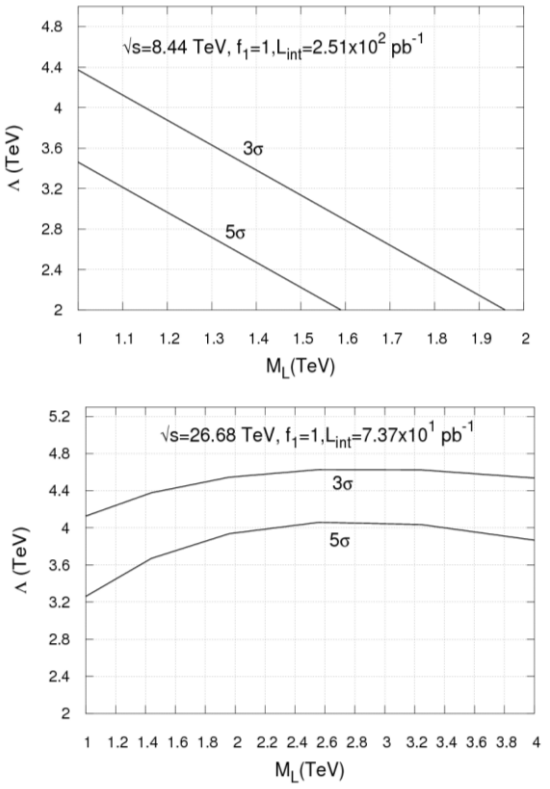


FIGURE 6. Contour plots at the Λ-$M_L$ parameter space for the SppC-based *ep* colliders.

## 5. CONCLUSION

Using weak isospin invariance may help us to investigate the properties of possible fermionic resonances. Thus, a new perspective on compositeness is developed. In extended weak isospin model, the usual weak isospin multiplets are extended to higher weak isospin multiplets namely, $I_W$ =1 (triplet) and $I_W$ =3/2 (quadruplet) multiplets. The doubly charged leptons are predicted in these exotic multiplets. SppC-based *ep* colliders will give an excellent environment to search for the doubly charged leptons. Taking into account the gauge interactions of doubly charged leptons with SM leptons and applying the cuts obtained from kinematical distributions, we have provided 2σ, 3σ and 5σ mass limits as 2.19 (4.30) TeV, 2.00 (3.85) TeV, and 1.75 (3.30) TeV, respectively at the SppC-based *ep* colliders at $\sqrt{s}$

= 8.44 (26.68) TeV for $\Lambda=M_L$ and $f_l=1$. Our results have showed that, SppC-based *ep* colliders can extend the limits for the doubly charged lepton mass nearly two times from those obtained from the *pp* colliders.

## References

[1] Terazawa H., Chikashige Y., and Akama K., Unified Model of the Nambu-Jona-Lasino Type for all Elementary Particle Forces, Phys. Rev. D 15-2 (1977) 480-487.

[2] Ne'eman Y., Primitive Particle Model, Phys. Lett. 82B-1 (1979) 69-70.

[3] Terazawa H., Yasue M., Akama K., and Hayashi M., Observable Effects of the Possible Sub-structure of Leptons and Quarks, Phys. Lett. 112B 4-5 (1982) 387-392.

[4] Renard F. M., Excited Quarks and New Hadronic States, Il Nuovo Cimento A 77-1 (1983) 1-20.

[5] Eichten E. J., Lane K. D., and Peskin M. E., New Tests for Quark and Lepton Substructure, Phys. Rev. Lett. 50-11 (1983) 811-814.

[6] de Rujula A., Maiani L., and Petronzio R., Search for Excited Quarks, Phys. Lett. 140B 3-4 (1984) 253-258.

[7] Cabibbo N., Maiani L., and Srivastava Y. N., Anomalous Z Decays: Excited Leptons?, Phys. Lett. 139B 5-6 (1984) 459-463.

[8] Kühn J. and Zerwas P. M., Excited Quarks and Leptons, Phys. Lett. 147B 1-3 (1984) 189-196.

[9] Hagiwara K., Komamiya S., and Zeppenfeld D., Excited Lepton Production at LEP and HERA, Z. für Physik C 29-1 (1985) 115-122.

[10] Boudjema F., Djouadi A., and Kneur J. L., Excited Fermions at $e^+e^-$ and eP Colliders, Z. für Physik C 57-3 (1993) 425-449.

[11] Cakir O., Yilmaz A., and Sultansoy S., Single Production of Excited Electrons at Future $e^+e^-$, ep and pp Colliders, Phys. Rev. D 70-7 (2004) 075011.

[12] Cakir O., Turk Cakir I., and Kirca Z., Single Production of Excited Neutrinos at Future $e^+e^-$, ep and pp Colliders Phys. Rev. D 70-7 (2004) 075017.

[13] Caliskan A., Kara S. O., and Ozansoy A., Excited Muon Searches at the FCC-Based Muon-Hadron Colliders, Adv. High Energy Phys. 2017 (2017) 1540243.

[14] Caliskan A., Excited Neutrino Search Potential of the FCC-Based Electron-Hadron Colliders, Adv. High Energy Phys. 2017 (2017) 4726050.

[15] Caliskan A. and Kara S. O., Single Production of the Excited Electrons at the Future FCC-Based Lepton-Hadron Colliders, Int. J. Mod. Phys. A 33-24 (2018) 1850141.

[16] Ginzburg I. F. and Ivanov D. Yu., Excited Leptons and Quarks at $\gamma\gamma$ / $\gamma e$ Colliders, Phys. Lett. B276 1-2 (1992) 214-218.

[17] Koksal M., Analysis of Excited Neutrinos at the CLIC, Int. J. Mod. Phys. A 29-24 (2014) 1450138.

[18] Ozansoy A. and Billur A. A., Search for Excited Electrons Through $\gamma\gamma$ Scattering, Phys. Rev. D 86-5 (2012) 055008.

[19] Kirca Z., Cakir O., and Aydin Z. Z., Production of Excited Electrons at TESLA and CLIC Based e gamma Colliders, Acta Phys. Polon. B 34-8 (2003) 4079.

[20] Eboli O. J., Lietti S. M., and Mathews P., Excited Leptons at the CERN Large Hadron Collider, Phys. Rev. D 65-7 (2002) 075003.

[21] Inan S. C., Exclusive Excited Leptons Search in Two Lepton Final States at the CERN LHC, Phys. Rev. D81-11 (2010) 115002.

[22] Cakir O., Leroy C., Mehdiyev R., and Belyaev A., Production and Decay of Excited Electrons at the LHC, Eur. Phys. J. C 32-2 (2004) s1-s17.

[23] Belyaev A., Leroy C., and Mehdiyev R., Production of Excited Neutrinos at the LHC, Eur. Phys. J. C 41-2 (2005) 1-10.

[24] Boos E., Volodgin A., Toback D., and Gaspard J., Prospects of Searching for Excited Leptons During Run II of the Fermilab Tevatron, Phys. Rev. D 66-1 (2002) 013011.

[25] Baur U., Spira M., and Zerwas P. M., Excited Quark and Lepton Production at Hadron Colliders, Phys. Rev. D 42-3 (1990) 815-824.

[26] Pancheri G. and Srivastava Y. N., Weak Isospin Spectroscopy of Excited Quarks and Leptons, Phys. Lett. 146B (1984) 87-94.

[27] Abada, A. et al, FCC Collaboration, FCC Physics Opportunities: Future Circular Collider Conceptual Design Report Volume 1, Eur. Phys. J. C79, no.6 (2019) 474.

[28] Abada, A. et al, FCC Collaboration, FCC-ee: The Lepton Collider: Future Circular Collider Conceptual Design Report Volume 2, Eur. Phys. J.ST 228 no.2, (2019) 261-623.

[29] Abada, A. et al, FCC Collaboration, FCC-hh: The Hadron Collider: Future Circular Collider Conceptual Design Report Volume 3, Eur. Phys. J.ST 228 no.4 (2019) 755-1107.

[30] Abada, A. et al, FCC Collaboration, HE-LHC: The High-Energy Large Hadron Collider: Future Circular Collider Conceptual Design Report Volume 4, Eur.Phys.J.ST 228 no.5 (2019) 1109-1382.

[31] Su F., Gao J., Xiao M., Wang D., Wang Y-W., Bai S., Bian T-J., Method Study of Parameter Choice for a Circular Proton-Proton Collider Chin. Phys. C 40-1 (2016) 017001.

[32] CEPC Study Group, “CEPC Conceptual Design Report: Volume 1 - Accelerator”, Conceptual Design Report, IHEP-CEPC-DR-2018-01, IHEP-AC-2018-01, arXiv preprint: 1809.00285(2018).

[33] CEPC Study Group, "CEPC Conceptual Design Report: Volume 2 - Physics & Detector", Conceptual Design Report, HEP-CEPC-DR-2018-02, IHEP-EP-2018-01, IHEP-TH-2018-01, arXiv preprint: 1811.10545 (2018)

[34] Chua C. K. and Law S. S. C., Phenomenological Constraints on Minimally Coupled Exotic Lepton Triplets, Phys. Rev D 83 (2011) 055010.

[35] Foot R., Lew H., He X. G., and Joshi G. C., Seesaw Neutrino Masses Induced by a Triplet of Leptons, Zür. Phys. C 44 (1989) 441-444.

[36] Kumericki K., Picek I., and Radovcic B., Exotic Seesaw-Motivated Heavy Leptons at the LHC, Phys. Rev. D 84 (2011) 093002.

[37] Demir D. A., Frank M., Huitu K., Kumar Rai S., and Turan I., Signals of Doubly-Charged Higgsinos at the CERN Large Hadron Collider, Phys. Rev. D 78 (2008) 035013.

[38] Franceschini M. and Mohapatra R., Radiatively Induced Type II Seesaw Models and Vectorlike 5/3 Charge Quarks, Phys. Rev. D 89-5 (2014) 055013.

[39] Dutta B., Mohapatra R. N., and Muller D. J., The Signature at the Tevatron for the Light Doubly Charged Higgsino of the Supersymmetric Left-Right Model, Phys. Rev. D 60 (1999) 095005.

[40] Chacko Z. and Mohapatra R. N., Supersymmetric Left-Right Model and Light Doubly Charged Higgs Bosons and Higgsinos, Phys. Rev. D 58 (1998) 015003.

[41] Frank M., Doubly Charged Higgsino Mediated Lepton Flavor Violating Decays, Phys. Rev. D 62 (2000) 053004.

[42] Cirelli M., Fornengo N., and Strumia A., Minimal Dark Matter, Nucl. Phys. B 753 (2006) 178-194.

[43] del Aguila F., de Blas J., and Perez-Victoria M., Effects of New Leptons in Electroweak Precision Data, Phys. Rev. D 78 (2008) 013010.

[44] Cvetic M., Halverson J., and Langacker P., Implications of String Constraints for Exotic Matter and Z' s Beyond the Standart Model, Journal of High Energy Phys. 1111 (2011) 058.

[45] Delgado A., Garcia Cely C., Han T., and Wang Z., Phenomenology of Lepton Triplet, Phys. Rev. D 84 (2011) 073007.

[46] Biondini S., Panella O., Pancheri G., Srivastava Y. N., and Fano L., Phenomenology of Excited Doubly Charged Heavy Leptons at the LHC, Phys. Rev. D 85 (2012) 095018.

[47] Alloul A., Frank M., Fuks B., and de Traubenberg M. R., Doubly-Charged Particles at the Large Hadron Collider, Phys. Rev. D 88 (2013) 075004.

[48] Leonardi R., Panella O., and Fano L., Doubly Charged Heavy Leptons at LHC via Contact Interactions, Phys. Rev. D 90-3 (2014) 035001.

[49] You Y., Chong-Xing Y., and Yun X., Pair Production of the Doubly Charged Leptons via Electroweak Vector Boson Fusion at the Large Hadron Collider, Chin. Phys. Lett. 31 (2014) 021201.

[50] Ma T., Zhang B., and Cacciapaglia G., Triplet with a Doubly-Charged Lepton at the LHC, Phys. Rev. D 89-1 015020 (2014); Doubly Charged Lepton from an Exotic Doublet at the LHC, Phys. Rev. D 89-9 (2014) 093022.

[51] Yu Y., Yue C-X., and Yang S., Signatures of the Quintuplet Leptons at the LHC, Phys. Rev. D 91-9 (2015) 093003.

[52] Okada H. and Yagyu K., Three-loop Neutrino Mass Model with Doubly Charged Particles from Isodoublets, Phys. Rev. D 93-1 (2016) 013004.

[53] Chen C-H. and Nomura T., Bounds on LFV Higgs Decays in a Vector-like Lepton Model and Searching for Doubly Charged Leptons at the LHC, Eur. Phys. J. C 76 (2016) 353.

[54] Leonardi R., Alunni L., Romeo F., Fano L., and Panella O., Hunting for Heavy Composite Majorana Neutrinos at the LHC, Eur. Phys. J. C 76 -11 (2016) 593.

[55] Zeng Q-G., Ji L., and Yang S., Pair Production of the Doubly Charged Leptons Associated with a Gauge Boson $\gamma$ or Z in $e^+e^-$ and $\gamma\gamma$ Collisions at Future Linear Colliders, Commun. Theor. Phys. 63-3 (2015) 331-339.

[56] Biondini S. and Panella O., Exotic Leptons at Future Linear Colliders, Phys. Rev. D 92-1 (2012) 015023.

[57] Guo Y-C., Yue C-X., Lui Z-C, The Signatures of Doubly Charged Leptons in Future Linear Colliders, J. Phys. G. Nucl. Part. Phys. 44 (2017) 085004.

[58] Zeng Q-G., Production of the Doubly Charged Leptons at the ILC, Eur. Phys. Lett. 111 (2105) 21003.

[59] Yu Y., Guo Y-C., Lui Z-C., Fan W-J., Mei Y., and Zhang J., The Signatures of Doubly Charged Leptons at LHeC, J. Phys. G. Nucl. Part. Phys. 45 (2018) 125003.

[60] Ozansoy A., Investigating Doubly Charged Leptons at the Future Energy Frontier Muon-proton Colliders, Communications Fac. Sci.Univ. Ank. Series A2-A3, 61,1 (2019) 111-128.

[61] Ozansoy A., Doubly Charged Lepton Search Potential of the FCC-Based Energy Frontier Electron-Proton Colliders, https://arxiv.org/abs/1912.07351 (2019).

[62] Sultansoy S., Four ways to Tev scale, Turkish Journal of Physics 22, no:1 (1998) 575-594.

[63] Sultansoy S., Linac-ring type colliders: second way to TeV scale, The European Phys. Journal 33, supplement 1 (2004) s1064-1066.

[64] Abelleira Fernandez J. L. et al. (LHeC Study Group), A Large Hadron Electron Collider at CERN, Journal of Phys. G 39 (2012) 075001.

[65] Bruening O. and Klein M., The Large Hadron Electron Collider, Mod. Phys. Lett. A 28 - 16 (2013) 1330011.

[66] Canbay A. C., Kaya U., Ketenoglu B., Oner B. B., and Sultansoy S., SppC based energy frontier lepton-proton colliders:luminosity and physics, Adv. in High Energy Phys. 2017 (2017) 4021493.

[67] Belyaev A., Christensen N. D., and Pukhov A., CalcHEP 3.4 for Collider Physics Within and Beyond the Standard Model, Computer Phys. Commun. 184-7 (2013) 1729-1769.

[68] Pukhov A., CalcHEP 2.3: MSSM, Structure Functions, Event Generation, Batchs, and Generation of Matrix Elements for other Packages, (2004) https://arxiv.org/abs/hep-ph/0412191.

[69] Pukhov A., Boos E., Dubinin M., Edneral V., Ilyin V., Kovalenko D., Kryukov A., Savrin V., Shichanin S., and Semenov A., CompHEP- a Package for Evaluation of Feynman Diagrams and Integration Over Multi-particle Phase Space. User's Manual for Version 33, (1999) https://arxiv.org/abs/hep-ph/9908288.

[70] Stump D., Huston J., Pumplin J., Tung W-K., Lai H. L., Kuhlmann S., and Owens J.F, Inclusive jet production, parton distributions and the search for new physics, JHEP 0310 (2003) 046.

*Current Address:* A. OZANSOY: Ankara University, Faculty of Sciences, Department of Physics, Ankara, TURKEY
*E-mail:* aozansoy@science.ankara.edu.tr
*Orcid ID:* https://orcid.org/0000-0002-9042-1372

*Current Address:* O. ALBAYRAK: Ankara University, Faculty of Sciences, Department of Physics, Ankara, TURKEY
*E-mail:* ouzhn06@hotmail.com
*Orcid ID:* https://orcid.org/0000-0002-4541-4385

Commun.Fac.Sci.Univ.Ank.Series A2-A3
Volume 62, Number 1, Pages 53-62 (2020)
DOI: 10.33769/aupse.676083
ISSN 1303-6009 E-ISSN 2618-6462
http://communications.science.ankara.edu.tr/index.php?series=A2A3

# BAND REDUCTION FOR TARGET DETECTION IN HYPERSPECTRAL IMAGES

MURAT ŞİMŞEK and HAKKI ALPARSLAN ILGIN

ABSTRACT. Due to the high spectral resolution, hyperspectral images need large data storage and processing time. Indeed, its high dimensional structure requires high computational complexity, especially for target detection. In order to overcome these problems, band reduction methods have been proposed. In this paper, we compare PCA and SNR-based band reduction methods to improve target detection performance in hyperspectral images. Experimental results show that band reduction methods not only reduce processing time, but also increase accuracy rate.

## 1. INTRODUCTION

Hyperspectral imaging collects image data simultaneously in hundreds of narrow and adjacent spectral bands. Owing to narrow contiguous spectral bands, hyperspectral images have detailed information about scene. Because of having large quantity of spectral information, hyperspectral images are used in many applications including remote sensing, mineral identification, environmental studies, surveillance, object classification and target detection. Although high spectral information allows us to distinguish various types of materials in scene, it increases processing time on account of large data size. Furthermore, large number of spectral bands increases complexity. Since hyperspectral images contain highly correlated spectral bands, their unnecessary information is excessive. Thus, dimensionality reduction methods have been developed which reduce the number of bands without losing the information content and also segregate noise in the data [1]. Fig. 1 shows a flow diagram of the band reduction.

Received by the editors: January 16, 2020; Accepted: February 10, 2020.
*Key word and phrases:* Hyperspectral image, band reduction, target detection.

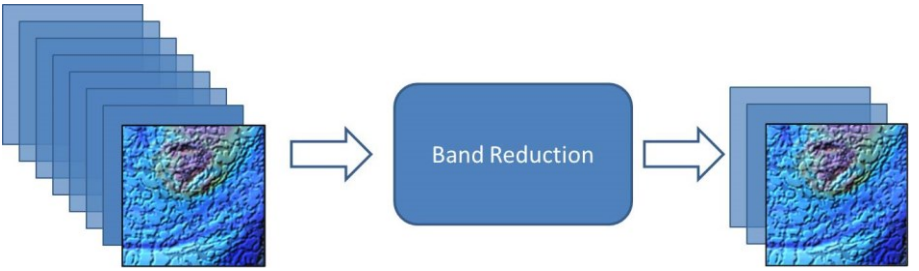


FIGURE 1. Band reduction flow diagram

Band reduction is an effective and necessary preprocessing phase for processing images in order to overcome problems caused by high size in hyperspectral images. Our aim is to obtain high accuracy percentage and low processing time with less data namely hyperspectral image band in target detection. Hyperspectral image is a three-dimensional data and consists of spectral bands each having a two-dimensional spatial image. Hyperspectral data cube used in the experimental studies is shown in Fig. 2.

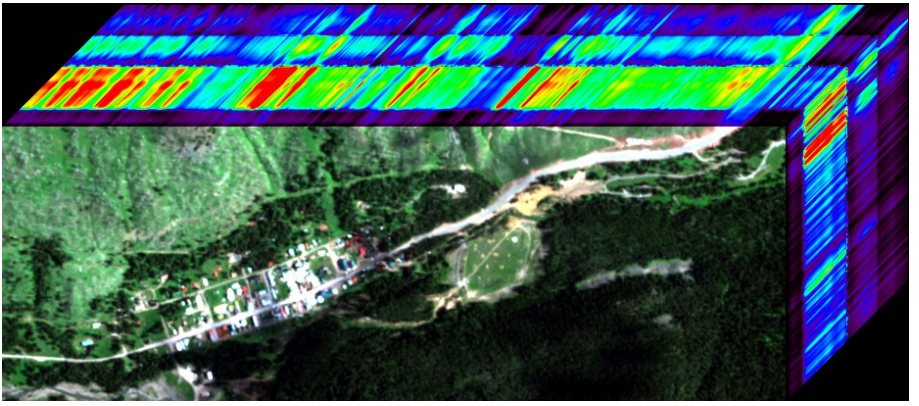

FIGURE 2. HyMap Hyperspectral Data Cube

Each band of hyperspectral image includes the responses of ground substances at a specific wavelength. Two spectral bands with different wavelengths of the hyperspectral image which is used in this study are shown in Fig. 3 [2].

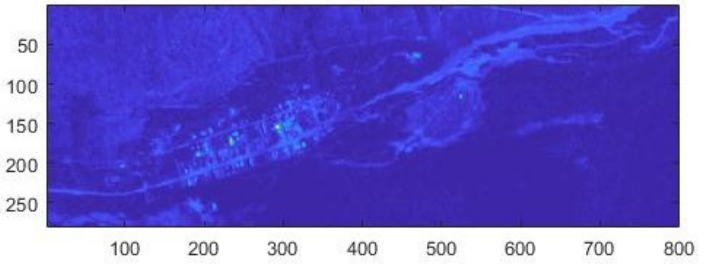


(a)

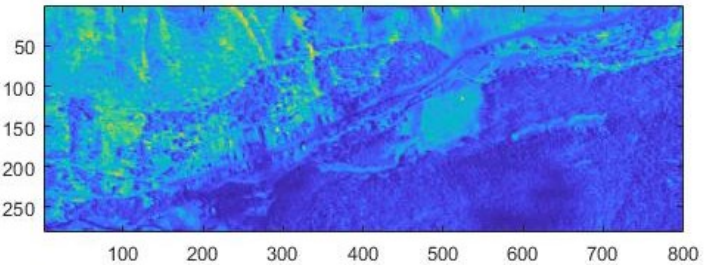


(b)

FIGURE 3. Spectral band examples of hyperspectral image (a) 15$^{th}$ band of hyperspectral image (b) 60$^{th}$ band of hyperspectral image

In the next section, Principle Component Analysis (PCA) and Signal-to-Noise Ratio (SNR)-based band reduction techniques are discussed. Comparison of these techniques and effect on target detection are examined in section 3. In the last section, conclusion and discussion are given.

## 2. BAND REDUCTION APPROACHES

There are several band reduction techniques for hyperspectral images each having different performance characteristics when combined with target detection methods. In this study, we consider two approaches, PCA and SNR-based band reduction methods, to increase target detection performance as well as to decrease processing time. In the following subsections PCA and SNR-based approaches are explained.

## 2.1. PCA Approach

In terms of remote sensing, PCA has been used in many areas. In this paper we use PCA for band reduction for target detection in hyperspectral images. The first small number of PCA bands generally include most of the information existing in hyperspectral image and therefore hyperspectral image bands and noise can be reduced effectively [3].

PCA utilizes the correlation which exists between neighboring spectral bands that generally contain the same information about the same object. PCA examines band dependence or correlation using statistical properties between the bands of hyperspectral image [4].

A hyperspectral image, which has *P* number of bands with *m* rows and *n* columns, namely *B*=*m*x*n* pixels, in each band, is defined as

$$\boldsymbol{H} = [\boldsymbol{h}_1, \boldsymbol{h}_2, \dots, \boldsymbol{h}_B]^T \tag{1}$$

where $\boldsymbol{h}_i$ is a pixel vector of the hyperspectral image at spatial point *i* which is given as

$$\boldsymbol{h}_i = [h_1, h_2, h_3, \dots, h_P]_i^T, i = 1, \dots, B \tag{2}$$

where $h_j$, {*j*=1,…,*P*} are pixel values at each band. The mean vector of all pixel vectors is

$$\boldsymbol{\mu} = \frac{1}{B}\sum_{i=1}^{B}[h_1, h_2, h_3, \dots, h_P]_i^T. \tag{3}$$

Covariance matrix is calculated as

$$\boldsymbol{C_H} = \frac{1}{B}\sum_{i=1}^{B}(\boldsymbol{h}_i - \boldsymbol{\mu})(\boldsymbol{h}_i - \boldsymbol{\mu})^T. \tag{4}$$

PCA is based on eigenvalue decomposition of covariance. Covariance matrix can be written as

$$\boldsymbol{C_H} = \boldsymbol{ADA}^T \tag{5}$$

where $\boldsymbol{D} = \mathrm{diag}(\lambda_1, \lambda_2, \lambda_3, \dots, \lambda_P)$ is the diagonal eigenvalue matrix where $\lambda_j$, {*j*=1,…,*P*} are eigenvalues and $\boldsymbol{A} = (\boldsymbol{a}_1, \boldsymbol{a}_2, \boldsymbol{a}_3, \dots, \boldsymbol{a}_P)$ is orthonormal eigenvector

matrix with orthonormal vectors $\boldsymbol{a}_j$, $\{j=1,\ldots,P\}$. Each PCA pixel vector after the transformation can be calculated as follows [5]:

$$\boldsymbol{y}_i = \boldsymbol{A}^T \boldsymbol{h}_i, \quad i = 1,2,\ldots,B \tag{6}$$

Each of the transformed pixel vectors contains the compressed information of the entire data set. While first few PCA bands have the highest variance, last bands have the lowest variance. Therefore, the first PCA bands generally contain most of the information in the original hyperspectral images. Since PCA is used to reduce number of bands to be used, it enables more efficient and accurate analysis [2]. It also eliminates noise since last bands are mostly noisy.

## 2.2. SNR-based Band Reduction Method

Hyperspectral imaging is very useful for remote sensing, but hyperspectral data is characterized by narrow bands affected by low SNR [6]. In this paper, Minimum Noise Fraction (MNF) algorithm is used as SNR-based band reduction method.

MNF is used to determine the dimensionality of image data, isolate noise in the data, and reduce computational requirements for subsequent operations [7]. MNF is based on separation of noise from information content in the image. MNF mainly consists of two steps. The first step associates and re-scales the noise in the data based on an estimated noise covariance matrix. Then a standard PCA is applied to the noise-whitened data [8].

Assuming that hyperspectral image matrix $\boldsymbol{H}$ consists of the sum of signal and noise;

$$\boldsymbol{H} = \boldsymbol{S} + \boldsymbol{N} \tag{7}$$

where $\boldsymbol{S}$ and $\boldsymbol{N}$ are the uncorrelated signal and additive noise, respectively. Therefore, covariance matrices are referred by

$$\boldsymbol{C}_{\boldsymbol{H}} = \boldsymbol{C}_{\boldsymbol{S}} + \boldsymbol{C}_{\boldsymbol{N}} \tag{8}$$

where $\boldsymbol{C}_S$ and $\boldsymbol{C}_N$ are noise and signal covariance matrices, respectively. MNF results in a new uncorrelated data set which is a linear transform of the original data $\boldsymbol{Y}$ which is given as

$$\boldsymbol{Y} = \boldsymbol{V}^T \boldsymbol{Z} \tag{9}$$

where $\boldsymbol{V}$ and $\boldsymbol{Z}$ are linear transformation matrix and zero-mean hyperspectral image, respectively. Row vectors in the zero-mean dataset $\boldsymbol{Z}$ are found by subtracting the row vectors of $\boldsymbol{H}$ from their means [9]. The first row vector of $\boldsymbol{Y}$ contains the signal components without noise. However, the other rows contain noisy signal components. In other words, as the number of lines increases, noisy signal components increase. SNR of each hyperspectral band can be written as

$$SNR_j = \frac{\boldsymbol{v}_j^T \boldsymbol{C}_H \boldsymbol{v}_j}{\boldsymbol{v}_j^T \boldsymbol{C}_N \boldsymbol{v}_j} - 1, \; j = 1, \dots, P \tag{10}$$

where $\boldsymbol{v}_j, j = \{1, \dots, P\}$ are orthonormal vectors of matrix $\boldsymbol{V}$.

## 3. Comparison of PCA and MNF band reduction methods with target detection algorithm

We use Adaptive Coherence Estimator (ACE) [10] target detection method alone and with PCA and then MNF to compare band reduction methods in terms of processing time and detection accuracy.

ACE is a target detection method that can be used in cases where background statistical parameters are not known. This method is derived from Generalized Likelihood Ratio (GLR) approach. Based on the assumption that the background covariance matrix is known, target detection criterion $D$ is calculated for each $\boldsymbol{h}_i$ pixel vector as follows:

$$D(\boldsymbol{h}_i) = \frac{\left(\boldsymbol{g}^T \boldsymbol{C}_H{}^{-1} \boldsymbol{h}_i\right)^2}{(\boldsymbol{g}^T \boldsymbol{C}_H{}^{-1} \boldsymbol{g})(\boldsymbol{h}_i{}^T \boldsymbol{C}_H{}^{-1} \boldsymbol{h}_i)} \tag{11}$$

where $\boldsymbol{g}$ is the target spectrum. In equation (11), ACE algorithm estimates the detection statistics and obtains a separation between the target and the background.

For experimental studies, we use hyperspectral data set which was collected by HyMap sensor and supplied by Rochester Institute of Technology. Hyperspectral data set has 3-meter spatial resolution per pixel and 126 spectral bands. Also, data set includes spectral signature of red small carpet [2].

For the evaluation purpose, we use PCA in conjunction with ACE called PCA-ACE method and then MNF with ACE, named MNF-ACE method on hyperspectral data set with spectral signature of 3x3 meter red carpet.

Experimental tests are performed on a computer with the specifications of Intel Core i5 2450M 2.5 GHz processor and 4GB RAM. The higher the detection accuracy, the greater the detection performance is. The best detection result is given with detection accuracy of 1. Using band reduction improves detection performance.
The results for all methods are given in Tab. 1. As it can be seen in Tab. 1, accuracy and processing time are the best for ACE target detection algorithm with MNF band reduction method.

Table 1. Comparison of band reduction methods for effect on target detection algorithm in terms of processing time and detection accuracy.

| Method | Processing Time (second) | Detection Accuracy |
|---|---|---|
| ACE | 6.65 | 0.6892 |
| PCA-ACE | 2.55 | 0.6927 |
| MNF-ACE | 2.40 | 0.8164 |

In order to demonstrate the effect of band reduction methods, PCA and MNF, target pixel spectrum and results of target detection are shown in Fig. 4. The spectrum in Fig. 4 (a) is the target signature, which is also detected by ACE without band reduction. In Fig. 4 (b), target spectrum which is detected by ACE with PCA band reduction method is shown. In this method resulting number of bands is 90. Other spectrum with 35 bands given in Fig. 4 (c) is detected by ACE with MNF band reduction method. MNF reduction results in the least number of bands used in target detection with the highest detection accuracy.

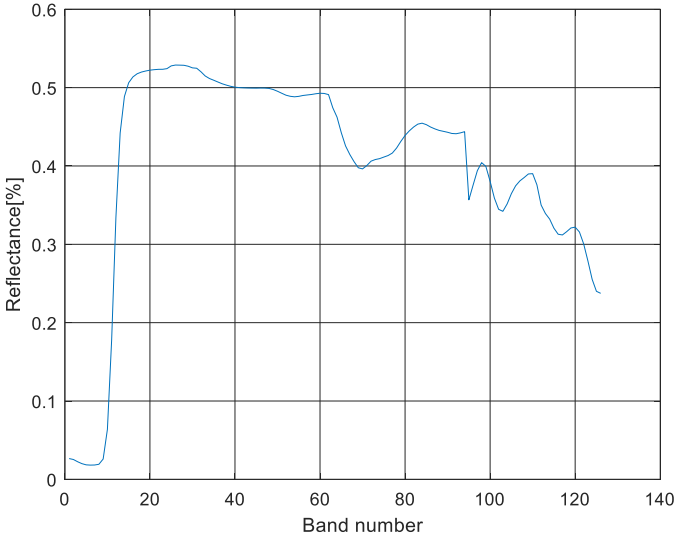
Reflectance[%]
Band number
0
0.1
0.2
0.3
0.4
0.5
0.6
0
20
40
60
80
100
120
140

(a)

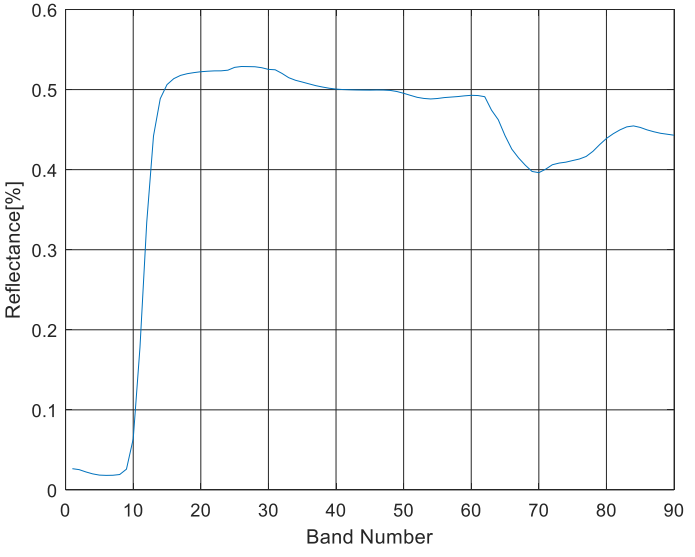
Reflectance[%]
Band Number
0
0.1
0.2
0.3
0.4
0.5
0.6
0
10
20
30
40
50
60
70
80
90

(b)

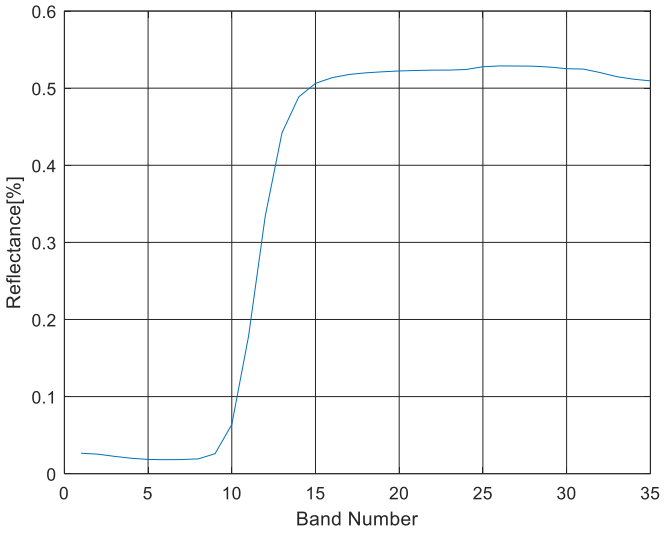


(c)

FIGURE 4. Comparison of detected target spectra (a) Original target signature which is detected by ACE without any band reduction application, (b) detected target spectrum by ACE with PCA band reduction, (c) detected target spectrum by ACE with MNF band reduction

## 4. CONCLUSION

In this study, a comparative framework was developed for band reduction approaches for target detection in hyperspectral images. We specifically investigated PCA and MNF band reduction algorithms when used with ACE algorithm for target detection in hyperspectral images. ACE alone gives the worst results in terms of processing time and detection accuracy when used without band reduction. Conversely, the results demonstrate that band reduction increases target detection performance since noisy bands are eliminated. Particularly, MNF band reduction algorithm with ACE leads to better detection accuracy and processing time than PCA with ACE. It is possible to extent future works with other target detection and band reduction methods, more targets with spectral signatures and hyperspectral images.

## References

[1] Marwaha, R. and Kumar, A., Target Detection Algorithm for Airborne Thermal Hyperspectral Data, ISPRS Technical Commission VIII Symposium, Volume XL-8, 2014.

[2] RIT (Rochester Institute of Technology) 2006, Chooke City Hyperspectral Data Set http://dirsapps.cis.rit.edu/blindtest/download. Last access date: 24.07.2019.

[3] Rodarmel, C. and Shan, J., Principal Component Analysis for Hyperspectral Image Classification, Surveying and Land Information Science, 62(2), (2002), 115-122.

[4] Gonzalez, R. and Woods, R., Digital Image Processing, Reading, Massachusetts, Addison-Wesley Publishing Company. pp.148-56, 1993.

[5] Mallapragada, S., Wong, M. and Hung, C., Dimensionality Reduction of Hyperspectral Images for Classification, Ninth International Conference on Information, Tokyo, Japan, 2018.

[6] Vaiphasa, C., Consideration of Smoothing Techniques for Hyperspectral Remote Sensing, *ISPRS Journal of Photogrammetry and Remote Sensing,* 60, Elsevier, New York, (2006), 91-99.

[7] ITT Visual Information Solutions, (ENVI User's Guide), 2009.

[8] Jin, X., Paswaters, S. and Cline, H., A Comparative Study of Target Detection Algorithms for Hyperspectral Imagery, Proc. SPIE 7334, Algorithms and Technologies for Multispectral, Hyperspectral, and Ultraspectral Imagery XV, 73341W , 2009.

[9] Gordon, C., A Generalization of the Maximum Noise Fraction Transform, *IEEE Trans. Geosci. Remote Sens.,* 38, (2000), 608–610.

[10] Manolakis, D. and Shaw, G., Detection Algorithms for Hyperspectral İmaging Applications, Signal Processing, 2002.

*Current Address:* MURAT ŞİMŞEK: Ankara University, Electrical and Electronics Eng. Dept., Gölbaşı, Ankara, TURKEY
*E-mail:* muratsimsek003@gmail.com
*ORCID:* https://orcid.org/0000-0002-8648-3693

*Current Address:* HAKKI ALPARSLAN ILGIN: Ankara University, Electrical and Electronics Eng. Dept., Gölbaşı, Ankara, TURKEY
*E-mail:* ilgin@eng.ankara.edu.tr
ORCID: https://orcid.org/0000-0003-0112-4833

Commun.Fac.Sci.Univ.Ank.Series A2-A3
Volume 62, Number 1, Pages 63-70 (2020)
DOI: 10.33769/aupse.660187
ISSN 1303-6009 E-ISSN 2618-6462
http://communications.science.ankara.edu.tr/index.php?series=A2A3

# RF ANTENNA DESIGN FOR BUTTON-TYPE BEAM POSITION MONITORS USING BIO-INSPIRED OPTIMIZATION METHODS

Ayhan AYDIN and Erkan BOSTANCI

ABSTRACT. Accelerator based facilities are in a leading position for crafting many scientific and technical innovations for a wide range of application from aviation to medicine. Beam Position Monitors (BPMs) are critical diagnostics tools for such facilities. This study presents bio-inspired methods known as Particle Swarm Optimization and Evolutionary Algorithms in order to design RF antennas for button-type BPMs. Our results show that the antenna parameters obtained using this multiple objective approaches present suitable SNR and linearity values for signal processing. It is found that using an antenna radius of 5.5 mm and beam-pipe radius of 17.5 mm, we can obtain SNR values around 40 dB which can be electronically processed.

## 1. INTRODUCTION

Although the installation and operation costs of accelerator based facilities require huge investments, they play a major role in the development of science and technology. Particle beams produced in such facilities must be continuously diagnosed and be subject to correction processes in order to provide protection from any radiation damage. Beam Position Monitors (BPM) are one of the most important diagnostics tools to diagnose entire system and they are used to determine position of beam inside the beam-pipe [1-3]. There are three important concerns in this process which can be listed as: (1) BPM antennas should provide adequate signal, i.e. signal-to-noise ratio (SNR) for signal processing, (2) beam position measurement should be done accurately and (3) the measurement system should be non-destructive to the beam. Considering these requirements, studies were carried out to determine the geometry of button-type BPM antennas using numerical and

Received by the editors: December 16, 2019; Accepted: March 02, 2020.
*Key word and phrases:* Multiple objective evolutionary algorithms, RF antenna design, beam position monitors.

analytical approaches [4]. In this study, we focused on optimizing the geometric properties of BPM antennas such as diameter, thickness and gap by using bio-inspired optimization algorithms such as Particle Swarm Optimization (PSO) and Evolutionary Algorithms (EA) [5-7].

## 2. BPM ANTENNA DESIGN

Different techniques can be used to determine of the beam position. However, these techniques can damage structure of the beam or they can be very expensive. Therefore, BPMs are widely used for all kind of accelerators due to low cost and robustness. The mechanical system of BPMs are generally designed as a cylindrical structure with 4 antennas placed on. Determination of the beam position is directly related to geometry of the BPM. This geometric design can affect many parameters such as accuracy, resolution, bandwidth, dynamic range, SNR *etc*. Therefore, design and production stages are key to achieve these requirements. In this study, optimization methods are applied on the following basic formulas to find geometric features of the BPMs for Turkish Accelerator and Radiation Laboratory in Ankara (TARLA) [8].

The signal power depends on the geometric parameters of BPM including beam-pipe radius, antenna diameter and thickness [9]. Once an adequate signal level is obtained, this signal can then be processed electronically by a front-end electronic system [10]. Despite the fact that the signal level can be increased by extending the antennas, it is known that using larger fitting elements makes it difficult to achieve an ultra-high vacuum level.

For this reason, we optimized antenna radius along beam-pipe radius and thickness for admissible values considering TARLA beam parameters such as the beam-pipe radius between 17.5 mm and 21 mm, average beam current of 1 mA and bunch repetition rate of 13 MHz.

In order to find optimal antenna radius $\boldsymbol{a}$ and beam-pipe radius $\boldsymbol{b}$ parameters, we used the following formula for finding signal power ($P_s$) and noise power ($P_n$) defined by Smith [2] as an objective function:

$$P_s = \frac{2\pi^2 a^4}{b^2 \beta^2 c^2} Z A_m^2 f_0^2 I_{avg}^2 \tag{2.1}$$

and

$$P_n = k_B T Z B \tag{2.2}$$

Then the SNR can be calculated as:

$$SNR = \frac{P_s}{P_n} \tag{2.3}$$

## 3. Parameter Optimization

Finding optimal design parameters for BPM is a numerically expensive problem. Considering the complexity of the power and signal calculations for a large number of candidate solutions, following a numerical or analytical optimization approaches may be a challenge. Furthermore, the classical approaches also tend to get stuck at local optimum.

The literature presents bio-inspired optimization methods such as PSO and EA [11-14] which are both stochastic computation techniques inspired by the flocking behavior of the birds and the basic law of survival of the fittest, respectively. Such optimization methods do not require prior knowledge about the solution, rather use a fitness function to choose among candidates that are promising to yield better solutions through a heuristic process.

In this paper, the design problem for the BPM was modeled using both approaches with two optimization goals as (1) to increase $P_s$, (2) decrease antenna radius, gap and thickness subject to three constraints as having (1) SNR larger than 30 dB (2) resolution smaller than 20 micrometer and (3) capacitance larger than 1 pF.

## 4. Results

Results show that the electron beam located anywhere in the beam-pipe (with radius 17.5 mm and antenna radius of 5.5 mm) can be measured linearly in the first 10 mm region of by using 11 mm diameter antennas as depicted in Fig.1.

Fig. 1a. and Fig. 1b. depict the extreme examples for the antenna size for 2.5 mm and 10 mm, respectively. It can be seen that the measurements can overlap for a short antenna (Fig. 1a), which means that there will be accuracy problems, *i.e.* linearity problems can be faced, in the measurement, whereas in case of using a long one (Fig. 1b.), more accurate readings can be achieved. The problem with using a

long antenna is that they are not always of practical use due to manufacturing process since antennas with a larger volume may counteract the vacuum permittivity constraints.

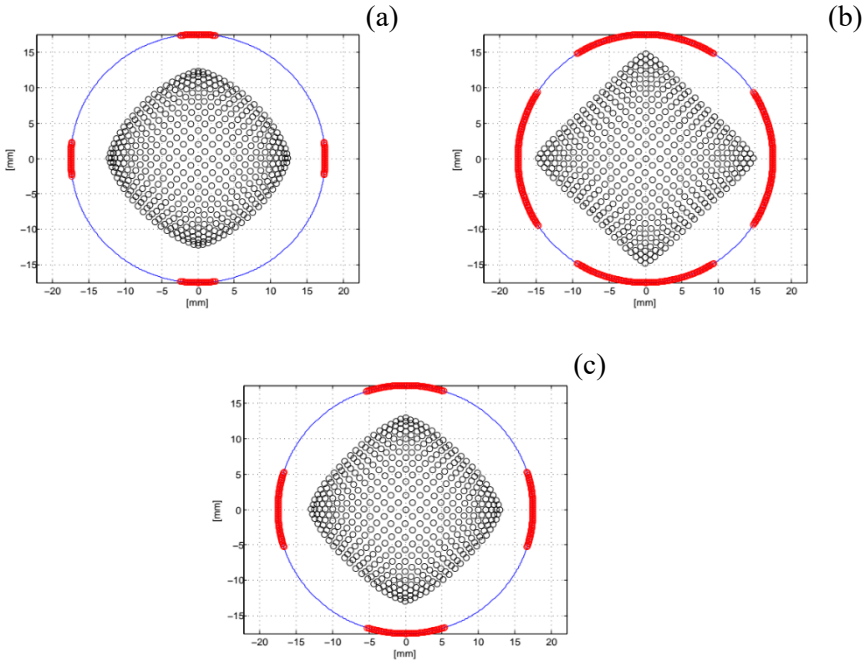


FIGURE 1. Linearity maps for the electron beam for varying antenna lengths (a) 2.5 mm (b) 10 mm (c) 5.5 mm.

The optimized length of 5.5 mm (Fig. 1c.) can achieve accurate measurement in 10 mm range of the beam-pipe. For the non-linear part (beyond 10 mm), mathematical interpolation methods such as curve fitting can be applied to determine beam position.

The beam position calculated in terms of voltages is depicted in Fig. 2 for small displacements from the beam-pipe center as described in [2].

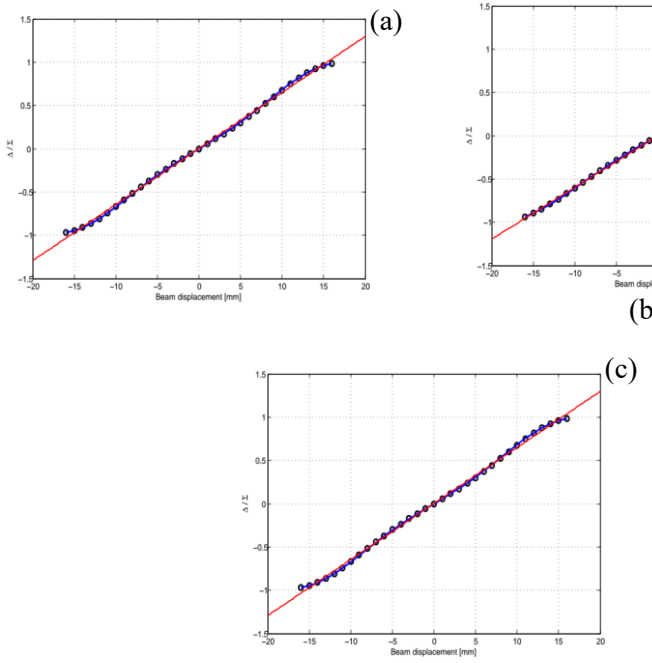


FIGURE 2. Sensitivities for the ***xy*** plane. Asterisks for ***x*** axis, line for ***y*** axis. Red line is added to compare linearity of the results. (a) 2.5 mm (b) 10 mm (c) 5.5 mm.

Here, it can be seen that the sensitivities are consistent for both axes on the ***xy*** plane. Difference over sum for the signals obtained from opposite antennas. It is clear that the sensitivity increases with the length of the antenna, the optimized length is given in Fig. 2c.

Fig. 3. shows the relation between SNR, beam-pipe radius and resolution for the solutions obtained using the bio-inspired approaches. It can be seen that as the SNR increases, BPM can achieve better resolution values.

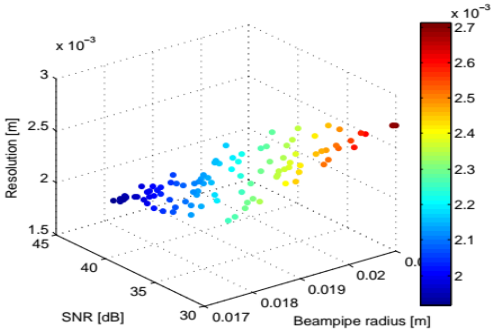


FIGURE 3. Relation between SNR, beampipe radius and resolution.

A comparison between EA and PSO is presented in Fig. 4. It can be seen that both approaches can find similar SNR values and both approaches can yield SNR values above 40 dB. These results are in an acceptable range for the isolation of the power signal from the noise signal.

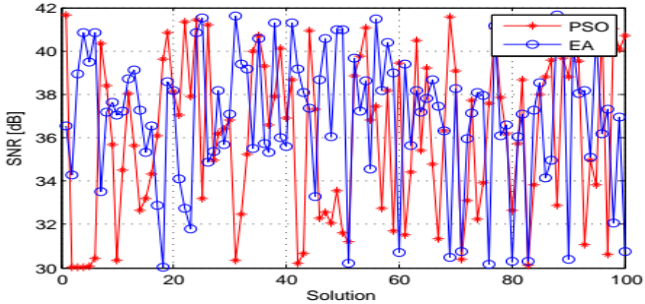


FIGURE 4. Comparison of EA and PSO.

Table 1. shows the capacitance and SNR values for the given antenna lengths. All capacitance and SNR values are in a range that is appropriate for signal processing.

**Table 1.** Relation between antenna length, capacitance and SNR

| Antenna Length (mm) | Capacitance (pF) | SNR (dB) |
|---|---|---|
| 2.5 | 1.22 | 13.957 |
| 5.5 | 2.55 | 30.001 |
| 10 | 4.55 | 39.720 |

The findings obtained here are for the button-type BPMs which are employed in the TARLA facility due to limited space available on the beam-pipe since other BPM types require larger space.

## 5. Conclusion

The findings for the infrared RF realm accelerators showed that the use of bio-inspired optimization methods, namely EA and PSO for antenna and BPM geometry design can yield more practical solutions than analytical and FEM methods. It is shown that parameters such as SNR and sensitivity are in a suitable range for signal processing techniques.

This approach can be used for all types of BPMs such as button, cavity and stripline as it offers a wide range of solutions while offering flexibility during design and production of BPMs.

**Acknowledgements.** The study is supported by TUBITAK 2219-International Postdoctoral Research Fellowship Program. The authors would also like to thank TARLA for the collaborative research support.

## References

[1] Shafer, Robert E., Beam position monitoring, *AIP conference proceedings*, (1992), 601–636.

[2] Smith, Stephen R., Beam position monitor engineering, *AIP conference proceedings*, (1997), 50–65.

[3] Forck, P., Liakin, D. and Kowina, P., Beam position monitors, CERN Accelerator School on Beam Diagnostics, (2009), 187–228.

[4] Nosych, A., Iriso, U. and Olle, J., Electrostatic finite-element code to study geometrical nonlinear effects of BPMs in 2D, *4th International Beam Instrumentation Conference (IBIC2015)*, Melbourne, Australia, (2015) 418-422

[5] Yiğit, S. S., Ar, Y. and Bostanci, G. E., Evolutionary approaches for weight optimization in collaborative filtering-based recommender systems, *Turkish Journal of Electrical Engineering & Computer Sciences*, (2019), 27.3, 2121-2136.

[6] Karim, A. M., Güzel, M. S., Tolun, M. R., Kaya, H. and Çelebi, F. V., A new generalized deep learning framework combining sparse auto encoder and Taguchi method for novel data classification and processing, *Mathematical Problems in Engineering*, (2018).

[7] Mohammed, S. N., Guzel, M. S. and Bostanci, E., Classification and Success Investigation of Biomedical Data Sets Using Supervised Machine Learning Models, *In*

*3rd International Symposium on Multidisciplinary Studies and Innovative Technologies (ISMSIT),* IEEE, (2019), 1-5.

[8] Aksoy, A., Karsli, O., Aydin, A., Kaya, C., Ketenoglu, B., Ketenoglu, D. and Yavas, O., Current status of Turkish accelerator and radiation laboratory in Ankara: the TARLA facility, *Canadian Journal of Physics,* 96(7), (2018), 837-842.

[9] Aydin, A., Bostanci, E. and Tanriover, Ozgur O., A Multiple Objective Evolutionary Algorithm Approach to Find Optimal Design Parameters for Beam Position Monitoring Systems, *International Journal of Modern Physics C*, (2019) doi: 10.1142/S0129183120500382

[10] Aydin, A. and Kasap, E., Design studies for the beam position monitor (BPM) front-end electronics of the Turkish accelerator and radiation laboratory in Ankara (TARLA). *Turkish Journal of Physics*, 41(3), (2017), 269-276.

[11] Eberhart, R. C. and Shi, Y., Comparison between genetic algorithms and particle swarm optimization, *International conference on evolutionary programming, (1998), 611–616.*

[12] Nebro, A. J., Durillo, J. J., Garcia-Nieto, J., Coello, C.A., Luna, F. and Alba, E., SMPSO: A new PSO-based metaheuristic for multi-objective optimization, *IEEE Symposium on Computational Intelligence in Multi-Criteria Decision-Making (MCDM)*, (2009), 66–73.

[13] Kollat, J. B. and Reed, P. M., Comparison of multi-objective evolutionary algorithms for long-term monitoring design, *World Water and Environmental Resources Congress, (2005).*

[14] Ketenoğlu, D., Bostanci, G. E., Aydin, A. and Ketenoğlu, B., A hard X-ray self-amplified spontaneous emission free-electron laser optimization using evolutionary algorithms for dedicated user applications, *Turkish Journal of Physics*, *43*(6), (2019), 551-555.

*Current Address:* Ayhan AYDIN: Ankara University, Computer Engineering Department, Ankara, TURKEY
*E-mail:* ayaydin@ankara.edu.tr
*ORCID:* https://orcid.org/0000-0001-7938-0509

*Current Address:* Erkan BOSTANCI: Ankara University, Computer Engineering Department, Ankara, TURKEY
*E-mail:* ebostanci@ankara.edu.tr
*ORCID:* https://orcid.org/0000-0001-8547-7569.

Commun.Fac.Sci.Univ.Ank.Series A2-A3
Volume 62, Number 1, Pages 71-78 (2020)
DOI: 10.33769/aupse.584380
ISSN 1303-6009 E-ISSN 2618-6462
http://communications.science.ankara.edu.tr/index.php?series=A2A3

# GENERATING TURKISH LYRICS WITH LONG SHORT TERM MEMORY

HAKAN ERTEN, MEHMET SERDAR GUZEL and ERKAN BOSTANCI

ABSTRACT. Long Short Term Memory (LSTM) has gained a serious achievement on sequential data which have been used generally videos, text and time-series. In this paper, we aim for generating lyrics with newly created "Turkish Lyrics" dataset. By this time, there have been studies for creating Turkish Lyrics with character-level. Unlike previous studies, we propose to Turkish Lyrics generator working with word-level instead on character-level. Also, for employing LSTM, we can't send the words as string and words must be vectorized. To vectorize, we tried two ways for encoding the words that are used in dataset and compared them. Firstly, we sample for generating one-hot encoding and then, secondly word-embedding way (Word2Vec). Observational results show us that word- level generation with word-embedding way gives more meaningful and realistic lyrics. Actually, there have not been good results enough to be used for a song because of Turkish Grammar. But, this study encourages authors to work on this field and we do believe that this study will initialize research on this area and lead researchers to contribute to this as well.

## 1. INTRODUCTION

Recurrent Neural Network (RNN) has appeared for solving the problems where sequential data will be used. It can be consecutive time or word or sentence. But, RNN is not an effective method of temporarily keeping long- term data and conventional RNN is hard to train [1]. Problems in RNN use have been solved with LSTM.

Received by the editors: June 29, 2019; Accepted: April 22, 2020.
*Key word and phrases:* LSTM, machine learning, one-hot encoding, word embedding, Turkish lyrics estimation.

Basically, LSTM has input, output, forget gates and a memory cell which can retain series of data. This cell controls the flow of information. LSTM is the state-of-the-art for many complex situations. The original formula of LSTM have been made many years ago [2] [3]. In this paper, we used architecture which is defined details in Colah et al.(2015) [4]. Figure 1 presents the design of LSTM.

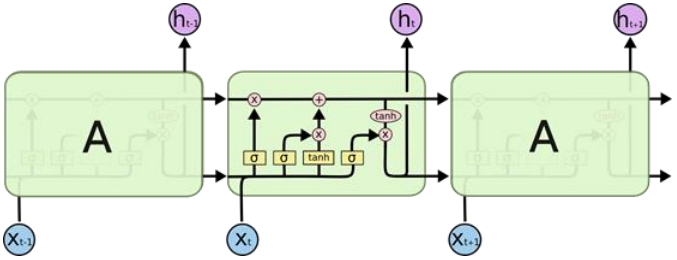


FIGURE 1. LSTM contains for interacting modules.

The model shared by [4], the following equations are identified as follows:

$$f_t = \sigma(W_f \cdot [h_t - 1, x_t] + b_f) \quad (1)$$

$$i_t = \sigma(W_i \cdot [h_t - 1, x_t] + b_i) \quad (2)$$

$$\overline{C}_t = tanh(W_C \cdot [h_t - 1, x_t] + b_C) \quad (3)$$

$$C_t = f_t * C_{t-1} + i_t * \overline{C}_t \quad (4)$$

$$o_t = \sigma(W_o \cdot [h_t - 1, x_t] + b_t) \quad (5)$$

$$h_t = o_t * tanh(C_t) \quad (6)$$

Equivalents of characters are defined below; $t$ : timestep, $x_t$ : input vector at timestep $t$, $h_t$ : hidden state, $W$ : weight matrix of associated gate, $z$ : a vector from concatenation of $x_t$ and $h_{t-1}$, $b$ : bias term, $f_t$ : forget gate, $i_t$ : input gate, $o_t$ : output gate, $C_t$ : memory cell state, $\overline{C}_t$ : candidate state value which will be regulated with $i_t$, * : the element-wise product of vectors at each side, $\sigma$ : sigmoid function, *tanh* : hyperbolic tangent function.

Our work, on the other hand, provides the first Turkish Lyrics generation with word-level and using a newly created dataset. On websites, there are some works about this topic. However, there are not any word-level works with Turkish Lyrics. Compared with character-level, because of keeping words in integrity on word-level

generation, there is no unclear word in results. This is the biggest advantage of word-level usage. Besides generation, the vectorization methods have been compared (one-hot encoding and word2vec). Our experimental evaluations show that using word-level generation with word2vec embedding deduce more meaningful words than one-hot encoding for a Turkish song phrase.

## 2. Related Works

Machine learning gather lots of attention from the researchers and is applied into different research fields [5,6]. Text generation is one of the most popular topic for using RNN. In one of the recent works, Sutskever et al. [7] presented an strength of RNN. In this character-level work, language model is originated. In 2013, the same work (originating language model) has been implemented with LSTM and originated better language model. Graves et al. [8]

Generating lyrics has been analyzed in current works. There are several works in various languages and types of music. Potash et al. [9] proposes not just generating rap lyrics, also to create a structure. In this work, authors corpus with line-by-line. They predict the next line in already existing lines. Malmi et al. [10] presents a tool which generates online rap lyrics (deepbeat.org), offers an information-retrieval approach, demonstrates the rhyme density and uses line-by-line prediction. There are also other websites which create a song with your choices.

## 3. Methodology

### 3.1 Datasets

The general Looking for a inviolate Turkish lyrics for this study, we acquired a good col- lection of lyrics website 1. This corpus has also been used in a blog [11], but for an only singer's songs (Sezen Aksu). Composing a corpus, We decided to join the songs of singers singing the same style. The all set contained 932 song lyrics in txt format, as well as basic meta-data including only the lyrics without any other data. In order to use only words, all the punctuation marks and spaces have been erased from the corpus. Hence, we didn't want to punctuation marks spaces to be perceived as a word and desired to employ only Turkish alphabet characters. Since the two words in the Turkish words can have different meanings, we checked the spelling of all words one by one (Totally 85662 words). In order to prepare for training, there are several other processes. Firstly, if all the words in the corpus had been utilized,

a layer of tens of thousands of dimensions would have been used. To keep away from this large numbers, we decided to filter uncommon words (frequency = 10). If a word is less than 10 times in the corpus, this one is ignored. After the ignored words have been removed, all the remaining words have been written in a dictionary file. Secondly, since words can't be applied as string, All the words in dictionary have been needed to put into bits and vectorized. We split the dataset 98 for training and 2 for testing.

### 3.2 Wordembeddings (Word2vec)

Word embedding is one of the most favorite model of vectorization for text files. This model can find structure of a word, relation and similarities with other words. Word embedding is a vector representation of words. Word2Vec is a style which learns word embedding using shallow neural network. Word2vec is one of the most popular methods in recent years. Word2vec can be obtained with two methods: Skip Gram and Common Bag of Words (CBOW).

In this paper, firstly Keras Embedding Layer which is initialized with random weights have been used. In training, all the weights will be updated and will learn an embedding for all words. In our model, we have defined an embedding layer with our size of words and a vector space of 1024 dimensions in which words will be embedded. Some relational sequences have been obtained.

### 3.3 One-hot encoding

As said above, words cannot be used as string. One-hot encoding which is binary vector array is another way of model that can represent each integer value. It uses a simple binary vector. Firstly, the number equivalents of the letters are kept. Then, all words are expressed according to these equivalents. In this model, there are not any relation between words. Only the integer values of words can be used. Because of that, Generating lyrics with using this model, any relational results haven't been taken.

## 4. Model and Experiment

### 4.1 Model

As expressed, previous works show the power of LSTM to model language. In our paper, using word embedding, after embedding layer Keras Bidirectional LSTM layer which has 128 dimensions and dense layer with the size of words have been

used. Dense layer connected to a single softmax output layer. To prevent overfitting, dropout function have been used. We employed sparse categorical cross entropy as loss function and Adam function for optimizer. When using one-hot encoding, embedding layer have not been used predictably and as loss function employed categorical cross entropy. As you see, there are two differences between in two models.

```
>>>Sentence[0]:
['onlar' , 'biraz' , 'terkedilmiş' , 'biraz' , 'küskün']
>>>next_Word[0]:
['çocuktular']
>>>Sentence[1]:
["'biraz' , 'terkedilmiş' , 'biraz' , 'küskün' , 'çocuktular']
>>>next_Word[1]:
['sanki']
```

FIGURE 2. Sequence and next word examples.

## 4.2 Training the network architecture

For implementation, Python implementation of an LSTM from Enrique a2 have been used. First of all, the words of all the dataset have been splitted. 85662 words in text and 13539 unique words have been found. Then, to keep away from this large dimensionality, we calculated the frequency of the words and filtered uncommon words (frequency = 5). In next step, Sequences have been created and filtered. If a sentence contains an ignored Word, this sentence will not be used for training. After that, Sequences have been shuffled and splitted training set. (Training sequence number: 2963 and test seq. number: 61) After these steps, Model have been implemented and started training to learn weights. In training, our model tried to predict the next word at the end of the sentence. Our sentence consists of 10 words and the next word is the target word. The sentence and the target word compose the sequence. Our model works are given as follow:

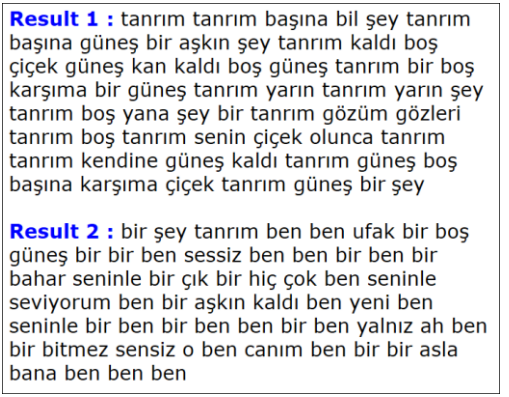


FIGURE 3. Word2vec results.

## 5. EXPERIMENTAL EVALUATION

### 5.1 Implementation details

For Word embedding and one-hot encoding architectures, we have trained the models for 100 epochs with a learning rate 0.01 and batch size 32. Mostly, after nearly 40 iterations, Good results have been obtained. The result was a 60-word lyrics. The Model is trained on a 12 GB NVIDIA TitanX GPU based laptop computer.

### 5.2 Results and discussion

In this section, we firstly present the word embedding result. Sample Lyrics is given in Figure 3. Secondly, one-hot encoding results are given in Figure 4.

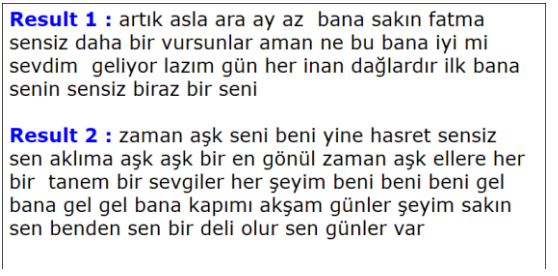


FIGURE 4. One-hot encoding results.

As a result, 85662 words have been trained but only 1052 of them used for estimation. We could not use thousands of words because of appendixes. Because Turkish is an agglutinative language. Because of that, some sentences which is created are not steady. Also, the meanings of two words of the same writing can be separated. This event can prevent the sentences from connecting the words properly. Dilemmas are frequently used in Turkish. Because of that, number of dilemmas are more than normal words. In most of the sentences generated due to the use of dilemmas too much, dilemmas took place almost nearly all the words.

## 6. Conclusion

In this paper, we collected a new Turkish Lyrics dataset. The dataset is opening up interesting directions to explore. In order to set the benchmarks in this dataset, we experimented a Turkish word-level lyrics generator. We also introduce vectorization methods (Word2vec and one-hot encoding). The experimental results indicates that the generation of lyrics with Turkish songs may be quite difficult because of the Turkish Grammar and sentence structure. Maybe, line-by-line generation can give better results for a song. Upon the publication of the paper, all the dataset will be made available to public.

## References

[1] Crash Course in Recurrent Neural Networks for Deep Learning, https://machinelearningmastery.com/ crash-course-recurrent-neural-networks-deep-learning/, accessed: 2019-06-15, 2010. 2

[2] Hochreiter, S., Schmidhuber, J., Long Short Term Memory, Technical Report FKI-207-95, URL http://citeseerx.ist.psu.edu/viewdoc/ similar? doi=10.1.1.51.3117&type =ab.2.

[3] Hochreiter, S., Schmidhuber, J., Long Short Term Memory, Neural Compu- tation, 9(8):17351780,November 1997. ISSN 0899-7667. doi: 10.1162/neco URL http://www.bioinf.jku.at/publications/older/2604.pdf. 2

[4] Understanding LSTM Networks, https://colah.github.io/posts/ 2015-08-Understanding-LSTMs/, accessed: 2019-06-17, 2015. 2

[5] Karim, A. M., Güzel, M. S., Tolun, M. R., Kaya, H., Çelebi, F. V., A new generalized deep learning framework combining sparse autoencoder and taguchi method for novel data classification and processing mathematical problems in engineering, Article ID 3145947, (2018), 13 pages.

[6] Karim, A. M., Güzel, M. S., Tolun, M. R., Kaya, H., Çelebi, F. V. A new framework using deep auto-encoder and energy spectral density for medical waveform data classification and processing, *Biocybernetics and Biomedical Engineering*, 39 (2019), 148–159.

[7] Sutskever, I., Martens, J., Hinton, G., Generating Text with Recurrent Neural Networks, *in: Proceedings of the 28th International Conference on Machine Learning, ICML*, (11 March 2011), 1017–1024,
[8] Graves, A., Mohamed, A.R., Hinton, G., Speech recognition with deep recur- rent neural networks, *in: IEEE international conference on acoustics, speech and signal processing, IEEE*, (March 2013), 6645–6649.
[9] Potash, P., Romanov, A., Rumshisky, A., Ghostwriter: Using an lstm for automatic rap lyric generation, *in: Proceedings of the 2015 Conference on Empirical Methods in Natural Language Processing*, (March 2015), 1919–1924.
[10] Malmi, E., Takala, P., Toivonen, H., Raiko, T., Gionis, A., DopeLearning: A Computational Approach to Rap Lyrics Generation, *in: Proceedings of the 22nd ACM SIGKDD International Conference on Knowledge Discovery and Data Mining, ACM*, (March 2016), 195–204.
[11] "Sezen aksu sarkisi yazan yapay zeka diyorum", 15/05/2019. https://medium.com/@tuncerergin/ sezen-aksu-sarkisi-yazan-yapay-zeka-diyorum-cd327001b7c4, Access date: 2019-05-31, 2019.

*Current Address:* Hakan ERTEN: Ankara University, Department of Computer Engineering, Ankara TURKEY
*E-mail:* hakanerten09@gmail.com
*ORCID:* http://orcid.org/0000-0002-4208-1537

Current Address: Mehmet Serdar GUZEL (Corresponding author): Ankara University, Department of Computer Engineering, Ankara TURKEY
E-mail: mguzel@ankara.edu.tr
ORCID: http://orcid.org/0000-0002-3408-0083

Current Address: Erkan BOSTANCI: Ankara University, Department of Computer Engineering, Ankara TURKEY
E-mail: ebostanci@ankara.edu.tr
ORCID: http://orcid.org/0000-0001-8547-7569

Commun.Fac.Sci.Univ.Ank.Series A2-A3
Volume 62, Number 1, Pages 79-99 (2020)
DOI: 10.33769/aupse.740416
ISSN 1303-6009 E-ISSN 2618-6462
http://communications.science.ankara.edu.tr/index.php?series=A2A3

# STUDY OF TRANSPORTATION PROBLEM OF IRON AND STEEL INDUSTRY IN TURKEY BASED ON LINEAR PROGRAMMING, VAM AND MODI METHODS

Rehile ASKERBEYLİ

ABSTRACT. The subject of this study is the investigation of the minimization of the total transportation costs for finished product produced by Alter Iron and Steel Industry Company in its own production facilities in Karabuk. Firstly, the current situation in the Iron and Steel Industry in the world and Turkey are briefly discussed. In the second stage, the distribution to the demand point from the factory operating in the Iron and Steel Sector is considered as the basic problem. The demand points were determined as geographical regions. We have two targets: the total cost to be minimized and the total amount of goods to be sent from supply center to the demand centers to be equal to the total demand or supply amount. The optimum solution of the transportation model were solved both the traditional transportation model methods such as Vogels Approximation Method (VAM), Modified Distribution (MODI) method and the linear programming method. The optimal solution for last model was found using the R /SIMPLEX package program. Obtained results by different approaches are discussed. Critical aspect of this problem is to use the single source transportation model, where all demand amounts are met from a single production center..

## 1. INTRODUCTION

### 1a. Iron and Steel Industry in the World

The iron and steel sector is one of the main sectors of the heavy industry sector, which gives majority contributes to the development of the national economy. Conventionally, the economic impact of an industry is measured by its contribution to GDP (Gross Domestic Product), i.e. gross value added from the industry - the

Received by the editors: May 20, 2020; Accepted: June 01, 2020.
*Key word and phrases:* Iron and steel industry, linear programming, simplex method, transportation model, single source product distribution.

difference between the value of output and intermediate inputs. Another important indicator is the number of people working in the industry. These indicators help to describe the direct impact. The steel industry has a gross value added of US$500 billion, which is 0.7% of global GDP and employs just over 6 million people.

Steel is a key input in the work of many other industrial sectors, which produce items essential to the functioning of the wider economy-including hand tools and complex factory machinery; lorries, trains, and aircraft; and countless items used by individuals in their everyday lives, from cutlery to cars and other. It also creates opportunities for innovative solutions in other sectors and is indispensable in research and development projects around the world. Given such a wide range of steel applications and its functions, it is not an easy and simple task to give a fair assessment of the economic impact of the steel industry through numbers. This is why in 2019 the World Steel Association commissioned Oxford Economics to evaluate our industry's impact on a global scale [1].

According to this report [1] the steel industry is active in all parts of the world, transforming iron ore into a range of products that are sold for a total annual value of US $2.5 trillion. The industry employed more than six million people around the world in 2017, and the "added value" of its production processes totaled almost US $500 billion. This figure comprises the industry's employment costs, capital costs, and net profits, and is the standard way of allocating global or national output GDP between sectors.

As shown in the report [1], we also find that for every two jobs in the steel sector, 13 more jobs are supported throughout its supply chain-meaning that, in total, some 40 million people work within the steel industry's global supply chain, generating over US $1.2 trillion of added value. This economic activity extends across multiple sectors and countries, far beyond the major steel-producing locations. The world steel study differentiates itself from the existing national studies by taking a global approach. Trade and the scope of impact is not limited to national borders and takes into consideration global supply chains and steel using sectors. It underlines the complexity of the role which the steel industry plays in the global economy. The overall impact of the steel industry is US$2.9 trillion value added, and 96 million jobs globally [1].

In Fig. 1, we can see how the growth in the world iron and steel sector is realized with the production amount; crude steel production in the world has achieved rapid

growth due to steady growth and increasing demand in the world economy from 2005 until to 2008-2009 global crisis. World crude steel production, which was 1.15

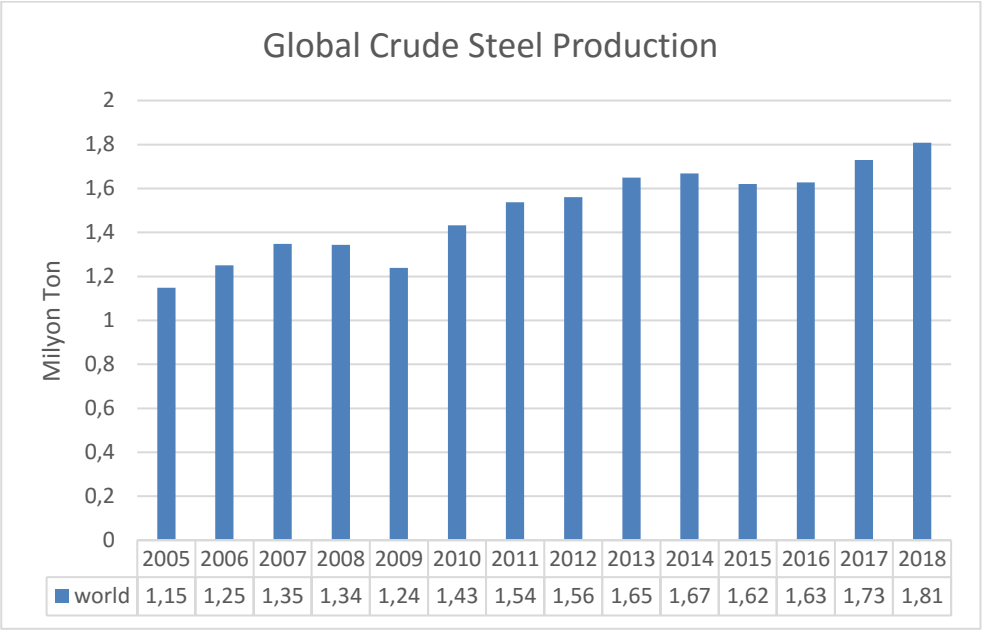


FIGURE 1. Crude (Liquid) Steel Production in the World (Billion Ton) World Steel

million tons in 2005, reached 1.24 million tons in 2009, but in 2007, production decreased significantly compared to approximately 1.35 million tons. Due to the decreasing demand as a result of the global economic crisis, the world steel production, which decreased in 2008 and 2009, started to increase again in 2010 and the production reached 1.43 million tons. Due to the lack of demand in 2015, production decreased by 0.05 million tons again compared to the previous year and reached 1.80 million tons in 2018.

According to World Steel Association (world steel) data on February 2020, world crude steel production increased by 2.8% compared to the same month of the previous year, reaching 143 million tons and 1% increase in the first two months of the year, at 294 million tons. As of the first two months of the year, China's crude

steel production increased by 3.1% compared to the same period of 2019 achieved to 155 million tons, while India's second-place crude steel production decreased by 0.8% to 18.9 million tons. Among the top 15 countries producing the most crude steel, Iran was the country with the highest production increase with a rate of 40.5% in January-February period, Turkey increase of the production by 12.7% took second place. In the first 2 months, Germany's production continued to decline and decreased by 10.9% to 6 million tons.

## 1b. Iron and Steel Industry in Turkey

Turkish steel industry was founded in the 1930s in order to meet the steel needs of the defense industry. Steel production started with the installation of two sixteen-ton Siemens-Martin mills in Kırıkkale. With the establishment of this sector, the country's economy started to develop and industrialization gave its first shoots. The first investments related to the steel sector were made in the 1930s within the scope of the 1st and 2nd industrial plans and the industry developed for a long time in the monopoly of the public sector, with integrated facilities predominantly [2].

Crude steel production in the world and in our country is carried out in Integrated Iron Steel (IIS) facilities using iron ore and in Induction and Electric Arc Furnace (EAF) facilities that produce scrap. When we view the production infrastructure of the sector, we see that a production infrastructure mainly based on scrap. As of 2018, there are 3 Integrated Iron and Steel plants producing iron ore and 31 Induction and Electric Arc Furnace plants producing scrap. As of 2018, 39.4 million tons of 51.8 million tons of crude steel capacity belong to facilities producing scrap and 12.4 million tons of iron ore. In addition, the sector has 22 Researcher centers and 3 Design Centers along with other metal sectors [3].

Karabuk Iron and Steel Manufacturer (Kardemir) is the first integrated steel mill which producing long products in Turkey. In the early years of the republic, KARDEMİR, the first integrated iron and steel plant, was established in Sümerbank as a public economic enterprise due to the lack of resources of the private sector. Then, the second integrated facility of the country Eregli Iron and Steel Factories (ERDEMİR) started production in 1965. The main purpose of this Manufacturer is to provide the demand of flat products. In order to provide the demand for the long and semi-finished products the third integrated facility in Turkey, Iskenderun Iron and Steel Factories (ISDEMIR) was opened for business. According to statistic dates for 2020 year, 32 facilities are operating in the sector which divided into four regions. There are 10 companies which operate in the Iskenderun region, 9

companies take place in the Marmara region, 8 companies are in the Izmir region and 5 companies are in the Black Sea (2020 year).

Steel production capacities are following for regions: 16.7 million tons for Iskenderun region, 15.2 million tons for Marmara region, 11.3 million tons for Izmir region and 8.3 million tons for Black Sea region. The crude steel production capacity for the Iron and Steel Factories in Turkey following: for 11 Factories 2 million tons and above, the capacity of 7 Factories are 1 - 2 million tons and 6 companies of them have a capacity from 500 thousands to 1 million tons, the capacity 8 companies between 50 and 500 thousand tons.

On Table 1 and 2, we can see the Turkey's Industry and Productivity directorate Sector Reports by years (2013-2020).

TABLE 1. *Turkey's Steel Production (Million Tons)*

| | **2013** | **2014** | **2015** | **2016** | **2017** | **2018** |
|---|---|---|---|---|---|---|
| **Billet** | 26,294 | 24,612 | 23,231 | 23,015 | 25,839 | 24,669 |
| **Slab** | 8,360 | 9,423 | 8,286 | 10,148 | 11,685 | 12,643 |
| **TOTAL** | **34,654** | **34,035** | **31,517** | **33,163** | **37,524** | **37,312** |
| **EAF** | 24,723 | 23,752 | 20,482 | 21,846 | 25,963 | 25,799 |
| **IIS** | 9,931 | 10,283 | 11,035 | 11,317 | 11,561 | 11,513 |
| **TOTAL** | **34,654** | **34,035** | **31,517** | **33,163** | **37,524** | **37,312** |

TABLE 2. Turkey's Steel Production (Million Tons)

| | **2019 2months** | **2020 2months** | %difference2020-2019 |
|---|---|---|---|
| **Billet** | 3.176 | 3.725 | 17.3 |
| **Slab** | 2.027 | 2.139 | 5.5 |
| **TOTAL** | **5.203** | **5.865** | **12.7** |
| **EAF** | 3.333 | 3.932 | 18 |
| **IIS** | 1.870 | 1.933 | 3.4 |

January-February period of 2020, Turkey's total crude steel production increased by 12.7%, rise from 5.2 million tons to 5.9 million tons in the same period of 2019. In the first two months of this year, facilities with electric arc furnaces increased by 18% achieved to 3.9 million tons; integrated plants produced 1.9 million tons of crude steel, increasing by 3.4%. January-February period Turkey's billet production 17.3% increase over last year from 3.2 million tons to 3.7 million tons in the same period. The slab production was increasing by 5.5% achieved value from 2 million tons to 2.1 million tons [4]. However, now due to the contracting effect of the coronavirus on the international market, has caused our exports to decline by 8.2% in February. On the other hand, our production was only able to increase by 8.2% due to the increase in imports by 31.2% despite the 68.2% increase in consumption. Thus, in the first 2 months of the year, imports increased by 40.4%, while the increase in domestic steel production was 12.7%.

## 2. Problem description

The subject of this paper is the investigation of the minimization of the total transportation costs for finished product produced by Alter Iron and Steel Industry Company in its own production facilities in Karabuk. Thus, production planning involves decisions such as distribution of the production mix between several plants according to their individual capacity, the need for totally external storage, and management of inventory levels for each plant.

Critical aspect of this problem is using the single source transportation model, in which all demand amounts are met from a single production center [5]. The problem of minimizing the total transportation cost is generally considered as a single source linear transportation model in the literature. The single-source transportation problem was developed in [6-8]. In this study, one-year numerical data of the production amount and unit transportation costs of each product of 2018 year for the six types of products produced by the company were used. The traditional transportation model methods such as VAM (Vogels Approximation Method) [9], MODI (Modified Distribution methods) [10] and Simplex methods [11-14] were used to solve the problem.

The model includes a total of 6 products and 6 demand centers (provinces). As one can see from table1, we have 6 products and 6 demand centers (provinces). In other words, all demand amount are met from a single supply center. In our model, the products are produced in the Organized Industrial Zone of Karabuk and distribute

products to six cities in total, namely Kocaeli, Istanbul, Ankara, Izmir, Samsun and Karabuk. The solution of the transportation model can be solved both the traditional transportation model methods as VAM, MODI and with the help of the linear programming model. Data input, transportation table and mathematical form of the problem are as follows:

TABLE 3. Transportation Model

| products | Kocaeli | İstanbul | Ankara | Izmir | Samsun | Karabuk | supply amount |
|---|---|---|---|---|---|---|---|
| Steel Billet Products-1 | 51 $X_{11}$ | 65 $X_{12}$ | 43 $X_{13}$ | 85 $X_{14}$ | 70 $X_{15}$ | 17 $X_{16}$ | 17440 |
| Steel Billet Products-2 | 51 $X_{21}$ | 65 $X_{22}$ | 43 $X_{23}$ | 85 $X_{24}$ | 70 $X_{25}$ | 17 $X_{26}$ | 29057 |
| Steel Billet Products-3 | 51 $X_{31}$ | 65 $X_{32}$ | 43 $X_{33}$ | 85 $X_{34}$ | 70 $X_{35}$ | 17 $X_{36}$ | 21904 |
| Rebar Products-1 | 41 $X_{41}$ | 55 $X_{42}$ | 43 $X_{43}$ | 75 $X_{44}$ | 60 $X_{45}$ | 7 $X_{46}$ | 6608 |
| Rebar Products-2 | 41 $X_{51}$ | 55 $X_{52}$ | 43 $X_{53}$ | 75 $X_{54}$ | 60 $X_{55}$ | 8000 | 8000 |
| Rebar Products-3 | 41 $X_{61}$ | 55 $X_{62}$ | 43 $X_{63}$ | 75 $X_{64}$ | 60 $X_{65}$ | 7 $X_{66}$ | 5500 |
| demand amount | 24443 | 10958 | 9000 | 6000 | 4000 | 34108 | 88509 |

Our aim is fined the optimal solution of the objective Function which determined as:

$$Z_{min} = \sum_{i=1}^{6} \sum_{j=1}^{6} C_{ij} X_{ij} \qquad (i - product)\ ,\ (j - demand\ zone) \tag{1}$$

Here the variable $X_{ij}$ is the i-product amount from producton region to the j-transshipment point. $C_{ij}$- the unit transportation cost of the i- product from producton region to the j- transshipment point. So,

$$\begin{aligned} Z_{min} = {} & 51 * X_{11} + 65 * X_{12} + 43 * X_{13} + 85 * X_{14} + 70 * X_{15} + 17 * X_{16} + 51 * \\ & X_{21} + 65 * X_{22} + 43 * X_{23} + 85 * X_{24} + 70 * X_{25} + 17 * X_{26} + 51 * X_{31} + 65 * \\ & X_{32} + 43 * X_{33} + 85 * X_{34} + 70 * X_{35} + 17 * X_{36} + 41 * X_{41} + 55 * X_{42} + 33 * \\ & X_{43} + 75 * X_{44} + 60 * X_{45} + 7 * X_{46} + 41 * X_{51} + 55 * X_{52} + 33 * X_{53} + 75 * \\ & X_{54} + 60 * X_{55} + 7 * X_{56} + 41 * X_{61} + 55 * X_{62} + 33 * X_{63} + 75 * X_{64} + 60 * \\ & X_{65} + 7 * X_{66} \end{aligned} \tag{2}$$

Constraints set consist of three parts: supply, demand and the condition of being nonnegative.
Constraints set of supply:

$$\sum_{j=1}^{6} X_{ij} \leq a_i \qquad (i - product) \tag{3}$$

Here $a_i$ is the supply amount of i-product .

$$X_{11} + X_{12} + X_{13} + X_{14} + X_{15} + X_{16} \leq 17443$$
$$X_{21} + X_{22} + X_{23} + X_{24} + X_{25} + X_{26} \leq 29057$$
$$X_{31} + X_{32} + X_{33} + X_{34} + X_{35} + X_{36} \leq 21904$$
$$X_{41} + X_{42} + X_{43} + X_{44} + X_{45} + X_{46} \leq 6608$$
$$X_{51} + X_{52} + X_{53} + X_{54} + X_{55} + X_{56} \leq 8000$$
$$X_{61} + X_{62} + X_{63} + X_{64} + X_{65} + X_{66} \leq 5500$$

**Constraints set of demand:**

$$\sum_{i=1}^{6} X_{ij} \geq b_j \qquad (j - demand\ zone), \tag{4}$$

where $b_i$ is the demand amount of j-demand zone:

$$X_{11} + X_{21} + X_{31} + X_{41} + X_{51} + X_{61} \geq 24443$$

$$X_{12} + X_{22} + X_{32} + X_{42} + X_{52} + X_{62} \geq 10958$$
$$X_{13} + X_{23} + X_{33} + X_{43} + X_{53} + X_{63} \geq 9000$$
$$X_{14} + X_{24} + X_{34} + X_{44} + X_{54} + X_{64} \geq 6000$$
$$X_{15} + X_{25} + X_{35} + X_{45} + X_{55} + X_{65} \geq 4000$$
$$X_{16} + X_{26} + X_{36} + X_{46} + X_{56} + X_{66} \geq 34108$$

The set of constraints (3) defines the transportation limitations for *i*- product from production region to the transshipment point *j*.

$$X_{ij} \geq 0 \quad (i = the\ product), (j = demand\ point) \tag{5}$$

Constraints (5) ensure that decision variable are non-negative.

It is essentially that according to the data Table 3 the total supply amount of the company is equal to the total demand amount from the individual centers. Thus, we consider the balance problem and this fact can be expressed mathematically as:

$$\sum_{j=1}^{n} b_j = \sum_{i=1}^{m} a_i = 88509\ ton \tag{6}$$

TABLE 4. The market prices of the produced products are as follows:

| **Products** | **Unit price of product (Turkish lira)** |
|---|---|
| Steel Billet Products-1 | 1445 |
| Steel Billet Products-2 | 1560 |
| Steel Billet Products-3 | 2060 |
| Rebar Products-1 | 1712 |
| Rebar Products-2 | 2030 |
| Rebar Products-3 | 2200 |

## 2a. Solving the Problem by VAM Method

According to the VAM method, firstly, the differences between the smallest $C_{ij}$ for each row and column and the second smallest $C_{ij}$ are determined for the respective row and column [6,9]. Here $C_{ij}$ represents unit transportation costs in each frame.

According to Table 3, the differences (penalty values) for the each row (SA) following:

SA1=43-17=26; SA2=43-17=26;SA3=43-17=26;SA4=33-7=26;SA5=33-7=26;SA6=33-7=26

The differences (penalty values) for the each column (ST) defined as:

ST1=51-41=10;ST2=65-55=10;ST3=43-33=10;ST4=85-75=10;ST5=70-60=10;ST6=17-10=10

In generally, we must select the square with maximum penalty value. But one can see, there is equality between the calculated penalty values. So, the smallest cost square in the row is optimally assigned. It ıs $C_{ij} = 7$. If the assignment is made to the row with the smallest cost, i.e. $C_{56} = 7$, $X_{56} = 8000$ and according to the assigned frame, the order is filled and this row is drawn out and processed. This process is shown in Table 5:

TABLE 5. VAM Transportation Model

| | Kocaeli | İstanbul | Ankara | Izmir | Samsun | Karabuk | supply amount |
|---|---|---|---|---|---|---|---|
| Steel Billet Products-1 | $X_{11}$ 51 | $X_{12}$ 65 | $X_{13}$ 43 | $X_{14}$ 85 | $X_{15}$ 70 | $X_{16}$ 17 | 17440 |
| Steel Billet Products-2 | $X_{21}$ 51 | $X_{22}$ 65 | $X_{23}$ 43 | $X_{24}$ 85 | $X_{25}$ 70 | $X_{26}$ 17 | 29057 |
| Steel Billet Products-3 | $X_{31}$ 51 | $X_{32}$ 65 | $X_{33}$ 43 | $X_{34}$ 85 | $X_{35}$ 70 | $X_{36}$ 17 | 21904 |
| Rebar Products-1 | $X_{41}$ 41 | $X_{42}$ 55 | $X_{43}$ 43 | $X_{44}$ 75 | $X_{45}$ 60 | $X_{46}$ 7 | 6608 |
| Rebar Products-2 | $X_{51}$ 41 | $X_{52}$ 55 | $X_{53}$ 43 | $X_{54}$ 75 | $X_{55}$ 8000 | 60 7 | 8000 |
| Rebar Products-3 | $X_{61}$ 41 | $X_{62}$ 55 | $X_{63}$ 43 | $X_{64}$ 75 | $X_{65}$ 60 | $X_{66}$ 7 | 5500 |
| demand amount | 24443 | 10958 | 9000 | 6000 | 4000 | 34108 | 88509 |

Penalty values are recalculated for each remaining row and column. Penalty values for lines (SA):

SA1=43-17=26 ; SA2=43-17=26; SA3=43-17=26;SA4=33-7=26; SA6=33-7=26.

Penalty values for the each column (ST) defined as:

ST1=51-41=10; ST2=65-55=10; ST3=43-33=10; ST4=85-75=10; ST5=70-60=10; ST6=17-10=10.

In this stage we must take account a change was occurred in the demand of the sixth column due to the first operation. So, the demand amount decreases from 34108 tons to26108 tons.

Based on the same logic new assignments are the following cells:

$$X_{46} = 6608$$
$$X_{66} = 5500.$$

As the fourth and fifth lines are filled with their supply, the relevant rows are drawn out and removed from the operation.

After second stage, Rebar-1, Rebar -2 and Rebar-3 products have been completely distributed and the new appearance of the table is shown below.

TABLE 6. VAM Transportation Method

| products | Kocaeli | İstanbul | Ankara | Izmir | Samsun | Karabuk | supply amount |
|---|---|---|---|---|---|---|---|
| Steel Billet Products-1 | $X_{11}$ | 65 $X_{12}$ | 43 $X_{13}$ | 85 $X_{14}$ | 70 $X_{15}$ | 17 $X_{16}$ | 17440 |
| Steel Billet Products-2 | 51 $X_{21}$ | 65 $X_{22}$ | 43 $X_{23}$ | 85 $X_{24}$ | 70 $X_{25}$ | 17 $X_{26}$ | 29057 |
| Steel Billet Products-3 | 51 $X_{31}$ | 65 $X_{32}$ | 43 $X_{33}$ | 85 $X_{34}$ | 70 $X_{35}$ | 17 $X_{36}$ | 21904 |
| demand amount | 24443 | 10958 | 9000 | 6000 | 4000 | 14000 | 88509 |

On following stage, we calculate Penalty values for the remaining row and column, and the maximum value is placed on the smallest cost square, according to supply and demand constraints and the result will be the following distribution table:

TABLE 7. VAM the Transportation Method

| Products | Kocaeli | İstanbul | Ankara | Izmir | Samsun | Karabuk | supply amount |
|---|---|---|---|---|---|---|---|
| Steel Billet Products-1 | 2539 | 51 0 | 65 0 | 43 901 | 85 0 | 70 14000 | 17440 |
| Steel Billet Products-2 | 0 | 51 10958 | 65 9000 | 43 5099 | 85 4000 | 70 0 | 17 29057 |
| Steel Billet Products-3 | 21904 | 51 0 | 65 0 | 43 0 | 85 0 | 70 0 | 17 21904 |

| | | | | | | | |
|---|---|---|---|---|---|---|---|
| Rebar Products-1 | 0 | 41 0 | 55 0 | 33 0 | 75 0 | 60 6608 | 7 6608 |
| Rebar Products-2 | 0 | 41 0 | 55 0 | 33 0 | 75 0 | 60 8000 | 7 8000 |
| Rebar Products-3 | 0 | 41 0 | 55 0 | 33 0 | 75 0 | 60 5500 | 7 5500 |
| demand amount | 24443 | 10958 | 9000 | 6000 | 4000 | 34108 | 88509 |

TABLE 8. VAM transportation Model

| variable | value | variable | value | variable | value |
|---|---|---|---|---|---|
| X11 | 2539 | X31 | 21904 | X51 | 0 |
| X12 | 0 | X32 | 0 | X52 | 0 |
| X13 | 0 | X33 | 0 | X53 | 0 |
| X14 | 901 | X34 | 0 | X54 | 0 |
| X15 | 0 | X35 | 0 | X55 | 0 |
| X16 | 14000 | X36 | 0 | X56 | 8000 |
| X21 | 0 | X41 | 0 | X61 | 0 |
| X22 | 10958 | X42 | 0 | X62 | 0 |
| X23 | 9000 | X43 | 0 | X63 | 0 |
| X24 | 5099 | X44 | 0 | X64 | 0 |
| X25 | 4000 | X45 | 0 | X65 | 0 |
| X26 | 0 | X46 | 6608 | X66 | 5500 |

TOTAL COST Z=51*2539+85*901+17*14000+65*10958+43*9000+85*5099+ 70*4000+51*21904+7*6608+7*8000+7*5500=3514619(TL) (7)

Thus, the basic solution is completed with the VAM method. KH=n+m-1=6+6-1=11 is a number of used Cells. Here n and m are the total number of the rows and the column correspondingly.

## 2b. Solving the Problem by MODI Method.

In this section we will investigate the optimalness of the founding solution using the MODI method [6,10]. If the rows of the tables are denoted by $R_i$ and the columns are $K_j$, based on the $C_{ij}$ values for the filled squares, using the the formula

$$R_i + K_j = C_{ij},$$

we can calculate the coefficients $R_i$ and $K_j$ for each row and column, correspondingly:

$R_1=R_2=R_3=0, R_4=R_5=R_6=-10, K_1=51, K_2=65, K_3=43, K_4=85, K_5=70, K_6=17.$

TABLE 9. MODI Transportation Method Table

| | | K1=51 | K2=65 | K3=43 | K4=85 | K5=70 | K6=17 | |
|---|---|---|---|---|---|---|---|---|
| | products | Kocaeli | İstanbul | Ankara | Izmir | Samsun | Karabuk | supply amount |
| R1=0 | Steel Billet Products-1 | 51 2539 | 65 0 | 43 0 | 85 901 | 70 0 | 17 14000 | 17440 |
| R2=0 | Steel Billet Products-2 | 51 0 | 65 10958 | 43 9000 | 85 5099 | 70 4000 | 17 0 | 29057 |

| | | | | | | | | |
|---|---|---|---|---|---|---|---|---|
| R3=0 | Steel Billet Products-3 | 51 | 65 | 43 | 85 | 70 | 17 | |
| | | 21904 | 0 | 0 | 0 | 0 | 0 | 21904 |
| R4=-10 | Rebar Products-1 | 41 | 55 | 33 | 75 | 60 | 7 | |
| | | 0 | 0 | 0 | 0 | 0 | 6608 | 6608 |
| R5=-10 | Rebar Products-2 | 41 | 55 | 33 | 75 | 60 | 7 | |
| | | 0 | 0 | 0 | 0 | 0 | 8000 | 8000 |
| R6=-10 | Rebar Products-3 | 41 | 55 | 33 | 75 | 60 | 7 | |
| | | 0 | 0 | 0 | 0 | 0 | 5500 | 5500 |
| | demand amount | 24443 | 10958 | 9000 | 6000 | 4000 | 34108 | 88509 |

After the $R_i$ and $K_j$ development coefficients stated for each rows and columns of the table, the 'Development index' ($GI_{ij}$) for all empty (unused squares) are calculated by the formula

$GI_{ij}= C_{ij}-R_i-K_j$.

Now, let's calculate the Development Index (GI) for empty squares.

GI12=C12-R1-K2=65-0-65=0, GI13=C13-R1-K3=43-0-43=0,
GI15=C15-R1-K5=70-0-70=0, GI21=C21-R2-K1=51-0-51=0,
GI26=C26-R2-K6=17-0-17=0, GI32=C32-R3-K2=65-0-65=0,
GI33=C33-R3-K3=43-0-43=0, G34=C34-R3-K4=85-0-85=0,
GI35=C35-R3-K5=70-0-70=0, GI36=C36-R3-K6=17-0-17=0,
GI41=C41-R4-K1=41+10-51=0, GI42=C42-R4-K2=55+10-65=0,
GI43=C43-R4-K3=33+10-43=0, GI44=C44-R4-K4=75+10-85=0,
GI45=C45-R4-K5=60+10-70=0, GI51=C51-R5-K1=41+10-51=0,

GI52=C52-R5-K2=55+10-65=0, GI53=C53-R5-K3=33+10-43=0,
GI54=C54-R5-K4=75+10-85=0, GI55=C55-R5-K5=60+10-70=0,
GI61=C61-R6-K1=41+10-51=0, GI62=C62-R6-K2=55+10-65=0,
GI63=C63-R6-K3=33+10-43=0, GI64=C64-R6-K4=75+10-85=0,
GI65=C65-R6-K5=60+10-70=0.

If the Development Indices are not negative, it means that the optimal solution is found.

**2c. Solving the Problem with the Simplex Method**

The solution of the transportation problem can be made not only with the traditional transportation model methods, but also using of the linear programing method [11-14]. Linear programming is a method to achieve the best outcome (such as maximum profit or lowest cost) in a mathematical model whose requirements are represented by linear relationships.

Linear programming is a technique in which we maximize or minimize a function. Every linear programming problem can be written in the following standard form

$$Maximize\ \zeta = c^T x \tag{8}$$

subject to

$$Ax = b,$$
$$x \geq 0 \tag{9}$$

The Simplex Method developed in [14] is the earliest solution algorithm for solving LP problems. It is an efficient implementation of solving a series of systems of linear equations. By using a greedy strategy while jumping from a feasible vertex of the next adjacent vertex, the algorithm terminates at an optimal solution. Simplex method uses row operations to obtain the maximum or minimum values of *function*. The simplex method moves from one extreme point to one of its neighboring extreme point. Typical uses of the simplex algorithm are to find the right mix of ingredients at the lowest cost (the goal). If the ingredients are food, the constraints would be having at least so many calories, so much protein, fats, carbohydrates, vitamins, minerals, etc.

R is a free software programming language and software environment for statistical computing and graphics. The R language is widely used among statisticians and data miners for developing statistical software and data analysis [15]. The optimal

solution for this application has been solved with the R / SIMPLEX package program [15] and the results are shown in Table 9.

TABLE 10. Transportation Table Simplex Solution Results

| variable | value | variable | value | variable | value |
|---|---|---|---|---|---|
| X11 | 0 | X31 | 4335 | X51 | 8000 |
| X12 | 0 | X32 | 10958 | X52 | 0 |
| X13 | 0 | X33 | 6611 | X53 | 0 |
| X14 | 0 | X34 | 0 | X54 | 0 |
| X15 | 0 | X35 | 0 | X55 | 0 |
| X16 | 17440 | X36 | 0 | X56 | 0 |
| X21 | 0 | X41 | 6608 | X61 | 5500 |
| X22 | 0 | X42 | 0 | X62 | 0 |
| X23 | 2389 | X43 | 0 | X63 | 0 |
| X24 | 6000 | X44 | 0 | X64 | 0 |
| X25 | 4000 | X45 | 0 | X65 | 0 |
| X26 | 16668 | X46 | 0 | X66 | 0 |

Resulting solutions which obtained by the linear programming are as follows

TABLE 11. The optimal solution of the transportation problem by R / SIMPLEX paket program

| products | Kocaeli | İstanbul | Ankara | Izmir | Samsun | Karabuk | supply amount |
|---|---|---|---|---|---|---|---|
| Steel Billet Products-1 | 0 | 0 | 65 0 | 43 0 | 85 0 | 70 17440 | 17 17440 |
| Steel Billet Products-2 | 0 | 51 0 | 65 2389 | 43 6000 | 85 4000 | 70 16668 | 17 29057 |

| | | | | | | | |
|---|---|---|---|---|---|---|---|
| Steel Billet Products-3 | 4335 | 51 10958 | 65 6611 | 43 0 | 85 0 | 70 0 | 17 21904 |
| Rebar Products-1 | 6608 | 41 $X_{42}$ | 55 $X_{43}$ | 33 $X_{44}$ | 75 $X_{45}$ | 60 0 | 7 6608 |
| Rebar Products-2 | 8000 | 41 $X_{52}$ | 55 $X_{53}$ | 33 $X_{54}$ | 75 $X_{55}$ | 60 0 | 7 8000 |
| Rebar Products-3 | 5500 | 41 $X_{62}$ | 55 $X_{63}$ | 33 $X_{64}$ | 75 $X_{65}$ | 60 0 | 7 5500 |
| demand amount | 24443 | 10958 | 9000 | 6000 | 4000 | 34108 | 88509 |

Thus, according to the table 10, the minimum value of the Total Transportation Cost is equal to:

**Z**=17*17440+43*2389+85*6000+70*4000+
7*16668+51*4335+65*10958+43*6611+41*6608+41*8000+41*5500=3514619 (TL) . (10)

In comparison, the results obtained by VAM transportation Model (7) with the optimal solution of the transportation problem by R / SIMPLEX packaged software (8), we can reach this conclusion: although we have two different distribution plans, the optimal total transportation cost is the same in both cases and equal to $Z_{min}$=3514619 (TL) .

## 3. Calculation of the Dollar Exchange Rate Fluctuations

The fluctuation of the dollar currency is reflected in fuel price and, consequently, affects on the total transportation costs. For this reason, let's examine how the total transportation costs change with the 5% increase and decrease in unit transportation costs.

Table 12. The coefficients of $C_{ij}$ in the Objective Function by 5% Unit transport price increasing

| Coefficients Cij | Value | Coefficients Cij | Value | Coefficients Cij | Value |
|---|---|---|---|---|---|
| C11 | 53.55 | C31 | 53.55 | C51 | 43.05 |
| C12 | 68.25 | C32 | 68.25 | C52 | 57.75 |
| C13 | 45.15 | C33 | 45.15 | C53 | 34.65 |
| C14 | 89.25 | C34 | 89.25 | C54 | 78.75 |
| C15 | 73.50 | C35 | 73.50 | C55 | 63.00 |
| C16 | 17.85 | C36 | 17.85 | C56 | 7.35 |
| C21 | 53.55 | C41 | 43.05 | C61 | 43.05 |
| C22 | 68.25 | C42 | 57.75 | C62 | 57.75 |
| C23 | 45.15 | C43 | 34.65 | C63 | 34.65 |
| C24 | 89.25 | C44 | 78.75 | C64 | 78.75 |
| C25 | 73.50 | C45 | 63.00 | C65 | 63.00 |
| C26 | 17.85 | C46 | 7.35 | C66 | 7.35 |

We observe that there is no change in the resulting distribution plan. But we can say that the total transportation cost has increased significantly. We see that the value of the Total transportation cost will be $Z_{min}$ =3690349.95TL, i.e. an increase by 175730.95 TL.

Similarly, the decreasing of the unit transport prices lead to a decreasing of the total transportation cost, a namely:

Table 13. The coefficients of $C_{ij}$ in the Aim Function by 5% Unit transport price decreasing

| Coefficients Cij | Value | Coefficients Cij | Value | Coefficients Cij | Value |
|---|---|---|---|---|---|
| C11 | 48.45 | C31 | 48.45 | C51 | 38.95 |
| C12 | 61.75 | C32 | 61.75 | C52 | 52.25 |
| C13 | 40.85 | C33 | 40.85 | C53 | 31.35 |
| C14 | 80.75 | C34 | 80.75 | C54 | 71.25 |
| C15 | 66.5 | C35 | 66.5 | C55 | 57 |

| | | | | | |
|---|---|---|---|---|---|
| C16 | 16.15 | C36 | 16.15 | C56 | 6.65 |
| C21 | 48.45 | C41 | 38.95 | C61 | 38.95 |
| C22 | 61.75 | C42 | 52.25 | C62 | 52.25 |
| C23 | 40.85 | C43 | 31.35 | C63 | 31.35 |
| C24 | 80.75 | C44 | 71.25 | C64 | 71.25 |
| C25 | 66.5 | C45 | 57 | C65 | 57 |
| C26 | 16.15 | C46 | 6.65 | C66 | 6.65 |

In this case the Total transportation cost will be $Z_{min}$=3338888.05TL, i.e. the value of the cost will decrease by 175730.95 TL.

## 6. Conclusion

In this paper the optimum solution of the transportation model were obtained by using the traditional transportation model methods such as VAM, MODI and the linear programming model (using R /SIMPLEX package software). Here we consider the single source transportation model, namely, all demand amounts are met from a single production center. Results of calculations practically coincide for different approaches.

## References

[1] https://www.worldsteel.org/media-centre/blog/2019
[2] https://**www.oecd.org**/sti/ind/Item 4.7 **Turkish** Iron/2018
[3] https://www.**worldsteel**.org/media-centre/press-releases/**2020**/**February-2020**-crude-**steel**.
[4] Nikolic, N., Total Time Minimizing Transportation Problem, Yugoslav Journal of Operations Research, Belgrade University, December, No 1, 2006.
[5] Sarıaslan, Halil, Karacabey, Argun, Gökgöz, Fazil, Nicel karar yöntemleri, Siyasal Kitap Evi, Ankara, 704 s., 2017.
[6] Frank R. Giordano, .D.Weir, W.P.Fox Mathematical Modelling, Thomson Books, 2002, 538 p.
[7] Balakrishnan, A., Render, Stair, Managerial Decision Modeling With Spread Heats, 2nd ed, Upper Saddle River, NJ, Prentice Hall, 2006.
[8] Shenoy, G.V., Srivastava, U.K., Operations Research for Management, New Delhi, 1986.
[9] Encyclopedia of Operations Research and Management Science, Editors: Saul I. Gass, Carl M. Harris, 2001.
[10] Gill, P.E., Murray, W., Wright, M.H., Numerical Linear Algebra and Optimization, Vol. 1., Addison-Wesley, 1991.

[11] Press, W.H., Teukolsky, S.A., Vetterling, W.T, Flannery, B.P., Numerical Recipes: The Art of Scientific Computing (Second Edition), Cambridge University Press, 1992.
[12] Winston, W.L., Operations Research: Applications and Algorithms, Duxbury Pres, California, 1994.
[13] Dantzig, G.B., Linear programming and extensions, Princeton N.J. , Princeton University Press, 1963.
[14] Fox, John, Andersen, Robert, Using the R Statistical Computing Environment to Teach Social Statistics, Department of Sociology, McMaster University. (January 2005), Retrieved 6 August 2018.

*Current Address:* Department of Business Administration of Karabuk University, Karabuk, Turkey
*E-mail:* raskerbeyli@karabuk.edu.tr
*ORCID:* http://orcid.org/0000-0001-6417-0939

Commun.Fac.Sci.Univ.Ank.Series A2-A3
Volume 62, Number 1, Pages 100-114 (2020)
DOI: 10.33769/aupse.673996
ISSN 1303-6009 E-ISSN 2618-6462
http://communications.science.ankara.edu.tr/index.php?series=A2A3

# EVALUATION OF MS-DIAL AND MZMINE2 SOFTWARES FOR CLINICAL LIPIDOMICS ANALYSIS

Engin KOÇAK

ABSTRACT. Lipidomics covers analysis of all lipid species in an organism. Lipid metabolism is one of the key factors to understand cellular processes at molecular level. Lipidomics has been used to find diagnostic and prognostic biomarkers in clinical sample (plasma, serum, urine, tissue). Today mass spectroscopy based approach dominates lipidomics and several computational platforms have been developed to process raw mass spectra data. However, there is no routine procedure for data processing in lipidomics. In present work, two different bioinformatics platforms, which are MS-DIAL and MZmine2, was compared for lipidomics analysis of plasma sample. Peak detection, identification and quantification parameters were investigated to understand advantages and disadvantages. In peak detection process, it was observed that MZmine2 detected more peak than MS-DIAL at same threshold level. In identification process, Lipidmaps database was used for identification. MZmine2 identifies more lipid than MS-DIAL. Semi-quantification is very important to find differentially expressed lipid species and biomarkers in clinical studies. MS-DIAL and MZmine2 calculated normalized peak intensities and results were compared to understand reproducibility. Average relative standard deviation of all peaks was calculated and results showed that MS-DIAL gives more reproducible results than MZmine2. In conclusion, MZmine2 and MS-DIAL could be used in clinical lipidomics studies.

## 1. INTRODUCTION

In recent years omics technologies have been emerged as essential tools to observe cellular processes at molecular level [1]

Genomics is the motherland of omics technologies. However, results of human genome project, which was ended in 2003, indicated that genome analysis is not

Received by the editors: January 13, 2020; Accepted: May 07, 2020.
*Key word and phrases:* Lipidomics, bioinformatics, MS-dial, MZmine2

sufficient to understand cellular process [2]. Because of this fact, post-genomic studies have drawn attention to complete genomics.

In post-genomic area, transcriptomics is the global analysis of mRNA, which is the product of transcription process [3]. Proteomics is another phoneme, which is the analysis of all gene-encoded proteins in cells and also post-translational modifications on protein structure [4]. Metabolomics is analysis of metabolites, which are side or end products of biological reactions (Figure 1) [5].

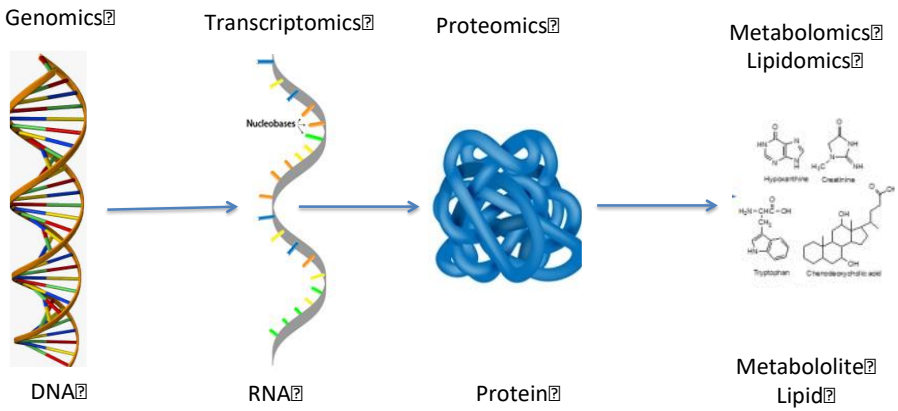


FIGURE 1. Omics technologies.

Lipidomics firstly described as a sub-discipline in metabolomics and covered analysis of all lipid spices in organism. Lipids play essential roles in cell structures, communication and trafficking [6]. In cell structure there are several thousand of lipid isoforms and in lipidomics each isoform structure should be evaluated in qualitative and quantitative analysis. In lipidomics workflow there are three steps. The first step is the extraction of lipids from biological specimen like cells, bacteria, tissue, plant, and body fluid. Currently various extraction methods are used for lipid isolation. Methanol/Chloroform and Methanol/terbutyl ether mixtures are most commonly used co-solvent systems in lipid extractions [7]. In second step, extracted lipid molecules are analyzed in analytical systems. Biological samples contained thousands of lipid molecules. Because of this biological complexity, there is a great demand for sensitive, reproducible analytical systems. Today liquid chromatography-mass spectroscopy system (LC/MS) is the most suitable combined

analytical system for lipidomics analysis [8-10]. Lipid species separated according to their polarity in LC system and analyzed in mass spectroscopy. Mass spectroscopy gives MS data for each lipid molecule. Commonly high sensitive LC/MS systems like LC/Q-TOF or LC/orbitrap system have been used in lipidomics analysis.

The last step in lipidomics is data process of raw MS data in computational platforms. In a single LC/MS analysis, thousand of MS data have been recorded. Analysis of this huge output is one of the biggest challenges in lipidomics analysis. Today various computational platforms have been developed for MS data processing [11-14]. Reliable lipid identification and semi quantification is the main purpose in computational lipidomics. Workflow of lipidomics software includes peak detection, filtering, deconvolution, intensity calculation, gap filling, identification and normalization.

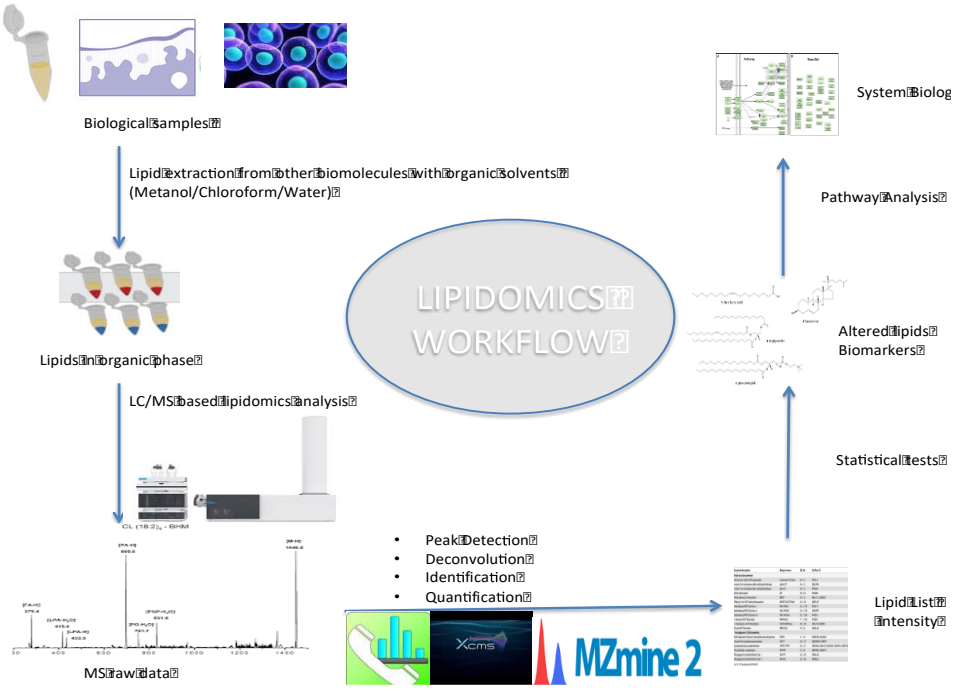


FIGURE 2. Classical LC/MS based lipidomics workflow.

MS-DIAL, which has been developed by Hiroshi Tsugova, has been used for untargeted metabolomics and lipidomics studies extensively [15-17]. In MS-DIAL

pipeline precursor ion peaks efficiently spotted by exploring two continuous data axes: retention times and accurate mass. Deconvolution mode is used to find individual peaks. Peak intensities are calculated according to peak height and area. Lipid molecules are identified with mass annotation (MS1 data) or MS2 data.
Another computational platform for metabolomics and lipidomics is Mzmine2 [18], which has similar workflow with MS-DIAL but it contains different peak detection, deconvolution and gap filling methods.

In present work, lipid profile of plasma was investigated by using Mzmine2 and MSDIAL. Peak detection, identification and quantification parameters were compared and discussed to understand advantages of software for clinical lipidomics.

## 2. EXPERIMENTAL

### 2.1. Sample Preparation

Lipidome structure of commercial plasma samples (100µL) (sigma) was analyzed in present work. Lipids in plasma were extracted by traditional methanol (300µL) /water (150µL)/chloroform (300µL) co solvent system. Lipids were extracted in chloroform phase. Chloroform was evaporated in vacuum centrifuge and lipids were solubilized in isopropyl alcohol and diluted mobile phase. We prepared three replicate for lipidomics analysis.
2.2. LC/MS Analysis

Lipids were separated in C18 column by performed Agilent 1290 HPLC system. In LC system, water (A) and ACN:Isopropyl alcohol (Sigma) (70:30 v/v) (B) were used a mobile phase. Aqueous and organic phase contained 1% 1M ammonium acetate - 0.1% acetic acid. Flow rate was adjusted as 0.20 mL/min. Elution gradient started with 55% B and it was risen up linearly 75% until $3^{th}$ minute, 89% until $8^{th}$ minute and 100% until $11^{th}$ minute. The ratio was kept constant till $15^{th}$ minute. The organic phase ratio will be decreased to 55% till 20th minute and 5-minute post run will be applied for further injections. Column temperature was set at $60^{o}$C. After LC separation, lipids were analyzed in Agilent 6530 QTOF-MS system. Lipids were analyzed in positive mode. Scan range was 100-1700 m/z. Capillary voltage was 3500 V.

## 2.3. Data Processing

MS-DIAL workflow

The raw MS data, which was in MzmL format, were converted to abf. With abf converter (https://www.reifycs.com/AbfConverter/) format. MS-DIAL 3.30 was downloaded from http://prime.psc.riken.jp/Metabolomics_Software/MS-DIAL/. In first step, ionization mode (positive), data type (centroid) was selected. In peak detection process, threshold of peak intensity was selected as 10000 amplitude. Linear weighted moving average method was preferred for smoothing and peak width was adjusted as 5. In deconvolution process, sigma window value was selected as 0.5. Retention time and mass tolerance was selected 2 min. and 10 ppm for gap filling process. In peak alignment process, retention time tolerance and MS1 tolerance were set up at 0.05 min and 0.04 Da. Total peak areas were used for peak intensity calculation and total ion intensity was used for normalization (Figure 3).

MZmine2

In data process by performed MZmine2(http://mzmine.github.io/download.html), raw MS data in mzML format was imported. Mass detection and ADAP chromatogram builder was performed to detected peaks. Minimum intensity was selected as 10000 amplitudes as well MS-DIAL. In peak smoothing process, peak width was adjusted as 5 as well as MSDIAL. In deconvolution, wavelet (ADAP) algorithm was used to separate overlapped peaks. Retention time tolerance was adjusted as 2 min and mass tolerance 10 ppm as well as MS-DIAL for gap filling. In addition, Intensity tolerance, which is another option in Mzmine2, was selected default value (10%). Linear normalization algorithm was used to normalize peaks area for relative quantification. In normalization process, total ion intensity was used to avoid experimental errors (Figure 3).

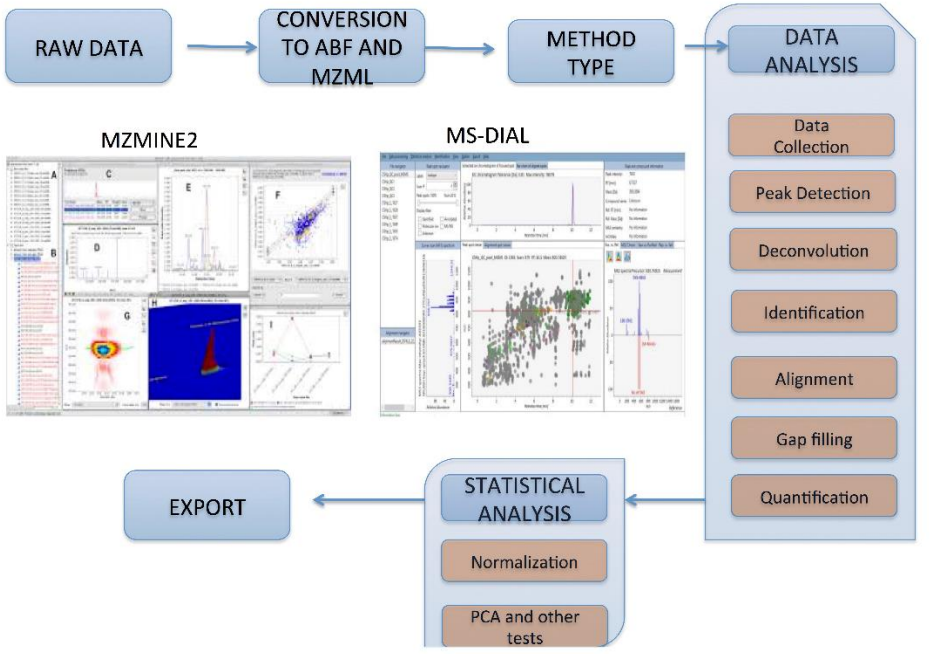


FIGURE 3. Workflow of MZmine2 and MS-DIAL

## 3. RESULTS AND DISCUSSION

Lipidomics, defined as the large-scale study of cellular lipids (i.e., the lipidome), has recently emerged as a rapidly expanding research field under the umbrella of systems biology. New analytical systems (NMR or Mass spectroscopy) have been developed in lipidomics to observe cellular process. However, there is a great demand to process raw outputs of analytical systems accurately. In present work, two promising platforms were compared for plasma lipidome profiling which is valuable specimen in clinical studies to find biomarkers. Peak detection, identification and quantification steps were evaluated for both platforms.

### 3.1. Peak Detection

The first step in lipidomics analysis is to detect peaks accurately. In peak detection, threshold of peak intensity is the most important parameter. High threshold causes

loss of many lipid species. Low threshold leads false negative identifications. In present work, threshold was selected as 10000 amplitudes for MS-DIAL and MZmine2. This level has been used in various lipidomics studies. In current stats, MS-DIAL detected 1157 and MZmine2 detected 1437 peaks
(Figure 4).

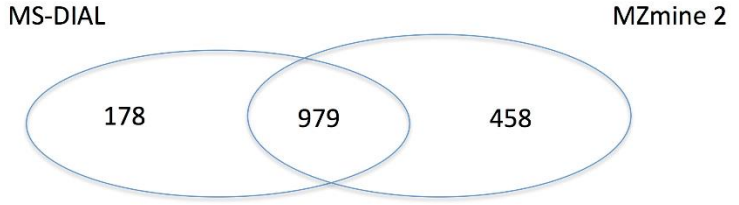


FIGURE 4. Number of detected peaks in MS-DIAL and MZmine2

Peak deconvolution is the second step after peak detection. The process of data deconvolution, sometimes called peak picking, is in itself a complex process caused by the complexity of the data and variation introduced during the process of data acquisition related to mass-to-charge ratio, retention time and chromatographic peak area. In deconvolution process, overlapped peaks separated to enhance analytical resolution.

The gap filling is another important parameter for lipidomics analysis. The gap filling process allowed us to connect identified metabolites and detection of metabolites that had been discarded during the data pre-processing or simply were not detected due to the LC/MS configuration. This is important to match identified and detected species between technical replicates. Mzmine2 software allows options to select gap filling ratio. MS-DIAL has automatic gap filling algorithm.

### 3.2. Peak Identification

In identification process MZmine2 offers two different routes. The first one is local MZmine2 lipid database and online lipidmaps database search option. MS-DIAL also offers two different identification routes. The first one lipidblast database module. The other way is transferring of MS-DIAL results to MS-FINDER, which include lipidmaps database, to match MS1 results with lipidmaps database. To evaluate identification yield of two softwares, lipidmaps database search option was used for both software. 189 lipid species were identified in MS-DIAL. In MZmine2, using lipidmaps database identified 155 lipid species. 121 lipid spices were

commonly identified with MZmine2 and MS-DIAL. 16.33% of detected peaks were identified in MS-DIAL and 10.78% of detected peaks were identified in MZmine 2. These lipids were listed in supplementary information.

### 3.3. Relative quantification of lipid species

In relative quantification process, peak intensities of lipid species in different experimental groups are compared to find statistically altered lipids in clinic samples. In lipidomics studies peak areas or peak heights are used for relative quantification between experimental groups. The peak of PG (16:0/0:0), which was detected in three replicates, was represented as an example in Figure 5.

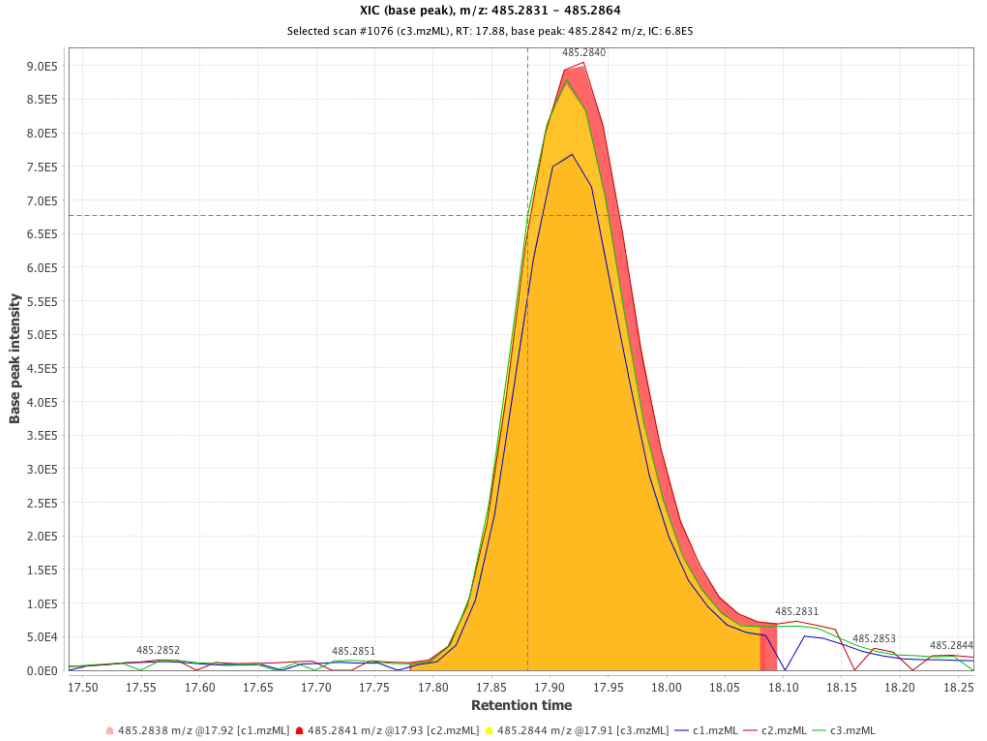


FIGURE 5. Peak of PG (16:0/0:0), wich was detected in three technical replicate. Peak area calculated by MS-DIAL and Mzmine2 automatically.

In MS-DIAL and MZmine2 workflow, peak heights or peak areas could be calculated. Normalization is an important step in relative quantification. In both platforms, internal standard could be used for normalization. Moreover, total ion

intensity could be also used for normalization process. In present work, total ion intensity of all identified lipids was used for normalization.

In present work, peak areas of lipid species were calculated by using MS-DIAL and MZmine2. Average relative standard deviation values were calculated for both software to understand relative reproducibility. Moreover, two sample t-test was used to observe if MSDIAL and MZmine2 give similar quantification results in plasma sample.

Average relative standard deviations of peak areas of identified lipids were calculated for both software. Average relative standard deviation was calculated as 10.2% for MS-DIAL and 16.3% for MZmine2. This result showed that MS-DIAL gives more reproducible results than MZmine2. We used two sample t-test to compare identified lipid intensities. Results showed there is no statistical difference for 98 lipid species. Intensities of 23 lipid species were differently calculated in MZmine2 and MS-DIAL. This result showed that MZmine2 and MS-DIAL give similar results for many lipid species in clinical samples.

## 4. Conclusion

In present work, MS-DIAL and MZmine2 software were compared by using LC/MS lipidomics data. In peak detection and identification process, MZmine2 provides to analyze more lipid species. However, MS-DIAL gives more reproducible results for quantification of lipid species. These two platforms have been used for lipidomics and metabolomics analysis. Present work will contribute to make more detailed and reliable lipidomics analysis.

## Supplementary Information

| No | Lipids |
|---|---|
| 1 | Xeniasterol-b;1alpha,25-dihydroxy-2beta-(3-hydroxypropoxy)vitamin D3 / 1alpha,25-dihydroxy-2beta-(3-hydroxypropoxy) cholecalciferol; |
| 2 | Wuhanic acid |
| 3 | Stoloniferone F;3alpha,7alpha,12alpha-Trihydroxy-24-methyl-5beta-cholest-23-en-26-oic acid |
| 4 | Spheroidene;Dihydroanhydrorhodovibrine/ Dihydromethoxylycopene |
| 5 | Rhodovibrin;3,4-Dihydrospheroidenone |
| 6 | PS(P-16:0/12:0) |
| 7 | PS(P-16:0/12:0) |
| 8 | PS(18:0/12:0);PS(17:0/13:0);PS(13:0/17:0);PS(12:0/18:0);PS(16:0/14:0);PS(15:0/15:0);PS(14:0/16:0) |
| 9 | PS(17:2(9Z,12Z)/0:0);Epothilone B |

| | |
|---|---|
| 10 | PS(17:0/22:0);PS(18:0/21:0);PS(19:0/20:0);PS(20:0/19:0);PS(22:0/17:0);PS(21:0/18:0) |
| 11 | PS(12:0/19:0);PS(13:0/18:0);PS(14:0/17:0);PS(17:0/14:0);PS(18:0/13:0);PS(19:0/12:0);PS(16:0/15:0);PS(15:0/16:0) |
| | |
| 12 | PKODiA-PA |
| 13 | PI(O-16:0/19:1(9Z));PI(O-18:0/17:1(9Z));PI(O-20:0/15:1(9Z));PI(P-16:0/19:0);PI(P-18:0/17:0);PI(P-20:0/15:0) |
| 14 | PI-Cer(d18:1/14:0) |
| 15 | PGF2alpha dimethyl amide;N-(3-oxo-octadecanoyl)-homoserine lactone;5,6-DiHETrE-EA;8,9-DiHETrE-EA;14,15-DiHETrE-EA;11,12-DiHETrE-EA |
| 16 | PG(P-20:0/19:1(9Z)) |
| 17 | PG(P-16:0/20:5(5Z,8Z,11Z,14Z,17Z)) |
| 18 | PG(P-16:0/15:1(9Z)) |
| 19 | PG(O-16:0/20:2(11Z,14Z));PG(O-18:0/18:2(9Z,12Z));PG(P-16:0/20:1(11Z));PG(P-20:0/16:1(9Z));PG(P-18:0/18:1(9Z)) |
| 20 | PG(O-16:0/18:2(9Z,12Z));PG(P-18:0/16:1(9Z));PG(P-20:0/14:1(9Z));PG(P-16:0/18:1(9Z)) |
| 21 | PG(20:0/22:1(11Z));PG(20:1(11Z)/22:0);PG(22:1(11Z)/20:0);PG(22:0/20:1(11Z)) |
| 22 | PG(17:0/22:1(11Z));PG(17:1(9Z)/22:0);PG(18:1(9Z)/21:0);PG(19:0/20:1(11Z));PG(19:1(9Z)/20:0);PG(20:0/19:1(9Z));PG(20:1(11Z)/19:0);PG(21:0/18:1(9Z));PG(22:0/17:1(9Z));PG(22:1(11Z)/17:0) |
| 23 | PG(16:0/0:0) |
| 24 | PG(16:0/0:0) |
| 25 | PG(13:0/22:1(11Z));PG(14:1(9Z)/21:0);PG(15:0/20:1(11Z));PG(15:1(9Z)/20:0);PG(16:0/19:1(9Z));PG(16:1(9Z)/19:0);PG(17:1(9Z)/18:0);PG(18:0/17:1(9Z));PG(18:1(9Z)/17:0);PG(19:0/16:1(9Z));PG(19:1(9Z)/16:0);PG(20:0/15:1(9Z));PG(20:1(11Z)/15:0);PG(21:0/14:1(9Z));PG(22:1(11Z)/13:0);PG(17:0/18:1(9Z));PG(16:0/18:0(11Cp)) |
| 26 | Pectenolone;(3S,4R,3'R)-4-Hydroxyalloxanthin;(3S,4S,3'R)-4-Hydroxyalloxanthin;Phoenicoxanthin/ Adonirubin/ 3-Hydroxycanthaxanthin |
| 27 | PE(P-20:0/22:6(4Z,7Z,10Z,13Z,16Z,19Z)) |
| 28 | PE(P-16:0/0:0) |
| 29 | PE(20:4(5Z,8Z,11Z,14Z)/0:0);PE(0:0/20:4(5Z,8Z,11Z,14Z));PE(0:0/20:4(8Z,11Z,14Z,17Z));PE(20:4(8Z,11Z,14Z,17Z)/0:0) |
| 30 | PE(20:3(8Z,11Z,14Z)/0:0);PE(0:0/20:3(11Z,14Z,17Z));PE(0:0/20:3(5Z,8Z,11Z));PE(0:0/20:3(8Z,11Z,14Z));PE(20:3(11Z,14Z,17Z)/0:0);PE(20:3(5Z,8Z,11Z)/0:0) |
| 31 | PE(12:0/16:1(9Z));PE(13:0/15:1(9Z));PE(14:0/14:1(9Z));PE(14:1(9Z)/14:0);PE(15:1(9Z)/13:0);PE(16:1(9Z)/12:0) |
| 32 | PE(12:0/15:1(9Z));PE(13:0/14:1(9Z));PE(14:1(9Z)/13:0);PE(15:1(9Z)/12:0) |
| 33 | PC(P-20:0/22:6(4Z,7Z,10Z,13Z,16Z,19Z)) |
| 34 | PC(P-16:0/20:5(5Z,8Z,11Z,14Z,17Z)) |
| 35 | PC(P-16:0/17:2(9Z,12Z));PE(O-18:0/18:3(6Z,9Z,12Z));PE(O-18:0/18:3(9Z,12Z,15Z));PE(O-16:0/20:3(8Z,11Z,14Z));PE(P-16:0/20:2(11Z,14Z));PE(P-18:0/18:2(9Z,12Z));GlcCer(d18:2(4E,8Z)/17:0(2OH[R]));GlcCer(d15:2(4E,6E)/20:0(2OH)) |
| 36 | PC(O-18:2(9Z,12Z)/2:0);PC(20:2(11Z,14Z)/0:0) |
| 37 | PC(O-18:1(10E)/2:0);PC(O-18:1(9Z)/2:0);PC(P-18:0/2:0);PC(20:1(9Z)/0:0);PC(20:1(11Z)/0:0) |
| 38 | PC(O-16:1(11Z)/2:0);PC(P-16:0/2:0);PC(18:1(6Z)/0:0);PC(18:1(9E)/0:0);PC(18:1(9Z)/0:0);PC(0:0/18:1(6Z));PC(0:0/18:1(9E));PC(0:0/18:1(9Z));PC(18:1(9Z)/0:0)[rac];PC(18:1(11Z)/0:0) |
| 39 | PC(O-16:0/18:3(6Z,9Z,12Z));PC(O-16:0/18:3(9Z,12Z,15Z));PC(O-16:1(9Z)/18:2(9Z,12Z));PC(P-16:0/18:2(9Z,12Z));PC(P-18:1(11Z)/16:1(9Z));PC(P-18:1(9Z)/16:1(9Z));PE(P-20:0/17:2(9Z,12Z)) |
| 40 | PC(O-16:0/0:0) |
| 41 | PC(22:6(4Z,7Z,10Z,13Z,16Z,19Z)/0:0) |

| | |
|---|---|
| 42 | PC(22:5(4Z,7Z,10Z,13Z,16Z)/0:0);PC(22:5(7Z,10Z,13Z,16Z,19Z)/0:0) |
| 43 | PC(22:4(7Z,10Z,13Z,16Z)/0:0) |
| 44 | PC(22:0/22:6(4Z,7Z,10Z,13Z,16Z,19Z));PC(22:2(13Z,16Z)/22:4(7Z,10Z,13Z,16Z));PC(22:4(7Z,10Z,13Z,16Z)/22:2(13Z,16Z));PC(22:6(4Z,7Z,10Z,13Z,16Z,19Z)/22:0) |
| 45 | PC(21:0/22:6(4Z,7Z,10Z,13Z,16Z,19Z));PC(22:6(4Z,7Z,10Z,13Z,16Z,19Z)/21:0) |
| 46 | PC(20:5(5Z,8Z,11Z,14Z,17Z)/22:5(7Z,10Z,13Z,16Z,19Z));PC(20:4(5Z,8Z,11Z,14Z)/22:6(4Z,7Z,10Z,13Z,16Z,19Z));PC(22:6(4Z,7Z,10Z,13Z,16Z,19Z)/20:4(5Z,8Z,11Z,14Z)) |
| 47 | PC(20:4(5Z,8Z,11Z,14Z)/0:0);PC(0:0/20:4(5Z,8Z,11Z,14Z));PC(20:4(8Z,11Z,14Z,17Z)/0:0) |
| 48 | PC(20:3(8Z,11Z,14Z)/0:0);PC(20:3(5Z,8Z,11Z)/0:0) |
| 49 | PC(20:0/22:6(4Z,7Z,10Z,13Z,16Z,19Z));PC(20:2(11Z,14Z)/22:4(7Z,10Z,13Z,16Z));PC(20:4(5Z,8Z,11Z,14Z)/22:2(13Z,16Z));PC(20:5(5Z,8Z,11Z,14Z,17Z)/22:1(11Z));PC(22:1(11Z)/20:5(5Z,8Z,11Z,14Z,17Z));PC(22:2(13Z,16Z)/20:4(5Z,8Z,11Z,14Z));PC(22:4(7Z,10Z,13Z,16Z)/20:2(11Z,14Z));PC(22:6(4Z,7Z,10Z,13Z,16Z,19Z)/20:0);LacCer(d18:1/16:0);Manbeta1-4Glcbeta-Cer(d18:1/16:0);Galalpha1-4Galbeta-Cer(d18:1/16:0) |
| 50 | PC(18:3(9Z,12Z,15Z)/0:0);PC(18:3(6Z,9Z,12Z)/0:0) |
| 51 | PC(15:1(9Z)/0:0);PE(18:1(9Z)/0:0);PE(0:0/18:1(11Z));PE(0:0/18:1(9Z));PE(18:1(11Z)/0:0) |
| 52 | PC(15:0/0:0);PE(18:0/0:0);PE(0:0/18:0);1-(2-methoxy-6Z-heptadecenyl)-sn-glycero-3-phosphoethanolamine |
| 53 | PC(13:0/0:0);PE(16:0/0:0);PE(0:0/16:0);1-(2-methoxy-13-methyl-6Z-tetradecenyl)-sn-glycero-3-phosphoethanolamine;1-(2-methoxy-6Z-pentadecenyl)-sn-glycero-3-phosphoethanolamine |
| 54 | PA(P-16:0/14:1(9Z)) |
| 55 | PA(O-20:0/22:6(4Z,7Z,10Z,13Z,16Z,19Z)) |
| 56 | PA(O-18:0/17:2(9Z,12Z));PA(P-16:0/19:1(9Z));PA(P-18:0/17:1(9Z));PA(P-20:0/15:1(9Z));SM(d18:2/14:0);PE-Cer(d14:2(4E,6E)/21:0);PE-Cer(d15:2(4E,6E)/20:0);PE-Cer(d16:2(4E,6E)/19:0) |
| 57 | PA(O-16:0/22:6(4Z,7Z,10Z,13Z,16Z,19Z));PA(P-18:0/20:5(5Z,8Z,11Z,14Z,17Z)) |
| 58 | PA(O-16:0/22:2(13Z,16Z));PA(O-18:0/20:2(11Z,14Z));PA(O-20:0/18:2(9Z,12Z));PA(P-16:0/22:1(11Z));PA(P-18:0/20:1(11Z));PA(P-20:0/18:1(9Z)) |
| 59 | PA(O-16:0/17:2(9Z,12Z));PA(P-16:0/17:1(9Z));PA(P-18:0/15:1(9Z)) |
| 60 | PA(O-16:0/0:0) |
| 61 | PA(18:0/18:1(9Z));PA(14:0/22:1(11Z));PA(14:1(9Z)/22:0);PA(15:1(9Z)/21:0);PA(16:1(9Z)/20:0);PA(17:0/19:1(9Z));PA(17:1(9Z)/19:0);PA(19:0/17:1(9Z));PA(19:1(9Z)/17:0);PA(20:0/16:1(9Z));PA(20:1(11Z)/16:0);PA(21:0/15:1(9Z));PA(22:0/14:1(9Z));PA(22:1(11Z)/14:0);PA(18:1(9Z)/18:0);PA(16:0/20:1(11Z)) |
| 62 | PA(17:0/22:1(11Z));PA(17:1(9Z)/22:0);PA(18:1(9Z)/21:0);PA(19:0/20:1(11Z));PA(19:1(9Z)/20:0);PA(20:0/19:1(9Z));PA(20:1(11Z)/19:0);PA(21:0/18:1(9Z));PA(22:0/17:1(9Z));PA(22:1(11Z)/17:0);PE-Cer(d15:2(4E,6E)/24:0(2OH)) |
| 63 | PA(14:0/18:1(9Z));PA(12:0/20:1(11Z));PA(13:0/19:1(9Z));PA(14:1(9Z)/18:0);PA(15:0/17:1(9Z));PA(15:1(9Z)/17:0);PA(16:1(9Z)/16:0);PA(17:0/15:1(9Z));PA(17:1(9Z)/15:0);PA(18:0/14:1(9Z));PA(19:1(9Z)/13:0);PA(20:1(11Z)/12:0);PA(18:1(9Z)/14:0);PA(16:0/16:1(9Z)) |
| 64 | OH-Spheroidenone |
| 65 | O-(17-carboxyheptadecanoyl)carnitine |
| 66 | N-palmitoyl tryptophan |
| 67 | N-oleoyl histidine |
| 68 | N-arachidonoyl D-serine;N-arachidonoyl L-serine;N-stearoyl taurine;15-HETE-Ala;12-HETE-Ala |
| 69 | N-(3E-hexadecenoyl)-deoxysphing-4-enine-1-sulfonate |
| 70 | Minabeolide-2 |
| 71 | MG(16:0/0:0/0:0)[rac];MG(16:0/0:0/0:0);MG(0:0/16:0/0:0);1-O-(2R-methoxy-4Z-pentadecenyl)-sn-glycerol;1-O-(2R-hydroxy-4Z-hexadecenyl)-sn-glycerol |
| 72 | L-Isoleucic acid;DL-2-hydroxy caproic acid;DL-3-hydroxy caproic acid;DL-4-hydroxy caproic acid;5-hydroxy caproic acid;6-hydroxy caproic acid;5R-hydroxy-hexanoic acid;3R-hydroxy-hexanoic acid;2-hydroxy-3-methyl-pentanoic acid;Leucinic acid;2-ethyl-2-hydroxy- |

| | |
|---|---|
| | butyric acid;D-Leucic acid;hydroxy-isocaproic acid;(S)-3-hydroxyhexanoic acid;(2R,3S)-2-hydroxy-3-methylpentanoic acid;(2S,3R)-3-hydroxy-2-methylpentanoic acid |
| 73 | GM4(d18:1/20:0) |
| 74 | GlcCer(d18:2(4E,8Z)/16:0(2OH[R]));GlcCer(d18:2(4E,8E)/16:0(2OH[R]));GlcCer(d14:2(4E,6E)/20:0(2OH));GlcCer(d16:2(4E,6E)/18:0(2OH)) |
| 75 | GlcCer(d15:2(4E,6E)/20:0) |
| 76 | GlcCer(d14:1/18:1);GlcCer(d14:2(4E,6E)/18:0) |
| 77 | ent-9-L1-PhytoP;16-B1-PhytoP;9-L1-PhytoP;ent-16-B1-PhytoP;9-B1-PhytoP;ent-9-B1-PhytoP;16-A1-PhytoP;16-epi-16-A1-PhytoP;9-A1-PhytoP;9-epi-9-A1-PhytoP;ent-16-A1-PhytoP;ent-16-epi-16-A1-PhytoP;ent-9-A1-PhytoP;ent-9-epi-9-A1-PhytoP;16-J1-PhytoP;16-epi-16-J1-PhytoP;9-J1-PhytoP;9-epi-9-J1-PhytoP;ent-16-J1-PhytoP;ent-16-epi-16-J1-PhytoP;ent-9-J1-PhytoP;ent-9-epi-9-J1-PhytoP;14,14,14-Trifluoro-11E-tetradecenyl acetate;14,14,14-Trifluoro-11Z-tetradecenyl acetate |
| 78 | dolichyl-4-D-xylosyl phosphate |
| 79 | Diketospirilloxanthin/ 2,2'-Diketospirilloxanthin |
| 80 | DGCC(16:0/20:5);DGCC(20:5/16:0) |
| 81 | DG(22:5(7Z,10Z,13Z,16Z,19Z)/22:5(7Z,10Z,13Z,16Z,19Z)/0:0);DG(22:4(7Z,10Z,13Z,16Z)/22:6(4Z,7Z,10Z,13Z,16Z,19Z)/0:0)[iso2];PA(15:0/22:1(11Z));PA(15:1(9Z)/22:0);PA(16:1(9Z)/21:0);PA(17:0/20:1(11Z));PA(17:1(9Z)/20:0);PA(18:0/19:1(9Z));PA(18:1(9Z)/19:0);PA(19:0/18:1(9Z));PA(19:1(9Z)/18:0);PA(20:0/17:1(9Z));PA(20:1(11Z)/17:0);PA(21:0/16:1(9Z));PA(22:0/15:1(9Z));PA(22:1(11Z)/15:0) |
| 82 | DG(12:0/17:1(9Z)/0:0)[iso2];DG(13:0/16:1(9Z)/0:0)[iso2] |
| 83 | delta2-THA;5beta-Chola-3,8(14),11-trien-24-oic Acid |
| 84 | Cervonyl carnitine |
| 85 | bromosuccinic acid |
| 86 | Bombykol;10-propyl-5,9-tridecadien-1-ol;7,11-hexadecadien-1-ol;6E,11Z-hexadecadien-1-ol;6Z,11Z-hexadecadien-1-ol;10E,12E-Hexadecadien-1-ol;11E,13E-Hexadecadien-1-ol;11E,13Z-Hexadecadien-1-ol;4E,6Z-Hexadecadien-1-ol;11Z,13E-Hexadecadien-1-ol;7Z,11E-Hexadecadien-1-ol;11Z,13Z-Hexadecadien-1-ol;7Z,11Z-Hexadecadien-1-ol;1,3-Hexadecadien-1-ol;2-hexadecenal;7-hexadecenal;9-hexadecenal;11-hexadecenal;2Z-hexadecenal;10E-Hexadecenal;10Z-Hexadecenal;11Z-Hexadecenal;12Z-Hexadecenal;7Z-Hexadecenal;9Z-Hexadecenal;cis-11-Hexadecenal;(Z)-hexadec-13-enal;1,15-Hexadecadien-3-one;1-Hexadecen-3-one |
| 87 | Behenic acid;Isobehenic acid;19-methyl-heneicosanoic acid;3-methyl-heneicosanoic acid;14,19-dimethyl-eicosanoic-acid;Eicosyl acetate;octadecyl butyrate;hexadecyl hexanoate;tetradecyl octanoate;dodecyl decanoate;hexyl hexadecanoate;6,10,13-Trimethyltetradecyl 3-methylbutanoate;16-Methylheptadecyl isobutyrate;Octadecyl isobutyrate;Butyl octadecanoate |
| 88 | bayogenin;Acacic acid;Arjunolic acid;11-acetoxy-3beta,6alpha-dihydroxy-24-methylene-9,11-seco-5alpha-cholesta-7,22E-dien-9-one. ;11-acetoxy-3beta,6alpha-dihydroxy-24-methyl-9,11-seco-5alpha-cholesta-7,22Z-dien-9-one. ;cimigenol |
| 89 | Axillarenic acid;Nebraskanic acid;Tetracosanedioic acid |
| 90 | Angelic acid;Tiglic acid;beta,beta-dimethyl acrylic acid;Isopropenylacetic acid;2-ethyl acrylic acid;beta-ethyl acrylic acid;beta-penteic acid;Allyl acetic acid;cis-pent-2-enoic acid;cis-pent-3-enoic acid;ethyl 2E-propenoate;gamma-valerolactone;Pentane-2,4-dione |
| 91 | 9-Keto heptadecylic acid;16-oxo-heptadecanoic acid;2-oxo-heptadecanoic acid;3-oxo-heptadecanoic acid;2-methoxy-5Z-hexadecenoic acid;2-methoxy-6Z-hexadecenoic acid;Avocadyne;Muricatacin |
| 92 | 6,8-dihydroxy-octanoic acid |
| 93 | 5-(L-alanin-3-yl)-2-hydroxy-cis,cis-muconate 6-semialdehyde |
| 94 | 4R-aminopentanoic acid;4S-aminopentanoic acid;4-amino-pentanoic acid;5-amino-pentanoic acid;2S-amino-pentanoic acid;2-Amino-3-methylbutanoic acid |
| 95 | 4,8,12-Trimethyl-1,3E,7E,11-tridecatetraene;3,6,9-Hexadecatriene |
| 96 | 4,4'-Diapo-zeta-carotene |

| | |
|---|---|
| 97 | 3alpha-Hydroxy-6-oxo-5beta-cholan-24-oic Acid;3beta-Hydroxy-6-oxo-5beta-cholan-24-oic Acid;3alpha-Hydroxy-6-oxo-5alpha-cholan-24-oic Acid;3beta-Hydroxy-6-oxo-5alpha-cholan-24-oic Acid;7-oxolithocholic acid;3beta-Hydroxy-7-oxo-5beta-cholan-24-oic Acid;3beta-Hydroxy-7-oxo-5alpha-cholan-24-oic Acid;3alpha-Hydroxy-11-oxo-5beta-cholan-24-oic Acid;3beta-Hydroxy-11-oxo-5beta-cholan-24-oic Acid;3alpha-Hydroxy-12-oxo-5beta-cholan-24-oic Acid;3beta-Hydroxy-12-oxo-5beta-cholan-24-oic Acid;12beta-Hydroxy-3-oxo-5beta-cholan-24-oic Acid;6alpha-Hydroxy-3-oxo-5beta-cholan-24-oic Acid;6beta-Hydroxy-3-oxo-5beta-cholan-24-oic Acid;6alpha-Hydroxy-3-oxo-5alpha-cholan-24-oic Acid;7alpha-Hydroxy-3-oxo-5beta-cholan-24-oic Acid;7beta-Hydroxy-3-oxo-5beta-cholan-24-oic Acid;7alpha-Hydroxy-3-oxo-5alpha-cholan-24-oic Acid;7alpha-Hydroxy-12-oxo-5beta-cholan-24-oic Acid;7beta-Hydroxy-12-oxo-5beta-cholan-24-oic Acid;7alpha-Hydroxy-12-oxo-5alpha-cholan-24-oic Acid;7beta-Hydroxy-12-oxo-5alpha-cholan-24-oic Acid;12alpha-Hydroxy-3-oxo-5beta-cholan-24-oic Acid;12alpha-Hydroxy-3-oxo-5alpha-cholan-24-oic Acid;12alpha-Hydroxy-7-oxo-5alpha-cholan-24-oic Acid;3beta,6beta-Dihydroxychol-4-en-24-oic Acid;3beta,7alpha-Dihydroxychol-4-en-24-oic Acid;3beta,7alpha-Dihydroxychol-5-en-24-oic Acid;3beta,7beta-Dihydroxychol-5-en-24-oic Acid;3beta,12alpha-Dihydroxychol-5-en-24-oic Acid;3alpha,12alpha-Dihydroxy-5beta-chol-6-en-24-oic Acid;3alpha,12beta-Dihydroxy-5beta-chol-6-en-24-oic Acid;3alpha,12alpha-Dihydroxy-5beta-chol-7-en-24-oic Acid;3alpha,12alpha-Dihydroxy-5beta-chol-8-en-24-oic Acid;3alpha,12alpha-Dihydroxy-5beta-chol-8(14)-en-24-oic Acid;3alpha,12alpha-Dihydroxy-5beta-chol-9(11)-en-24-oic Acid;7alpha,12alpha-Dihydroxy-5beta-chol-3-en-24-oic Acid;(22E)-3alpha,7alpha-Dihydroxy-5beta-chol-22-en-24-oic Acid;(22E)-3alpha,7beta-Dihydroxy-5beta-chol-22-en-24-oic Acid;(22E)-3alpha,12alpha-Dihydroxy-5beta-chol-22-en-24-oic Acid;1alpha-Hydroxy-3-oxo-5beta-cholan-24-oic Acid;3alpha,7alpha-Dihydroxychol-5-en-24-oic Acid;3alpha,7beta-Dihydroxychol-5-en-24-oic Acid;3alpha,7alpha-Dihydroxy-5beta-chol-11-en-24-oic Acid;3alpha,7beta-Dihydroxy-5beta-chol-11-en-24-oic Acid;3alpha,12alpha-Dihydroxy-5beta-chol-14-en-24-oic Acid;3alpha,12beta-Dihydroxy-5beta-chol-9(11)-en-24-oic Acid;3alpha-Hydroxy-12-oxo-5alpha-cholan-24-oic Acid;7alpha,12alpha-Dihydroxy-5beta-chol-2-en-24-oic Acid;12alpha-Hydroxy-7-oxo-5beta-cholan-24-oic Acid;3beta,19-Dihydroxychol-5-en-24-oic Acid;3alpha-Hydroxy-7-oxo-5alpha-cholan-24-oic Acid;3alpha,7alpha-Dihydroxy-5beta-chol-16-en-24-oic Acid |
| 98 | 3,4,3',4'-Tetrahydrospirilloxanthin |
| 99 | 3,4-dihydroxy-4-methylhexadecanoic acid;1-O-(2R-hydroxy-4Z-tetradecenyl)-sn-glycerol |
| 100 | 3-Methylsubericacid;Azelaic acid;cis- and trans-Ethyl 2,4-dimethyl-1,3-dioxolane-2-acetate |
| 101 | 3-hydroxypalmitoleoylcarnitine;N-stearoyl glutamic acid |
| 102 | 2,5-Diaminopentanoic acid |
| 103 | 2,4-diamino-butyric acid |
| 104 | 2-deoxyecdysone;25-deoxyecdysone;Porrigenin A;Digitogenin;Agigenin;Paniculogenin;Neoagigenin;Tokorogenin;Epimetagenin;Metagenin;Convallagenin A;Neotokorogenin;Hispigenin;Solaspigenin;Neosolaspigenin;(24R)-6,19-epidioxy-1alpha,24-dihydroxy-6,19-dihydrovitamin D3 / (24R)-6,19-epidioxy-1alpha,24-dihydroxy-6,19-dihydrocholecalciferol;(6R)-6,19-epidioxy-1alpha,25-dihydroxy-6,19-dihydrovitamin D3 / (6R)-6,19-epidioxy-1alpha,25-dihydroxy-6,19-dihydrocholecalciferol;(23S,25R)-1alpha,23,25,26-tetrahydroxyvitamin D3 / (23S,25R)-1alpha,23,25,26-tetrahydroxycholecalciferol;1alpha,23R,25S,26-Tetrahydroxyvitamin D3;7beta,12alpha-Dihydroxy-3-oxo-5beta-cholestan-26-oic acid;7alpha,12alpha-Dihydroxy-3-oxo-5beta-cholestan-26-oic acid;7alpha,12alpha-Dihydroxy-3-oxo-5alpha-cholestan-26-oic acid;3alpha,12alpha-Dihydroxy-7-oxo-5beta-cholestan-26-oic acid;3alpha,7alpha,12alpha-Trihydroxy-5beta-24E-cholesten-26-oic acid;3alpha,7alpha,12alpha-Trihydroxy-5beta-cholest-23-en-26-oic acid;3alpha,7alpha-Dihydroxy-12-oxo-5alpha-cholestan-26-oic acid;3alpha,7alpha,12alpha-trihydroxy-5alpha-23E-cholesten-26-oic acid;3alpha,7alpha,12alpha-Trihydroxy-5beta-24Z-cholesten-26-oic acid |
| 105 | 17-phenyl-trinor-PGF2alpha amide;N-linoleoyl taurine |
| 106 | 17-oxo-20Z-hexacosenoic acid;Ficulinic acid A;22-keto-26-Hexacosanolide |
| 107 | 12beta-hydroxy-24-norcholesta-1,4,22E-trien-3-one |
| 108 | 10-oxo-nonadecanoic acid;18-oxo-nonadecanoic acid;2-oxo-nonadecanoic acid;3-oxo-nonadecanoic acid |

| | |
|---|---|
| 109 | 1-tetradecanyl-2-(8-[3]-ladderane-octanyl)-sn-glycerophosphoethanolamine;GlcCer(d15:2(4E,6E)/18:0) |
| 110 | 1-tetradecanyl-2-(8-[3]-ladderane-octanyl)-sn-glycerophosphoethanolamine |
| 111 | 1-O-(2R-hydroxy-hexadecyl)-sn-glycerol |
| 112 | 1-chloro-3-(5'-(penta-1,3-diyn-1-yl)-[2,2'-bithiophen]-5-yl)prop-2-yn-1-ol |
| 113 | 1-(6-[3]-ladderane-hexanyl)-2-(8-[3]-ladderane-octanyl)-sn-glycerophosphocholine |
| 114 | 1-(2-methoxy-eicosanyl)-sn-glycero-3-phosphoethanolamine |
| 115 | (3'-sulfo)Galbeta-Cer(d18:1/22:0) |
| 116 | (2S,3R,4E,8E)-3-Hydroxy-2-[methyl(stearoyl)amino]-4,8-octadecadien-1-yl hydrogen sulfate |
| 117 | (2E,5Z,7E)-decatrienoylcarnitine |
| 118 | (25S)-5alpha-cholestan-3beta,6alpha,7beta,8beta,15alpha,16beta,26-heptol;(25S)-5alpha-cholestan-3beta,4beta,6alpha,8beta,15alpha,16beta,26-heptol |
| 119 | (22E)-26,26,26,27,27,27-hexafluoro-25-hydroxy-22,23-didehydrovitamin D3 / (22E)-26,26,26,27,27,27-hexafluoro-25-hydroxy-22,23-didehydrocholecalciferol |
| 120 | (11Z)-eicoseneoylcarnitine |
| 121 | (11Z,14Z)-eicosadienoylcarnitine |

## REFERENCES


[1] Kim, M., Rai, N., Zorraquino, V., Tagkopoulos I., Multi-omics integration accurately predicts cellular state in unexplored conditions for Escherichia coli, *Nat Commun.* 7 (2016), 13090-96.

[2] Wilson, B.J., Nicholls, S.G., The Human Genome Project, and recent advances in personalized genomics, *Risk Manag Healthc Policy*, 8 (2015), 9-20.

[3] Du, F., Zou, Y., Hu, Q., Zhang, H., Ye, D., Comparative transcriptomic analysis reveals molecular processes involved in pileus morphogenesis in Pleurotus eryngii under different light conditions, *Genomics*, 2019.

[4] Ahmed, F., Kumar, G., Soliman, F.M., Adly, M.A., Soliman, H.A.M., El-Matbouli, M., et al., Proteomics for understanding pathogenesis, immune modulation and host pathogen interactions in aquaculture, *Comp Biochem Physiol Part D Genomics Proteomics*, 32 (2019), 100625.

[5] Jia, H., Wang L, Li, J., Sun, P., Lu, M., Hu J., Comparative metabolomics analysis reveals different metabolic responses to drought in tolerant and susceptible poplar species, *Physiol Plant*, 2019.

[6] Lydic, TA, Goo, Y.H., Lipidomics unveils the complexity of the lipidome in metabolic diseases, *Clin Transl Med*., 7 (2018), 4-17.

[7] Rupasinghe, T.W., Lipidomics: extraction protocols for biological matrices. *Methods Mol Biol.* 1055 (2013) 71-80.

[8] Hu T, Zhang, JL., Mass-spectrometry-based lipidomics. *J Sep Sci.* 41 (2018) 351-72.

[9] Hsu FF. Mass spectrometry-based shotgun lipidomics-a critical review from the technical point of view, *Anal Bioanal Chem*., 410 (2018), 6387-409.

[10] Loizides-Mangold, U., On the future of mass-spectrometry-based lipidomics, *FEBS J.*, 280 (2013), 2817-29.

[11] Kyle JE, Crowell KL, Casey CP, Fujimoto GM, Kim S, Dautel SE, et al. LIQUID: an-open source software for identifying lipids in LC-MS/MS-based lipidomics data. *Bioinformatics*. 33 (2017) 1744-6.
[12] Zhou Z, Shen X, Chen X, Tu J, Xiong X, Zhu ZJ. LipidIMMS Analyzer: integrating multi-dimensional information to support lipid identification in ion mobility-mass spectrometry based lipidomics. *Bioinformatics*. 35 (2019) 698-700.
[13] Zhou Z, Tu J, Xiong X, Shen X, Zhu ZJ. LipidCCS: Prediction of Collision Cross-Section Values for Lipids with High Precision To Support Ion Mobility-Mass Spectrometry-Based Lipidomics. *Anal Chem*. 89 (2017) 9559-66.
[14] Yeo HC, Chen S, Ho YS, Lee DY. An LC-MS-based lipidomics pre-processing framework underpins rapid hypothesis generation towards CHO systems biotechnology. *Metabolomics*. 14 (2018) 98.
[15] Tsugawa H, Cajka T, Kind T, Ma Y, Higgins B, Ikeda K, et al. MS-DIAL: data-independent MS/MS deconvolution for comprehensive metabolome analysis. *Nat Methods*. 12 (2015) 523-6.
[16] Tsugawa H, Ikeda K, Tanaka W, Senoo Y, Arita M, Arita M. Comprehensive identification of sphingolipid species by in silico retention time and tandem mass spectral library. *J Cheminform*. (2017) 19.
[17] Klatt S, Brammananth R, O'Callaghan S, Kouremenos KA, Tull D, Crellin PK, et al. Identification of novel lipid modifications and intermembrane dynamics in Corynebacterium glutamicum using high-resolution mass spectrometry, *J Lipid Res*. 59 (2018) 59 1190-204.
[18] Pluskal T, Castillo S, Villar-Briones A, Oresic M. MZmine 2: modular framework for processing, visualizing, and analyzing mass spectrometry-based molecular profile data, *BMC Bioinformatics*, 11 (2010) 395.

*Current Address:* Engin KOÇAK, Department of Analytical Chemistry, Faculty of Pharmacy, Hacettepe University, Ankara, TURKEY
*E-mail address:* kengin@hacettepe.edu.tr
*URL:* https://orcid.org/0000-0002-1076-1300

# INSTRUCTIONS TO CONTRIBUTORS

**Communications Faculty of Sciences University of Ankara Series A2-A3: Physical Sciences and Engineering** is a peer reviewed journal which has been published since 1948 by Ankara University, accepts original research articles written in English in the fields of Physics, Engineering Physics, Electronics/Computer Engineering, Astronomy and Geophysics. Review articles written by eminent scientists can also be invited by the Editor.

The publication costs for *Communications Faculty of Sciences University of Ankara Series A2-A3* are covered by the journal, so authors do not need to pay an article-processing and submission charges. The PDF copies of accepted papers are **free of charges** and can be downloaded from the webside. Hard copies of the paper, if required, are due to be charged for the amount of which is determined by the administration each year.

Manuscripts should be typeset using a **word processor** editor. Authors should prepare the article using the COMMUNICATIONS style before **submission to the editor via our submission system.** Manuscripts written in any plain TeX format are also acceptable. A **template of manuscript** can be downloaded in **doc** form from the link http://dergipark.org.tr/download/journal-file/13094 (or can be reviewed in pdf form). Authors are required to submit their Open Researcher and Contributor ID (**ORCID**) 's which can be obtained from http://orcid.org as their URL address in the format http://orcid.org/xxxx-xxxx-xxxx-xxxx. Acknowledgements should be given as short as possible at the end of the text. Formulas should be numbered consecutively in parentheses. The following format for the references should be used. Authors are urged to use the Communication.csl style (https://dergipark.org.tr/en/download/journal-file/18514) in **Mendeley Desktop** or **Zotero** automated bibliography. If manual entry is prefered for bibliography, then all citations must be listed in the references part and vice versa. Below, It has no relationship with the text, but can be used to show sample citations such as; for articles [1, 4], for books/booklets/theses [3], and for proceedings/conferences etc. [2].


[1] Demirci, E., Unal, A., Özalp, N., A fractional order SEIR model with density dependent death rate, *Hacettepe J. Math. Stat.*, 40 (2) (2011), 287–295.

[2] Gairola, A. R., Deepmala, Mishra, L. N., Rate of approximation by finite iterates of q-Durrmeyer operators, *Proc. Natl. Acad. Sci. India Sect. A Phys. Sci.*, 86 (2) (2016), 229–234.

[3] Lehmann, E. L., Casella, G., Theory of Point Estimation, Springer, New York, 2003.

[4] Özalp, N., Demirci, E., A fractional order SEIR model with vertical transmission, *Math.Comput. Model.*, 54 (1-2) (2011), 1–6, https://dx.doi.org/10.1016/j.mcm.2010.12.051.


After the acceptance of manuscripts for publication, we will ask you to submit the TeX form of the manuscript prepared in accordance with the style of the Journal. Authors are required to submit their Open Researcher and Contributor ID (ORCID) 's which can be obtained from http://orcid.org as their URL address in the format http://orcid.org/xxxx-xxxx-xxxx-xxxx. Manuscripts should be submitted in the **PDF** form together with **THE COVER LETTER** (http://dergipark.org.tr/download/journal-file/14088) In the cover letter please suggest potential peer reviewers for your manuscript and please provide institutional email addresses where possible, or information which will help the Editor to verify the identity of the reviewer (for example an ORCID or Scopus ID). In the cover letter, you may enter details of anyone who you would prefer not to review your manuscript. Note that in **the cover letter**, authors should nominate **three potential reviewers** and the most appropriate **Field Editor** of the research. The editorial office may not use these nominations, but this may help to speed up the selection of appropriate reviewers.

The Editor may seek the advice of two, or three referees, depending on the response of the referees, chosen in consultation with appropriate members of the Editorial Board, from among experts in the field of specialization of the paper. The reviewing process is conducted in strict confidence and the identity of a referee is not disclosed to the authors at any point since we use a **single-blind peer review process**.



It is a fundamental condition that articles submitted to **COMMUNICATIONS** have not been previously published and will not be simultaneously submitted or published elsewhere. After the manuscript has been accepted for publication, the author will not be permitted to make any new additions to the manuscript.

Before publication the galley proof is always sent to the author for correction. Thus it is solely the author's responsibility for any typographical mistakes which occur in their article as it appears in the Journal. The contents of the manuscript published in the COMMUNICATIONS are the sole responsibility of the authors.

With the submission of the manuscript authors declare that:

- ➢ All authors of the submitted research paper have directly participated in the planning, execution, or analysis of study;
- ➢ All authors of the paper have read and approved the final version submitted;
- ➢ The contents of the manuscript have not been submitted, copyrighted or published elsewhere and the visual-graphical materials such as photograph, drawing, picture, and document within the article do not have any copyright issue;
- ➢ The contents of the manuscript will not be copyrighted, submitted, or published elsewhere, while acceptance by the Journal is under consideration.
- ➢ The article is clean in terms of plagiarism, and the legal and ethical responsibility of the article belong to the author(s). Author(s) also accept that the manuscript may go through plagiarism check using iThenticate software;
- ➢ The objectivity and transparency in research, and the principles of ethical and professional conduct have been followed. Authors have also declared that they have no potential conflict of interest (financial or non-financial), and their research does not involve any human participants and/or animals.

Research papers published in **Communications Faculty of Sciences University of Ankara** are archived in the Library of Ankara University (Volume 1-60) and Dergipark immediately following publication with no embargo.


Editor in Chief
Commun. Fac. Sci. Univ. Ank. Ser. A2-A3.
Ankara University, Faculty of Sciences
06100, Besevler - ANKARA TURKEY

# C O M M U N I C A T I O N S

FACULTY OF SCIENCES
UNIVERSITY OF ANKARA

DE LA FACULTE DES SCIENCES
DE L'UNIVERSITE D'ANKARA

Series A2-A3: Physical Sciences and Engineering

**Volume 62** **Number : 1** **Year :2020**